Qualification of the Instrumented Indentation Technique for the Parameter Identification of Welded Advanced High Strength Steels

vorgelegt von
M. Sc.
Ehsan Javaheri

an der Fakultät V – Verkehrs- und Maschinensysteme
der Technischen Universität Berlin
zur Erlangung des akademischen Grades

Doktor der Ingenieurwissenschaften
– Dr.-Ing. –

Promotionsausschuss:

Vorsitzender: Prof. Dr. -Ing. Matthias Rötting
Gutachter: Prof. Dr. rar. Nat. Wolfgang H. Müller
Gutachter: Prof. Dr. -Ing. Reza Rawassizadeh
Gutachter: Prof. Dr. -Ing. Zuheir Barsoum

Tag der wissenschaftlichen Aussprache: 04. März 2022

Berlin 2022

Abstract

An essential step in the manufacturing or development of a product, or in inspecting the durability of an existing structure or machinery, is to have information about the strength of its consisting materials. Such an information, which can be summarized in the form of a stress-strain diagram, can be obtained by performing a conventional tensile test on the specimens made of the target material. However, when the fabrication of a product requires different manufacturing processes such as welding, the final structure is made of different materials that each has its own unique behavior, e.g., the unique stress-strain curve. In many cases, it is not possible to prepare a homogeneous tensile specimen from such a product, e.g. a welded joint contains three different zones such as base metal, weld seam and heat affected zone. Therefore, it is proposed to reproduce the microstructure of the interest zone in a large area by using a thermomechanical simulator to finally provide a standard tensile specimen or prepare the micro tensile specimens from the target area that require significant effort or the infrastructures which are not available in many small companies or research institutes. Consequently, an alternative approach is needed to determine the mechanical properties of a structure locally with straightforward implementation for the end user. The current research work aims to further develop the instrumented indentation technique (test) to establish a correlation between the indentation test information and the material parameters of an investigated sample. In the first step, the force-indentation depth curves obtained as the output of the instrumented indentation machine are connected with the mechanical properties of the indented samples using a trained artificial neural network. Subsequently, the methodology has been developed by training the artificial neural network based on the data from the surface of an indented sample, which is summarized in the form of the indented surface profile. The latter approach is not only more precise than the first one, it is additionally independent of the instrumented indentation machine which makes it applicable in many small companies. Moreover, there is a strong agreement between the output of

the two trained artificial neural networks and the experimental results, indicating the robustness of the employed methodology. Additionally, at the end of the current report and in further work, the introduced methodology was advanced and a concept was presented to perform material characterization with artificial neural networks which are trained with the images taken from the indented surface of a specimen using a high-resolution 3D measurement system and a light microscope. Although, these trained artificial neural networks show acceptable performance and further ease material characterization for the end user, the accuracy of the predicted material parameters can be increased enormously by enlargement of the training datasets.

Zusammenfassung

Ein entscheidender Schritt bei der Herstellung oder Entwicklung eines Produkts oder bei der Inspektion der Haltbarkeit einer bestehenden Struktur oder Maschine ist es, detaillierte Kenntnisse über die Festigkeit der verwendeten Materialien zu haben. Eine solche Information, die in Form eines Spannungs-Dehnungs-Diagramms zusammengefasst werden kann, kann durch eine klassische Zugprüfung an den Proben aus dem Zielmaterial bestimmt werden. Erfordert die Herstellung eines Produkts jedoch verschiedene Fertigungsprozesse wie z. B. Schweißen, besteht die fertige Struktur aus verschiedenen Materialien, die jeweils ein einzigartiges Verhalten aufweisen, z. B. die einzigartige Spannungs-Dehnungskurve. In vielen Fällen ist es nicht möglich, eine homogene Zugprobe aus einem solchen Produkt herzustellen, z.B. enthält eine Schweißverbindung drei verschiedene Zonen wie Grundwerkstoff, Schweißnaht und Wärmeeinflusszone. Eine Möglichkeit besteht darin, die zu untersuchende Zone in einem großen Bereich mit Hilfe eines thermomechanischen Simulators zu reproduzieren, um somit eine normierte Zugprobe aus dem Zielbereich zu fertigen. Diese Methode bedeutet einen erheblichen Aufwand und erfordert Infrastrukturen, die in vielen kleinen Unternehmen oder Forschungsinstituten nicht verfügbar sind. Folglich wird ein alternativer Ansatz mit einfacher Implementierung für den Endanwender benötigt, um die mechanischen Eigenschaften einer Struktur lokal zu bestimmen. Die aktuelle Forschungsarbeit zielt darauf ab, die instrumentierte Eindringprüfung weiterzuentwickeln, um eine Korrelation zwischen den Informationen der Eindringprüfung und den Materialparametern einer untersuchten Probe herzustellen. Im ersten Schritt werden die als Output der instrumentierten Eindringmaschine erhaltenen Kraft-Eindringtiefen-Kurven mit Hilfe eines trainierten künstlichen neuronalen Netzes mit den mechanischen Eigenschaften der eingedrückten Proben verbunden. Anschließend wurde eine Methodik entwickelt, mit der das künstliche neuronale Netz auf Basis der Daten der Oberfläche einer eingedrückten Probe, die in Form des eingedrückten Oberflächenprofils

zusammengefasst werden, trainiert werden kann. Der letztere Ansatz ist nicht nur präziser als der Erste, er ist zusätzlich unabhängig von der instrumentierten Eindringmaschine, was ihn in vielen kleinen Unternehmen anwendbar macht. Außerdem gibt es eine starke Übereinstimmung zwischen der Ausgabe der beiden trainierten künstlichen neuronalen Netze und den experimentellen Ergebnissen, was auf die Stabilität der verwendeten Methodik hinweist. Zusätzlich wurde am Ende des aktuellen Berichts und in „Further Work“ die vorgestellte Methodik weiterentwickelt und ein Konzept vorgestellt, bei dem die Materialcharakterisierung mit künstlichen neuronalen Netzen durchgeführt wird, welche mit den Bildern, aufgenommen mit einem hochauflösenden 3D-Messsystem und einem Lichtmikroskop, der eingedrückten Oberfläche einer Probe trainiert werden. Obwohl diese trainierten künstlichen neuronalen Netze eine akzeptable Performance zeigen und die Materialcharakterisierung für den Endanwender weiter erleichtern, kann die Genauigkeit der vorhergesagten Materialparameter durch Vergrößerung der Trainingsdatensätze enorm gesteigert werden.

List of Publications

The contents of this dissertation have already been published in the following research works:

1. E. Javaheri, V. Kumala, A. Javaheri, R. Rawassizadeh, J. Lubritz, B. Graf and M. Rethmeier, "Quantifying Mechanical Properties of Automotive Steels with Deep Learning Based Computer Vision Algorithms," *Metals (10),* p. 163, 2020, https://doi.org/10.3390/met10020163 [1]

2. E. Javaheri, A. Pittner, B. Graf and M. Rethmeier, "Mechanical properties characterization of resistance spot welded DP1000 steel under uniaxial tensile tests," *Materials Testing 61(6),* pp. 527-532, 2019, https://doi.org/10.3139/120.111349 [2]

3. E. Javaheri, J. Lubritz, B. Graf and M. Rethmeier, "Mechanical Properties Characterization of Welded Automotive Steels," *Metals (10) 1,* 2020, https://doi.org/10.3390/met10010001 [3]

4. E. Javaheri, A. Pittner, B. Graf and M. Rethmeier, "Application of artificial neural network for the determination of local material properties of welded steel structures," in *Estad*, Düsseldorf, Germany, 2019. [4]

5. E. Javahei, A. Pittner, B. Graf and M. Rethmeier, "Instrumented indentation technique and its application for the determination of local material properties of welded steel structures," in *39. Assistentenseminar, DVS report 2019*, Aachen, Germany, 2019. [5]

6. E. Javaheri, B. Graf, M. Rethmeier; AIF-Bericht; Forschungsprojekt P 1248 / IGF-Nr. 19550 N der FOSTA, „Qualifizierung der instrumentierten Eindringprüfung zur Kennwertermittlung für hochfeste Stähle mit Schweißungen“, Bestell-Nr. P 1248, ISBN-Nummer 978-3-946885-98-6, Forschungsvereinigung Stahlanwendung e. V., Düsseldorf, 2021 [6]

Contents

List of Tables

List of Figures

Abbreviation

FEM	Finite Element Method
HAZ	Heat Affected Zone
BM	Base Metal
WM	Weld Metal
IIT	Instrumented Indentation Technique
AHSS	Advanced High Strength Steel
ANN	Artificial Neural Network
RSW	Resistance Spot Welding
LBW	Laser Beam Welding
AI	Artificial Intelligence
GPU	Graphical Processing Units
DIC	3D-Digital Image Correlation (DIC)
DP-steel	Dual Phase steel
TRIP-steel	Transformation Induced Plasticity steel
TT	Tensile Test
$t_{8/5}$	Time of the dropping temperature from 800 °C to 500 °C
TTT diagram	Time Temperature Transformation diagram
LMA	Levenberg-Marquardt Algorithm
MSE	Mean Square Error
R	Pearson Correlation Coefficient

1. Introduction

One of the most critical aspects in the initial design, development, and construction of any new structure or product is to have enough information about its materials' reliability and strength. This information should be considered at various steps of manufacturing of the new product, such as the designing, the idea implementation, and the prototype testing [8]. Knowing the material data leads to identifying and improving the structural weaknesses in the early phases of product manufacturing. This fact becomes even more critical when fast changes in modern society force the industries and manufacturers to optimize and reduce their final products' weights to lower fuel consumption and lower air pollution [9]. However, the main challenge is that how we can increase safety, strength, and crashworthiness at the same time [10]. As a result, identifying the material data and parameters have gained increasing importance.

1.1. Scope and Objectives of the Research

The material information, known as the mechanical properties that rely on the physical properties of materials are of utmost importance in the different branches of industries [11]. The traditional method in assessing alloys' mechanical materials is the uniaxial standard tensile testing [12]. However, processes such as welding or grinding affect the mechanical properties locally so that the properties of the bulk of material are different from those affected areas. For example, welding results in a different type of microstructure in a tiny area known as the heat-affected zone (HAZ) or weld metal (WM). One method to study the mechanical properties of these affected zones is to make micro tensile specimens from the material of the target zone [13, p. 01]. However, the fabrication of such micro-scale specimens is extremely expensive, and each step from specimen fabrication to performing the tensile test requires a specialized

infrastructure that is not available in many companies or research institutes. Another approach is to reproduce the microstructure of the target zone, for instance the WM, over a large area and then to produce a homogeneous tensile specimen from the reproduced and simulated microstructure. This method also requires a thermomechanical simulator [14] which is not available in many universities or companies, not even in the research center where the present research was carried out. Therefore, it is necessary to develop a method which is able to evaluate the mechanical properties of the inhomogeneous structure such as welded zones locally.

An alternative method to the tensile test to determine the mechanical properties of the material is to correlate the hardness measurement with material data such as the yield strength or other parameters that describe the plastic behavior of the material [15]. Efforts to relate the hardness measurement analytically to the stress-strain diagram have been started many decades ago and this analytical approach is known as the representative stress-strain method [16]. This methodology is limited to determine only a few parameters of the mechanical properties and cannot predict the entire stress-strain diagram [17]. Furthermore, the current approach does not have sufficient accuracy when it is used to determine the material data of modern steel grades, such as advanced high strength steels (AHSS) or WM due to their high value of yield strength [18].

The indentation test procedure has been developed and attempts have been made to collect more data, such as force and indentation depth, simultaneously and over a period of time, and then to sum this information in a force-indentation depth diagram [19]. Having more data allows to establish a more reliable correlation between the indentation test and the mechanical properties of the material. The artificial neural network (ANN) can be used to solve such an inverse problem and provide a correlation between the information from the indentation test and the material data [20]. This method has been developed over the last decades and shows that the results are quite acceptable for steel structures with low yield strength, but fail drastically in predicting the material data when their yield strength exceeds 400 MPa [18].

However, innovation and development in steel production makes it possible to produce AHSSs with a yield strength of more than 400 MPa [21]. Such steel grades as DP-steels (e.g. DP1000) or high strength fine grained structural steel (e.g. S690QL) are widely used nowadays in various industries such as automotive sector or construction.

Some welding processes, such as resistance spot welding (RSW) technique or laser beam welding (LBW) approach, result in the production of a WM with higher yield strength compared to the plain steel base material (BM). Therefore, the currently available ANNs and analytical approaches (representative stress-strain method) fail to establish a correlation between the result of the indentation test and the mechanical properties of AHSSs (e.g. DP or TRIP Steels) in both the BM and WM. The current research aims to develop an ANN capable of predicting the material behavior of welded AHSS structures with a yield strength of more than 400 MPa by using data from instrumented indentation technique (IIT).

1.2. Methodology of the Research Work

The first step in using an ANN together with the data of IIT to calculate the material properties of AHSSs with a yield strength greater than 400 MPa is to train the ANN for this target range. The ANN as a supervised machine learning algorithm needs input and output datasets to find a pattern or do correlation between datasets. In this case, the data collected from the instrumented indentation technique, which is summarized in a force-indentation depth diagram, can be used as the input data of ANN, and its output is the parameters describing the mechanical properties of the material. It is possible to have small datasets from the indentation test performed experimentally on a limited number of samples. However, it is possible to generate a large volume of training datasets with a validated numerical model of the IIT. The simulation model must be fed with the imaginary material data, which is varied at the desired intervals, as the input data and output data of the numerical model becomes the points which describe the force-indentation depth diagram. The numerical simulation have to be performed repeatedly to generate sufficient datasets. In the training step related to ANN, the simulation model's input becomes the desired output of the ANN, and the simulation output becomes the input of the ANN. When the ANN is trained, its accuracy has been checked and validated by the reference data, e.g., the mechanical properties obtained from the tensile test. This means that the force-indentation depth diagram resulting from the IIT must be given as input to the ANN to calculate the indented specimens' material data.

In the further development of this methodology, it became possible to use other datasets for training the ANN in addition to the force-indentation depth diagram obtained from IIT. The induced deformations on the sample surface are furthermore used to train another ANN to determine the material data. The simulation model generates sufficient datasets to train the ANN with dataset of penetration profile curves. In this approach, the input data is the penetration profile on the surface of the specimen generated from the numerical simulation and the output of the ANN remains the mechanical properties. By using the information from the surface deformation profile of the steel, the accuracy of the ANN to predict the material data becomes higher, and the material characterization method makes independent of the instrumented indentation machine, since it is no longer necessary to measure the force and indentation depth simultaneously over a period of time.

Another dataset used to train the ANN is the images captured by a three-dimensional (3D) measurement sensor from the surface of the indented sample. The output of the sensor shows the deformation depth in colored scale. The images showing the deformation on the surface of the indented samples in a colorful scale are processed and the important features are obtained by using unsupervised machine learning algorithms. Then, these representative features showing the deformation depth on the surface of the samples are used to train the ANN. The accuracy of the material data obtained with the trained ANN with the dataset of 3D measurement images are lower than the result of the ANN trained with the dataset of the force-indentation depth diagram and the profile of the deformed surface. In addition, the output of this ANN has been examined with test materials which are unknown to the ANN and the results show that the predicted material data are in the acceptable range.

The fourth and final datasets used to train the ANN are the images from the surface of indented specimen taken with the light microscope. In this phase, the same procedure such as image processing and feature extraction, as described for training the ANN with the third dataset, is repeated. Several statistical tests are performed to verify the accuracy and correctness of the used methodology in each step. In the final examination, the results of the trained ANN were compared with the test materials which are unknown to the trained ANN. The steps of data generating and training of the ANNs with different datasets are shown in Figure 1.1.

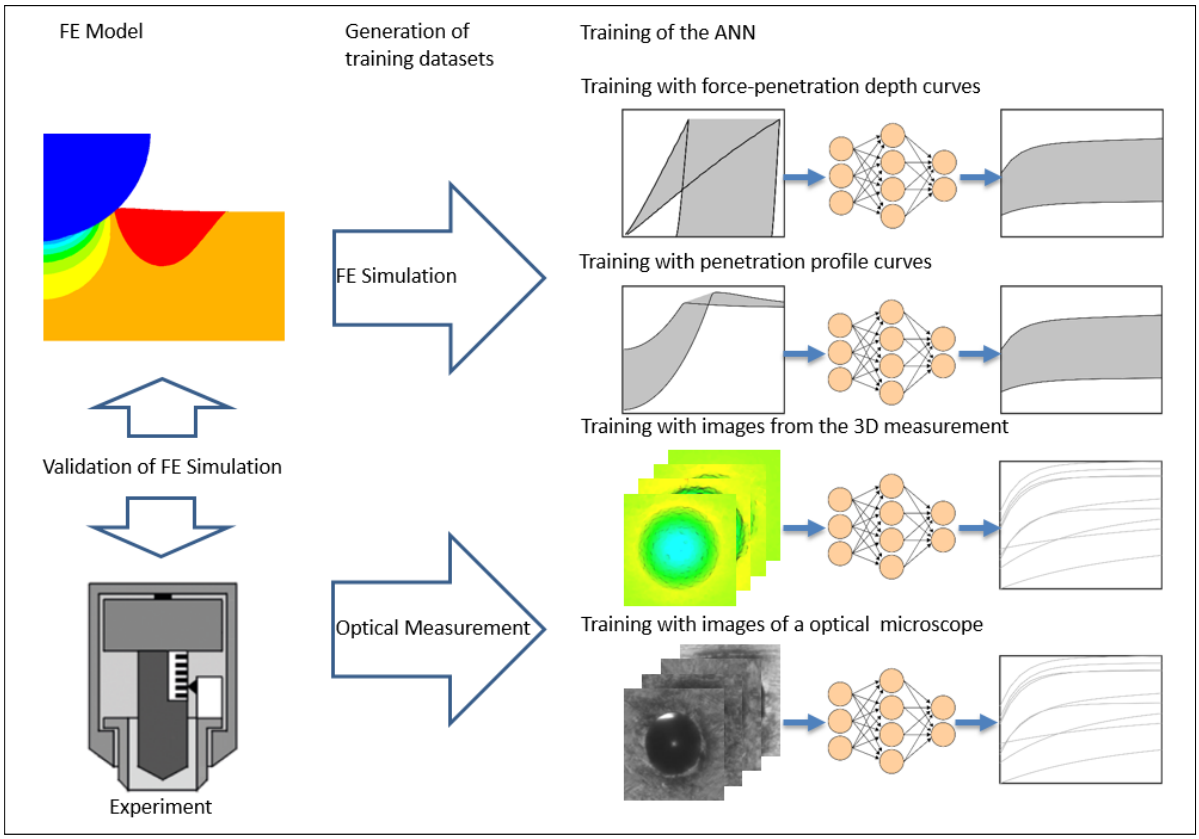

Figure 1.1: An overview of the applied methodology in the present work. The first step is to prepare a numerical simulation model of the instrumented indentation technique (IIT) with the finite element method (FEM) and then validate it with the experimental data. The simulation model then generates sufficient datasets to train the artificial neural network (ANN) in the first two methods: force-penetration (indentation) depth curves and penetration (indentation) profile curves. In the next step, the training is performed by using the images captured by a 3D measurement sensor and a light microscope. In all ANNs, the outputs are the material model parameters that describe the welded steel structure's mechanical properties in different zones, such as weld seam and base metal [1]

1.3. Dissertation Structure

The current dissertation consists of seven chapters including introduction, literature review, material characterization with tensile test, instrumented indentation technique, material characterization with artificial intelligence, summary and finally appendix.

The importance of material testing in industry and also the different approaches to determine the mechanical properties of an inhomogeneous steel structure have already been discussed in the current chapter, the so-called introduction. It was then explained that the analytical formulas and available ANNs fail to predict the mechanical

properties of AHSSs such as DP-steels by using the IIT data. Then, the methodology, used in the current research work, to train the ANNs with different datasets was presented shortly.

The second chapter, the literature review, provide the necessary theoretical background to understand the research objective and the methodology used to answer the research question. At the beginning, the necessity of innovations for the construction of new products is discussed. It then focuses on the role of AHSS in modern products, particularly in the automotive industry. Subsequently, the manufacturing processes, such as welding techniques, and their effects in the production and finishing of inhomogeneous steel structures are explained. In the next step, the traditional and conventional methods to analyze material data and the necessary requirements for their applications are introduced. Next, the available methods for estimating the mechanical properties from the indentation test are reviewed. These methods are compared with each other and their respective advantages, drawbacks, accuracy and areas of usage are highlighted. At the end of this chapter, the results and methodologies used by other researchers to determine material parameters using artificial intelligence (AI) are presented, and the reason and necessity for conducting the current research in accordance with the work of other researchers is pointed out.

The third chapter, known as material characterization with tensile test, aims to determine the material data of the welded AHSSs in both BM and WM. This information is later required as test data to check and verify the accuracy of the trained ANN. It is also necessary to obtain them in order to start with the numerical simulation model of the IIT. First, the AHSSs used in this work are presented and described in details. Then, the methodology for determining the mechanical properties of the BM of the steels is demonstrated and the accuracy of the material model is evaluated. In the next step, a novel method is described to determine the mechanical properties of the WM without reproducing its microstructure in a larger volume by using a thermomechanical simulator, due to its unavailability at the research center where the present study is conducted. In this method, the microstructure of the WM in the resistance spot welding technique (RSW) is reproduced in one steel sheet by varying the welding parameters. To ensure that both WMs have the same microstructure, a range of analyses such as metallographic investigation, temperature and hardness

measurement are carried out. Then, the notched tensile specimens are prepared to guarantee that the fracture during the tensile test occurs in the WM, as the goal is to determine the material data of this zone. Lastly, an investigation is conducted on the concept of geometry factor and the differences between the stress-strain diagram of the notched and smooth tensile specimen. In the end, it becomes possible to determine the stress-strain diagram of the smooth and welded tensile specimens considering the geometry factor. Finally, the material model parameters of the weld seam from the RSW approach are calculated and their accuracy are evaluated.

The objective of the fourth chapter, instrumented indentation technique, is to show the procedure of performing the instrumented indentation test on different samples. Another goal is to introduce a validated numerical simulation model of the indentation test which is capable to generate a large volume of data for training an ANN with an extremely high accuracy. In addition, the material data of the WM produced by laser beam welding (LBM) and also the HAZ in RSW are obtained by inverse analysis with the numerical model of IIT. Furthermore, this section describes the methodology and results of measuring the deformation on the surface of the indented samples by optical sensors, which will later be used to train the ANN.

The fifth chapter, material characterization with ANN, describes the procedure for training and testing the ANN with two types of datasets by using the results of the previous sections, such as the experimentally measured or numerically calculated datasets from Chapter 4 for training and the mechanical properties of the material from Chapter 3 for testing of the accuracy and validation of the ANN. The input for training of the two ANNs are the numerically calculated force-indentation depth diagrams and the deformation profile curves, respectively, and the output are the imaginary parameters of a material model that describes the plastic behavior of welded steels. The data selection, quality and quantity of datasets, ANNs architecture, procedure and parameters of training, accuracy of ANNs output and various statistical tests to check the correctness and confidence of the used supervised machine learning algorithms are explained and discussed in details. In the last step, the results of the individual trained ANNs are compared with the test materials and the repeatability of the results and the error interval are discussed.

Another chapter, labeled as summary, once again provides an overview on the methodology and findings of the present research work. In the appendix, known as the further work, the two other ANNs are trained with the input data obtained from the images captured by a 3D measurement sensor and a light microscope and the output remains the material parameters. The current datasets are cleaned with image processing and the representative features are extracted with unsupervised machine learning algorithms. In a similar way to Chapter 5, the results of the trained ANNs are compared with the test materials to evaluate and analysis the accuracy of trained ANNs with last two datasets.

2. Literature Review

Companies in the automobile industry innovate to keep their share of the market and gain more in the future. The fundamental to innovation is knowing the features of materials used in the industry. It was Schumpeter who showed the importance of innovation for firms by focusing on the roles of economic factors in promoting new technologies [22]. In fact, companies innovate in order to reach new markets and gain a competitive advantage for themselves. Innovation is not limited to manufacturing, and it encompasses new suggestions in implementation, marketing, or improving processes [23]. Loof et al. has demonstrated that innovation is a vital factor for companies to survive. In the recent decade, the competitive environment has been intensified. It leads to pushing firms more into continuous innovation in products and processes to ensure their better performance [24]. A valuable product can only be produced if a suitable manufacturing process is chosen together with proper material according to its mechanical properties and chemical composition [25]. Therefore, material characterization is an information bridge to assess the current situation and plan for superior properties and gain competitive advantage by innovative products and processes.

2.1. Advanced High Strength Steels in Automotive Industry

The automotive industry considers material manufacturing seriously in terms of production safety, cost, and light-weight materials. AHSSs that have at least a yield strength of 210 MPa have become the car industry's primary material. By increasing the yield strength higher than 350 MPa, the ductility and weldability of steel drastically reduces due to high carbon content. Instead, microalloying elements containing a small amount of nickel, vanadium, and titanium are designed to raise the yield strength up to 550 MPa [21]. The AHSSs include dual-phase, complex-phase,

structural and TRIP (Transformation Induced Plasticity) manganese-boron steels, combining their advantages by different microstructural constituents. They show excellent forming properties with high strengths having martensite in their structure. Dual phase (DP) steels have gained increasing attention due to their superior strength as well as light-weighting features, especially in the car industry [26]. DP-steels are low-carbon steels with a soft matrix (ferritic phase) and particles of a second hard phase (martensite) [27]. Transformation to martensite is diffusionless, and it occurs within high rates of cooling to surpass the diffusion-controlled transformation of austenite to ferrite, pearlite, or bainite in the Iron-Carbon equilibrium diagram. The martensitic transformation completes by shearing or cooperative movement of a huge number of atoms [28].

There are three different approaches to produce DP steels, which include (a) intercritical annealing of a ferritic-perlitic microstructure, (b) intercritical annealing of a quenched martensitic microstructure, and (c) austenitizing and intercritical annealing. All the three methods are followed by quenching in water [29]. Suppose the temperature increases during intercritical annealing of DP-steels, then the volume share of the martensitic phase raises. Consequently, it enhances the material's strength but weakens its ductility. Another critical factor in shaping DP-steels is time [30] [31]. Cold-rolled steel sheets are passing through several rollers in the roll-forming process to shape into the final format. Overall, cold-work affects the stress-strain diagram. The finished steel has a higher yield strength and lower ductility [32]. Generally, the DP-steels' strength value depends on the volume fraction and morphology of the martensitic phase in their microstructure. This class of steels' yield strength can be between 350-650 MPa. They have a microstructure containing more than 20 percent martensite islands dispersed in a ferritic matrix. Their carbon content is usually less than 0.2%, giving them a superior ability for RSW [33].

Another steel grade investigated in this research work is S690QL, a low-alloyed thermo-mechanically treated steel types with yield strength higher than 690 MPa and limited carbon content of 0.2% [34]. The steel grades are often used for structural applications are S355QL, S460QL and S690QL. The initial letter S in their names refers to structure, the following number shows their minimum yield strength, and QL shows that the fine grained steel is quenched and tempered [35].

2.2. Welding Technology for Advanced High Strength Steels

Due to the welding suitability of low-carbon steels in principle, the classical joining processes in automotive body construction include low-cost and effective methods such as resistance spot welding (RSW) and laser beam welding (LBW) [36]. A considerable challenge in welding technology is the microstructural changes at the joints of two steel sheets, which leads to undesired hardening or softening of the material in the local areas [37]. Therefore, research and development departments of automobile producers need accurate information about material properties.

Generally, a welded structure contains three different regions such as weld metal (WM), heat affected zone (HAZ) and the base metal (BM). The WM is the material that has been melted. Moreover, the changed microstructure of the material that has not been melted, is known as HAZ [38]. The high heat input primarily causes the underlying phase transformations in the WM and the HAZ during the welding process, affected by the high heating/cooling rates. As a result, the material behavior in the different zones of a welded joint may deviate from the BM. Martensite formation leads to increased hardness values, resulting in lower formability in the joining area [39].

RSW employs the heat generated through resistance against an electrical current to join surfaces. The contacting surfaces are heated up in the electrical current concentration region by short pulses of low-voltage, high-amperage to form a fused nugget of WM. The significant advantage of RSW is high operating velocity and suitability for robotization [40]. The working principle in RSW is as follows: two pin-shaped electrodes press the workpiece to be joined together. Electric current flows between the electrodes through the workpieces at a certain time. It heats the joint to the welding temperature, shaping a welded joint between two workpieces under mechanical pressure. If spattering can be seen at the welding point, it leads to severe electrode wear and ultimately to unusable welds. Therefore, the contact force between two workpieces should be neither too large nor too small because it strongly influences the resistance. Additionally, the electrode material should be rigid with low resistance and high thermal conductivity [41]. The diameter of the electrode pin is a function of the thickness of the steel sheet [38].

LBW uses a high-power laser beam as the source of heating for penetrating the weld joint. The main advantage of LBW comparing to RSW is its smaller distortion area and more flexibility in application [42]. LBW, in contrast to RSW, is a non-contact welding process. This process's heating/cooling rate is so fast that the HAZ is smaller in comparison to other conventional welding method [38]. The workpiece absorb the laser beam until the metal melts and then the material vaporizes partially, and a narrow keyhole is formed, which can be up to 3 mm deep depending on used material and the power of laser beam. The metal vapor should be extracted or blown away because it can interfere with the laser beam [43]. The laser-active medium can be performed with solid-state or gas lasers. For example, a solid-state laser with an active medium made from single crystal (Nd:YAG) is widely used for thinner steel sheets, when the plate thickness is less than 3 mm [38].

Welding leads to a significant change in the mechanical properties of a component, so that the conventional tensile test cannot be used as a standard method for determining material data. Therefore, in this research work, a methodology is developed to characterize the mechanical properties of welded joints without tensile testing. However, as a first step, it is necessary to explain the traditional approaches and the importance of material characterization.

2.3. Characterization of Material Mechanical Properties

The material information, measured by applying the external force in the solid-state material, is called the mechanical properties [11]. The deformation and fracture characteristics under applied stresses (tensile, compressive, or multiaxial) describe materials' mechanical behavior [44]. This physical behavior is simply represented by the relationship between the stress and the strain of a material on a macroscale which usually is depicted in the stress-strain diagram [11]. Brittle materials such as oxides, amorphous carbon coatings, and single crystalline silicon follow the fracture mechanics in elastic region. It means that the sample broke after exerting linear elastic loading without any considerable plastic deformation. On the other hand, semi-brittle behavior of materials such as steels which are ductile materials can only be explained by elasto-plastic fracture mechanics [45]. The stress-strain diagram of metals, particularly steel, offers two different behaviors: elastic and plastic zones [46].

The Young modulus expresses the relationship between the stress and the axial strain in the elastic range, which is achievable by applying external tensile force. By removing the external loading, the elastic strain recovers completely. Therefore, the elastic modulus is merely quantified by calculating the tangent of the elastic recovery line [47]. The deformation and strain of steels in other directions perpendicular to the applied external force in a complex structure can be determined by Poisson's ratio in the elastic region [48]. Furthermore, a structure undergoes plastic deformation when the tensile stress goes beyond the yield strength. The yield strength is the point where the straight elastic recovery line ends, and the non-linear plastic curve begins. The plastic deformation is permanent and survives even after the external force is removed [49].

A traditional and still widely used method for determining the stress-strain diagram is the uniaxial tensile test [12]. For this purpose, in the first step, a dog bone tensile specimen in a particular size should be prepared from homogeneous material according to the guideline [50]. Subsequently, the sample should be fully clamped from both sides, and the test should be completed under the ideal conditions and experimental setup [51, p. 2016]. The displacement, stress, and associated strain are then recorded at each time step and finally represented in the stress-strain curve [51, p. 2016]. The engineering stress-strain curve cannot fully describe the deformation characteristic of metal since it relies on the original dimensions of the samples, however, the sample dimensions continuously change during the tensile test. Besides, the ductile material pulled from both sides in the uniaxial tensile test becomes unstable and necks down. A correction is needed to calculate the true stress-true strain curve. On the other hand, the true stress-strain curves increase continuously to fracture point by considering the actual stress based on the real cross-sectional area of the specimen [44]. Figure 2.1 shows the engineering and true stress-strain curves of an AHSS in different loading phases.

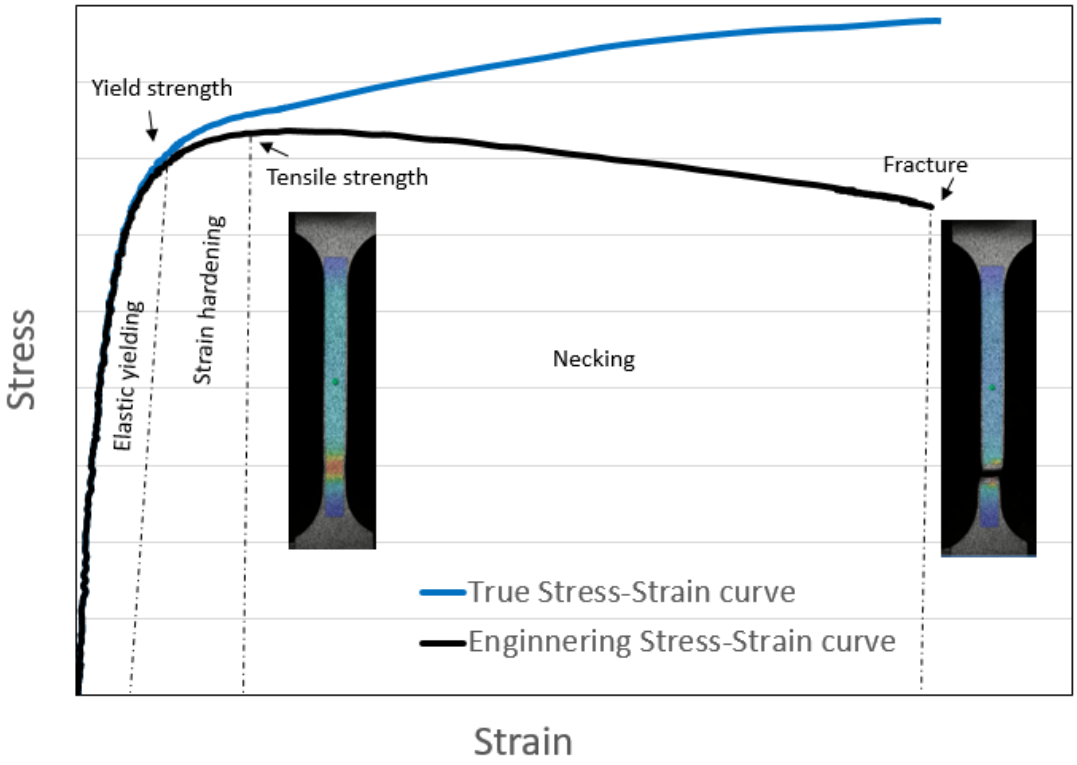

Figure 2.1 A Comparison between engineering and true stress-strain curves in different loading ranges, such as the elastic zone where the magnitude of the stress is less than the yield strength, the strain hardening that occurs up to the tensile strength, and the necking that begins from ultimate strength up to fracture

Material behavior in the plastic region is complex and can be defined by the differential equations, a so-called material model, with one or several internal parameters. The elastic-plastic material model can have different forms based on non-linear isotropic or kinematic hardening parameters. It is hugely time-consuming to calculate their internal parameters and, at the same time, a critical factor in describing the structural behavior as accurately as possible [52]. Besides the internal parameters, knowledge about the ultimate tensile stress and failure strain of material is required to explain the material behavior when it collapses [53]. The area under the curve in the stress-strain diagram related to the elastic-plastic region indicates the amount of energy material absorbs and its toughness [54]. The material data is a unique property of each steel type and describes the overall behavior of material from the early (elastic region) to the final step (plastic region and then failure) after applying an external force [55].

As the uniaxial stress rarely occurs in an industrial application, the multiaxial stress state can be replaced by a uniaxial equivalent stress which can be calculated according to von Mises yield criteria. The plastic behavior of an isotropic material can

be expressed as a yield function which specifies conceivable states on the spanned coordinate system with different axis. The elasticity range can be defined, when the amount of yield function is equal to zero. As soon as the stress state touches the yield surface and becomes bigger than the yield function, the material plasticizes [56]. During the plastic deformation, the yield surface grows along due to the material strain hardening, where its shape, size, and position can alter. In this case, the yield function depends on plastic comparative strain which is determined according to von Mises' law. In isotropic hardening, the yield surface grows symmetrically about the origin and the shape as well as the flow surface size change uniformly in all directions, however, the position of the axis remains similar. Conversely, in kinematic hardening, the flow surface shifts from the origin, but its shape and size remain the same. The mathematical description of nonlinear isotropic hardening can be quantified by Voce [57] as shown in the Equation (2.1) according to Figure 2.2 with the assumption that the stress will reach a maximum value.

$$\sigma = \mathrm{R_{p0.2}} + \mathrm{R_0} \cdot \varepsilon_{\mathrm{pl}} + \mathrm{R_\infty} \cdot (1 - \mathrm{e}^{(-\mathrm{b} \cdot \varepsilon_{\mathrm{pl}})}) \tag{2.1}$$

According to this material model, the Equation has four parameters of $R_{p0.2}$, R_0, R_∞, and b. In this Equation, $R_{p0.2}$ (MPa) is the amount of yield strength. σ (MPa) shows the amount of stress at corresponding equivalent plastic strain (ε_{pl}). In the material model, R_0 (MPa) stands for the tangent of the line in the stress-strain diagram in the plastic region or the linear hardening coefficient. Furthermore, R_∞ (MPa) shows the difference between the yield stress and the maximum value of stress or exponential hardening coefficient. The exponential saturation rate is described with the material parameter of b. The Voce material model follows the von Mises/Hill yield criterion and associative flow rule for describing the nonlinear isotropic hardening in an exponential form and the yield function can be defined as:

$$F = \left[\frac{3}{2}\{S\}^T[M]\{S\}\right]^{\frac{1}{2}} - \sigma = 0 \tag{2.2}$$

In Equation (2.2), F and {S} stand for the yield criterion and deviatoric stress, respectively. M is the constant matrix used as a multiplier when the accumulated plastic work must be calculated over the total time of loading. Furthermore, the accumulated equivalent plastic strain (ε_{pl}^{acc}) and its increment ($\Delta\varepsilon_{pl}^{acc}$) can be calculated from Equation (2.3) and (2.4) as:

$$\{\Delta\varepsilon_{pl}^{acc}\} = \frac{3}{2}\gamma\frac{\{S\}}{\sigma_e} \tag{2.3}$$

$$\varepsilon_{pl}^{acc} = \sum\sqrt{\frac{2}{3}\{\Delta\varepsilon_{pl}^{acc}\}^T[M]\{\Delta\varepsilon_{pl}^{acc}\}} \tag{2.4}$$

In Equation (2.3), the parameter γ and σ_e stand for plastic multiplier and equivalent stress, respectively. In addition, the isotropic hardening material model has been further developed by considering the power hardening law based on the Gurson [58] and Tvergaard and Needleman [59] material model to describe the ductile plasticity, as seen in Equation (2.5):

$$\frac{\sigma_Y}{\sigma_o} = \left(\frac{\sigma_Y}{\sigma_o} + \frac{3G}{\sigma_o}\bar{\varepsilon}^{pl}\right)^N \tag{2.5}$$

In Equation (2.5), the parameters σ_Y and σ_o stand for current and initial yield strength, respectively. The other parameters, G and N show the shear modulus and stress ratio, accordingly. Finally, the parameter $\bar{\varepsilon}^{pl}$ can be calculated based on the porosity, macroscopic plastic strain and Cauchy stress tensor and defines the microscopic equivalent plastic strain. However, the current research work focuses only on the determination of the martial model parameters of Equation (2.1), as shown in Figure 2.2, which is able to describe the material behavior of AHSSs in quasi-static tensile test with a high accuracy, which will be discussed in the next chapter.

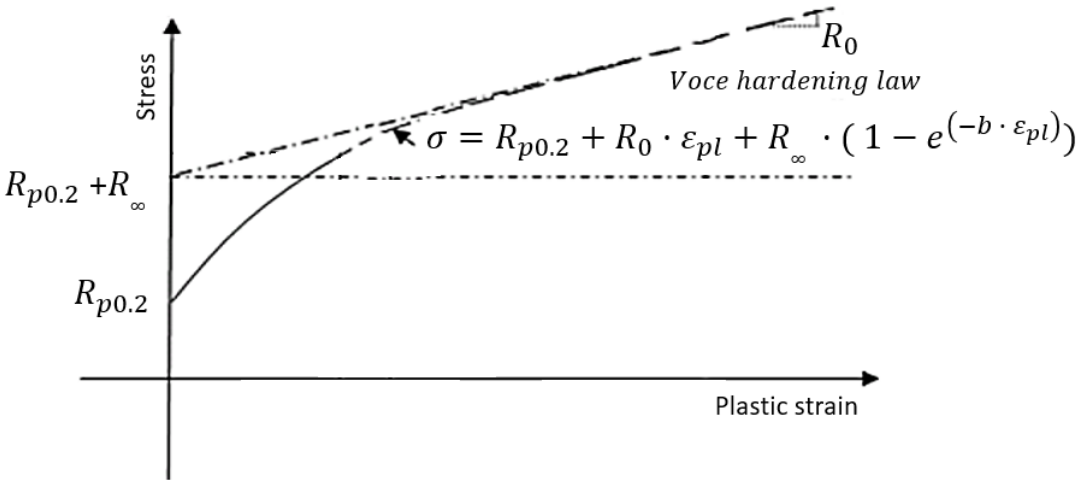

Figure 2.2 Parameters of the Voce non-linear isotropic hardening model [60]

The parameters of the Voce material model can be identified by performing a tensile test, however, the major challenge with preparing a uniaxial tensile testing specimen is that a sufficient material volume must be available to produce the defined tensile specimens. It is easily possible to construct samples from conventional materials such as plain steels. Various manufacturing processes are widely used in the industry, such as welding and grinding, to produce a final product, lead to inhomogeneity and local changes in used materials. For example, a welded structure contains three entirely different areas: the weld metal, heat affected zone (HAZ), and the base material [61]. Each region has completely different mechanical properties and may not have enough dimensions to make a tensile specimen.

Another approach can be to produce a notched tensile specimen from the welded steels, with the notch located exactly in WM, to force fracture to occur at this point [62]. It was found [63] that it is possible to calculate the true stress of a smooth tensile specimen from the notched tensile specimens according to the following equations:

$$\sigma_{true}^{Smooth}(\varepsilon) = \sigma_{true}^{Notched}(\varepsilon)/G \tag{2.6}$$

$$\mathrm{G}_{n=0.1} = 1.007 + 0.18777\left(\frac{D_o}{R_o}\right) - 0.01313\left(\frac{D_o}{R_o}\right)^2 \tag{2.7}$$

$$\frac{\mathrm{G}_n}{\mathrm{G}_{n=0.1}} = 1.053 - 053\varepsilon_{P_{max}} \tag{2.8}$$

The parameter G in Equation (2.6) stands for the geometry factor and depends on the initial diameter (D_o) and notch radius (R_o) of the notched tensile specimens. However, the size of the geometry factor can be changed depending on the value of strain hardening (n) and can be calculated from Equation (2.8). On the other hand, Equations (2.6) to (2.8) apply to the tensile specimens with the special geometry and the variation of the tensile specimen size may affect the applicability of the mentioned formulas.

Besides, the tensile test, as a destructive technique, includes uncertainty in the final result. As a rule, the test must be repeated at least three times, and the deviation among the results can be up to ten percent [64]. Therefore, an alternative method is required to determine the material data when a product or structure contains

inhomogeneous material. Consequently, the new alternative approach should satisfy these key features:

a. This technique should be applicable to the local areas on the target material when the phase material is small, such as a welded zone
b. It should reduce the burden to produce the tensile specimens
c. It should have proper accuracy
d. The new method should not be destructive

Although the conventional uniaxial tensile test is a destructive technique, other approaches such as ultrasonic [65] or electromagnetic methods [66] are non-destructive and can be employed to identify the local material parameters. The effects of residual stresses or the magnetic field during the specimen preparation should be considered when measuring material parameters. On the other hand, they cannot fully predict the stress-strain diagram of a material. It is possible to obtain local material data entirely from hardness measurement, as an in-field and minor destructive test. This widely used approach in industry will be developed further in this research work.

2.4. Alternative Methods for Material Characterization

One of the first attempts to establish a relationship between the hardness measurement and the stress-strain diagram of the material was conducted by Tabor in 1951 [15]. He found a correlation between the applied force, the indenter size, and the corresponding relative strain on the specimen's surface after indentation measurement [15]. The hardness measurement with instrumented indentation technique (IIT) is more efficient in collecting comprehensive data to make a more accurate correlation [19]. One of the main differences between the conventional hardness measurement and the instrumented indentation test is that the force should be steadily imposed on the surface of a specimen in IIT, then slightly removes over a while. The applied force and the corresponding indentation depth in loading and unloading are continuously recorded, followed by plotting as the force-indentation depth diagram [67].

Furthermore, nanoindentation test can simultaneously measure the loads as small as 1 nN with depth evaluation in the 0.1 nm range [68]. It is recommended to employ a

spherical indenter, which is more resistant to deformation than the test specimen. For instance, a polished tungsten carbide when performing the IIT is a proper choice. Furthermore, the test must be completed at room temperature while the loading should be kept between 2N and 3kN. The depth of the plastic deformation under the indented surface is around ten times more than the indentation depth. Consequently, the obtained material data determines this area's mechanical properties and not the bulk of material [69].

The IIT machine must have enough equipment to isolate the test sample from the temperature changes and potential external noises as well as vibrations. The proper sensors must be installed to record and measure the force, the penetration depth on the specimen surface, and the time in each test cycle. The machine must also have the ability to provide the power in several loading and unloading cycles [70]. The typical radius of the spherical indenter is between 200 and 500 μm [71]. The smallest distance between the individual indentations must be ten times bigger than the indentation radius. Suppose the indentation is performed beside the specimen edge. In that case, the distance between the first indentation and the border must be six times bigger than the indentation radius. Besides, the specimen surface must be prepared so that its roughness should become less than 0.1% of the penetration depth [72]. It is observed that IIT can be performed not only on the blank samples but also on coated specimens [73]. A schematic representation of the IIT system head components from universal hardness testing machine ZHU/zwicki-Line which contains load cell, an indenter and two measuring sensors are presented in Figure 2.3.

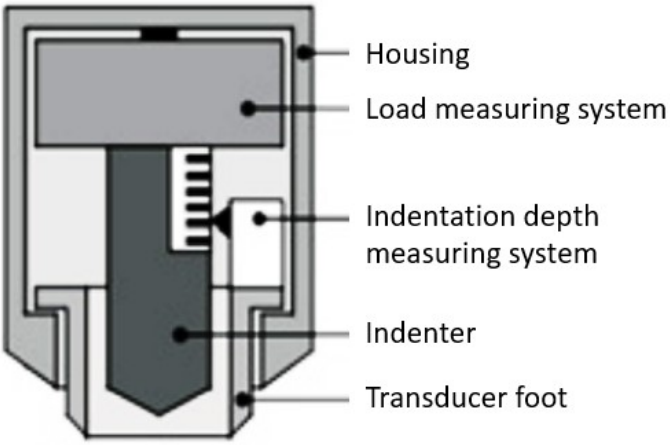

Figure 2.3 Schematic representation of instrumented indentation testing (IIT) system head from ZHU/Zwicki-Line universal hardness testing machine. The components include an indenter with a specific geometry with the maximum diameter of 10 mm for the application of Brinell hardness testing which is mounted on a rigid column, through which the load is applied, and two sensors that measure the indentation displacement and the force [74]

The resulted force-indentation depth curve from the IIT can be correlated to material data with three main different methods. First, by using the analytical approaches which correlate the changes in the surface of the indented samples to mechanical properties. Another approach is applying the inverse numerical calculation to find the best possible input data as the material parameters of the indented sample. The last main methodology is using the artificial neural network to correlate the force-indentation depth diagram to mechanical properties of samples. It is necessary to know each approach individually for any further development of a new methodology.

2.4.1. Representative Stress and Strain

The resulting Force-Indentation depth diagram, driven from the IIT approach by considering multiple loading and unloading phases and increasing the amount of maximum force ($F_{max}(i)$) and indentation depth ($h_{max}(i)$) at each cycle (i), as shown in Figure 2.4, can be analytically correlated with the mechanical properties of a given material in the form of the stress-strain diagram. The area under the force-indentation depth diagram shows the total indentation work (W_i), which is composed of elastic (W_i^e) and plastic (W_i^p) work. As seen in Figure 2.4, the elastic work can be calculated considering the area under the unloading path and the area remaining between the

loading and unloading paths shows the plastic work and can be influenced based on the speed of the applied load [75].

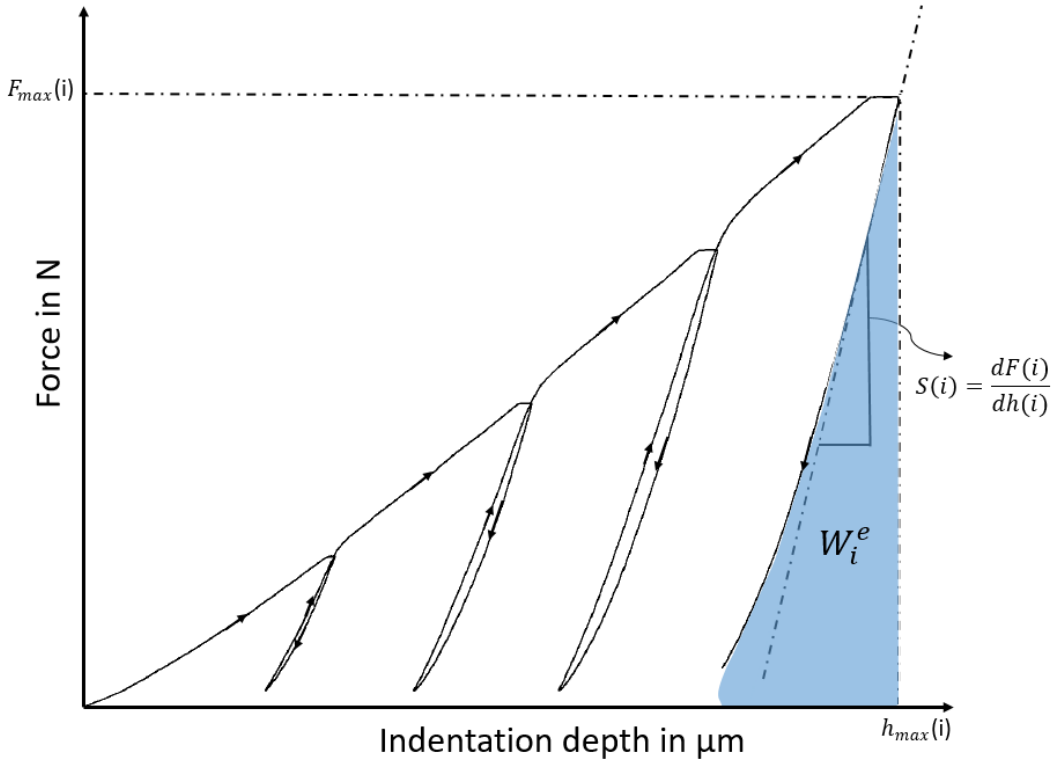

Figure 2.4 Force-Indentation depth diagram with several loading and unloading phases and increasing the amount of maximum force ($F_{max}(i)$) and indentation depth ($h_{max}(i)$) at each load cycle (i) and elastic work under the unloading path (W_i^e) as well as the initial unloading slope (*S(i)*)

In order to calculate the stress-strain diagram, the key parameters that describe the contact between the indenter and specimen, such as the deformation height (pile-up) or depth (sink-in) and the total contact area and the contact angle should be firstly measured as shown in Figure 2.5. The pile-up or skin-in almost always occurs during penetration on the surface of the indented specimen and is mainly influenced by the material parameters such as Young's modulus, strain hardening exponent, and friction coefficient [76]. When the surface is exposed, the area below the indenter applies stress and it begins to deform elastically at first and then plastically. However, due to strain hardening, the strength in the area contacted by the indenter also increases with the stress and the area which is softer, deforms plastically. Ductile material tends to pile-up as less consolidation occurs and the material with larger consolidation exponent to sink-in [77].

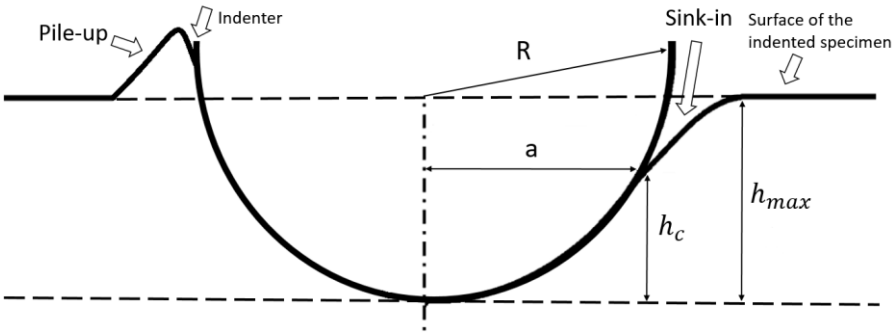

Figure 2.5 Schematic profile of the indented surface after performing of the indentation test by considering the pile-up and sink-in phenomena with indentation depth (h_{max}) and contact depth (h_c)

The next step is to calculate the stress and strain based on the contact parameters and then gather them in a material model [78]. The representative true stress ($\sigma(i)$) and true strain ($\varepsilon(i)$) can be calculated from the sink-in geometry based on the parameters introduced in Figure 2.4 and Figure 2.5 as presented in [18] according to [79] [16].

$$\sigma(i) = \frac{1}{3.5}\frac{F_{max}(i)}{\pi c(i)^2} \tag{2.9}$$

$$\varepsilon(i) = 0.12\frac{c(i)}{R\sqrt{1-(\frac{c(i)}{R})^2}} \tag{2.10}$$

$$c^2(i) = \frac{2}{5}\left(\frac{2-n_{in}}{4+n_{in}}\right)\pi a^2 = \frac{2}{5}\left(\frac{2-n_{in}}{4+n_{in}}\right)(2Rh_c(i) - h_c^2(i)) \tag{2.11}$$

$$h_c(i) = h_{max}(i) - \frac{3}{4}\frac{F_{max}(i)}{\left(\frac{dF(i)}{dh(i)}\right)_{F_{max}(i)}} \tag{2.12}$$

$$\sigma(i) = \ln K + n\ \ln\varepsilon(i) \tag{2.13}$$

In Equation (2.11), the projected contact section between the indenter and the specimen is presented with πa^2 as shown in Figure 2.5. The initial unloading slope ($\left(\frac{dF(i)}{dh(i)}\right)_{F_{max}(i)}$) in Equation (2.12) stands for the contact stiffness and depends on the geometry of the contact area and surface roughness [80]. It can be assumed that the parameters (n_{in}) from Equation (2.11) and (n) from Equation (2.13) can be approximately equal and represent the work hardening exponent from the indentation

test and the stress-strain curve, respectively. It is first necessary to calculate the representative true stress and true strain from Equation (2.9) and Equation (2.10) to later determine the variables K and n in Equation (2.13). Then, the representative true stress and true strain must be recalculated with the already computed parameter (n) in a repetitive process to determine the most accurate n and K, and thus the yield strength [18].

An observation demonstrated that it is possible to analytically calculate the stress and corresponding strain at several points beyond the yield strength, sufficient to determine the desired material model [16]. Besides, the yield strength and ultimate tensile strength of various materials were calculated with an accuracy of up to 5% using the representative stress and strain method [81]. There is enough experimental work to demonstrate the robustness and trustworthiness of this method, the simplicity of using its algorithms, and there is no further need for complicated numerical simulation. However, this method is not flexible enough and cannot predict the yield strength of AHSSs [18]. Moreover, it does not have any other solution to calculate the other necessary theoretical material data [17].

2.4.2. Inverse Analysis by means of Finite Element Method

In addition to the representative stress and strain method, the stress-strain diagram of a material can be estimated with the inverse analysis through FEM. In this repetitive approach, the goal is to find the most accurate estimation of the material data using a trial and error procedure. In this regard, the force-displacement curve can also result from an infinite number of combinations of material parameters. Inverse analysis employs FEM calculations to select parameters and consequently the deviation of force-penetration curve between experimental results and FEM simulation should be minimal. FE model iteratively computed until a match is found with the experimental force-penetration diagram. Therefore, the infinity possibilities of parameter combinations are limited to the force-displacement curve.

An approach used in several works [82] [83] to determine the material parameters from the force-indentation depth diagram with inverse analysis technique is applying Kalman filter algorithm [84]. This methodology has been used in various fields such as manufacturing and signal processing to solve the inverse problems [85], in addition

to being used in computational mechanics to identify the parameters of nonhomogeneous material model [86]. The Kalman filter theory can be described with the following equations.

$$x_t = x_{t-1} + K_t[z_t - H_t(x_{t-1})] \tag{2.14}$$

$$K_t = P_t h_t^T R_t^{-1} \tag{2.15}$$

$$P_t = P_{t-1} - P_{t-1} h_t^T (h_t P_{t-1} h_t^T + R_t)^{-1} h_t P_{t-1} \tag{2.16}$$

In Equation (2.14), the x_t stand for the vector of unknown measured parameters at updating step t. For instance, vector x_t contains the target material model parameters at increment t such as elasticity modulus or yield strength ($x_t = [x_i]_t$). The vector z_t and H_t describe the experimentally measured parameters and the relationship between the measurable parameters and the quantities that indicate the state of a material, such as material constants. For example, vector z_t contains the magnitude of measured displacements with its corresponding measurement error at a specific load step, however, the elements $(H_j)_t$ of vector H_t show only the exact value of displacement [82]. The vector of unknown parameters must be calculated in an iterative process considering the correction factor, which can be calculated by the Kalman gain matrix K_t as shown in Equation (2.15). The matrix h_t is the gradient of matrix H_t according to the unknown parameters at step t as shown in Equation (2.17) and must be defined before starting with the calculation [83]. The matrix P_t and R_t are the measurement and error covariance matrix at increment step t as described in Equation (2.18) and Equation (2.19).

$$h_t = \frac{\partial [H_j]_t}{\partial [x_i]_t} = \begin{pmatrix} \frac{\partial (H_1)_t}{\partial (x_1)_t} & \cdots & \frac{\partial (H_1)_t}{\partial (x_i)_t} \\ \vdots & \ddots & \vdots \\ \frac{\partial (H_j)_t}{\partial (x_1)_t} & \cdots & \frac{\partial (H_j)_t}{\partial (x_i)_t} \end{pmatrix} \tag{2.17}$$

$$P_o = \begin{pmatrix} ((x_1)_{max} - (x_1)_{min})^2 & \cdots & 0 \\ \vdots & \ddots & \vdots \\ 0 & \cdots & ((x_i)_{max} - (x_i)_{min})^2 \end{pmatrix} \tag{2.18}$$

$$R_t = \begin{pmatrix} (R)^2 & \cdots & 0 \\ \vdots & \ddots & \vdots \\ 0 & \cdots & (R)^2 \end{pmatrix} \tag{2.19}$$

In another approach to calculate the material parameters with inverse analysis, a validated and as precise as possible numerical simulation model of the indentation test within the range of all boundary conditions must be prepared. The indentation test should then be performed on the desired samples and then in an extraordinarily time-consuming and numerically expensive procedure, the simulation model's material model parameters have to be arbitrarily and repeatedly changed to find the best match between the force-indentation depth diagrams of the IIT, which are separately obtained from the experimental and numerical work. In other words, the output is known, and the input must be modified in such a way to calculate the desired result [87].

This means that the goal must be to minimize the mean square error (MSE) between the output of the numerical model and the experiment, as shown in Equation (2.20). In another work [88], it was proposed to normalize the squared error based on the value of the experimental output to give equal importance to each output, as shown in Equation (2.21). Additionally, such an approach can benefit from constrained optimization routines if additional information such as the value of elastic modulus or yield strength can be estimated in advance [89].

$$MSE = \frac{1}{n}\sum_{i=1}^{n}(output_{experiment} - output_{simulation})^2 \tag{2.20}$$

$$Error\ criterion = \sum_{i=1}^{n}\frac{(output_{experiment} - output_{simulation})^2}{output_{experiment}} \tag{2.21}$$

However, it is possible to optimize the procedure by finding the best guesses in each step to reduce the total calculation time. For example, several representative points must be chosen from the experimental force-indentation depth curve to begin with the inverse analysis. The first numerical simulation is performed by guessing the material data. The rest of the simulation, belonging to other successive points, depends on the first simulation's accuracy. The procedure must be continued step by step to draw the entire force-indentation depth curve. This method can become more efficient if the first guess is made based on the previous information [90]. In another complementary process, the focus is more on some other parameters such as indenter shape, the actual contact area between the indenter and the surface, as well

as penetration force and pressure [91]. For instance, several indentations must be performed and the curves must be normalized according to a specific parameter such as pressure. The experiment's results in curves and inverse numerical simulation have to be matched in a single diagram [92].

Contrary to the representative stress and strain method, the inverse analysis approach is flexible enough to be applied to different materials such as ceramics and even the specimens with the coated surface or various forms of the indenters spherical or conical shape is used [93]. The drawback of this method is that if the first guess is not close enough to the real material data, the rest of the simulation to estimate the mechanical properties as accurately as possible will be numerically expensive and time-consuming.

2.4.3. Artificial Intelligence and Material Data

In addition to the first two methods, the force-indentation depth diagram can be associated with the stress-strain diagram employing a trained artificial neural network (ANN). Attempts to use the ANN to determine the material data have been significantly developed at the end of the last century [94]. It became clear that the ANN is a strong and powerful tool for solving the inverse and complicated problems in mechanical engineering [95].

The artificial neural network, known as the most accurate and robust machine learning algorithm, was first introduced in 1943 when scientists attempted to map the brain function into a mathematical and then a computer model [96]. A couple of years after the introduction of ANN, it was expected that many complex technical problems could be solved by this novel method, and even that it could overtake and control all aspects of humans life. However, due to some fundamental aspects of the early model of the ANN, known as symbolic AI, it could not meet the expectations, and ANN lost its popularity at the end of the last century. Symbolic AI is a strong tool for solving problems based on a set of rules, such as chess or backgammon. It means that the developer can define a set of rules or the rules' regulations initially, and the AI can then act based on them. On the other hand, it could not solve the complex and fuzzy problems such as recognizing a specific object in an image [97]. The next phase in the development of AI occurred in 1980 when the concept of the Expert System

and the LISP programming language were introduced to solve complex problems based on conditional rules [98].

Neural networks can be viewed as directed graphs that transmit data along directed connections as seen in Figure 2.6. According to how data transmission works, there are two types of neural networks. If there is only one direction, forward, from the input neurons to the output neurons, it is called a feed-forward network. If it contains loops or directed circuits, it is called a recurrent network. The neurons in the input layer distribute the input data to the neurons in the next layer, while the hidden layer has no contact with the environment and may contain multiple hidden layers. The output neurons provide the output data. A nonlinear mapping can be shaped in hierarchical ANNs from multiple input data to multiple output data by using a learning process. Therefore, the network should be trained with different patterns containing input and output data. The current ANN is capable of generalization, a kind of interpolation so that the trained network can estimate the results even for unlearned examples and can operate quickly in the application phase [99].

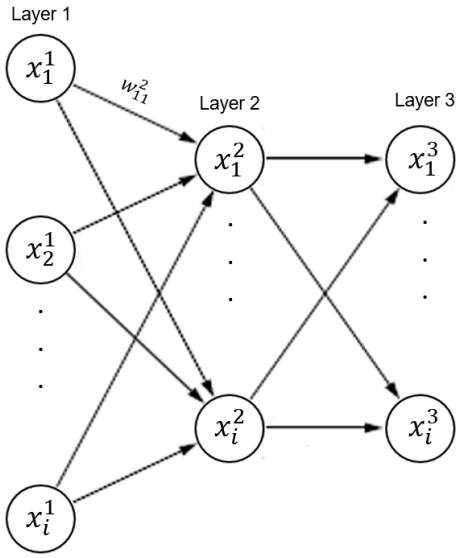

Figure 2.6 Schematic representation of a feed-forward ANN with three layers such as input layer (Layer 1), hidden layer (Layer 2) and output layer (Layer 3) and features of input dataset (x_i^1), outputs (x_i^3) and an example of weight between each neurons (w_{11}^2)

The mathematical description between the input and output of the ANN as depicted in Figure 2.6 can be shown in Equations (2.21) to (2.23). Equation (2.21) shows a logistic function as an example of sigmoid function to make the linear regression term ($b + w^T X$) nonlinear. In the linear regression, the vectors *X* and *w* represent the input

and the weight, respectively, and the bias is shown by the parameter b. Equation (2.22) shows the cost function that results from the mean square error between the target value and the calculated output of the logistic regression. The most accurate value of the weights leading to a minimum value of the cost function can be calculated based on the standard gradient descent method with learning rate of $\propto$ in an iterative process as shown in Equation (2.23). The most critical point in the learning process is to improve the optimization algorithm by using other methods such as stochastic or batch gradient descent to minimize the cost function to find best possible weights by reducing the calculation time.

$$f(X) = \frac{1}{1 + e^{-(b+w^T X)}} \tag{2.21}$$

$$J = \frac{1}{n}\sum_{i}(y_i - f(x))^2 \tag{2.22}$$

$$\mathrm{w} = \mathrm{w} - \propto \nabla \mathrm{J}(\mathrm{w}) = \mathrm{w} - \propto \left(\frac{\partial \mathrm{J}}{\partial w_1}, \ldots, \frac{\partial \mathrm{J}}{\partial w_N}\right) \tag{2.23}$$

Of all the AI developments, the revolution in machine learning took place around 2012, when it became possible to perform the calculations with the graphical processing units (GPU). The GPU significantly reduces the artificial neural network's expensive computation time with the backpropagation algorithms, known as a deep neural network [100]. The main distinction between the traditional machine learning algorithms and deep neural network is that the accuracy in modern ANN is significantly increased by having more datasets. However, the accuracy becomes greater when there are more datasets in the traditional version only in the beginning. It then remains constant even when the training datasets are increased. For instance, AlexNet applied a deep neural network with enough datasets to improve image recognition accuracy by about 10% to 83.6% [101]. Following this remarkable development in machine learning, AI has been applied to other fields such as text mining, speech recognition, and even mechanical engineering, particularly material characterization, to revolutionize them too, as explained in [102] [103] [104] [105] [106].

The question which arises at this point is that what the backpropagation algorithm is. As a supervised learning algorithm that contains multiple layers such as input, hidden,

and output in a row, ANN relies on the input and output to begin with the training process. In the training procedure, the goal is to find the correct variable between the layers, called weight, so that the error between the ANN's output and the actual results becomes minimal. If the weight of a neuron or input is greater than the weight of other neurons or inputs, this specific input influences the final calculated outputs compared to the other input data. In a simple forward method with two output and input layers, the input values are multiplied by the randomly chosen weights and summed together to calculate the outputs. Then, in the backpropagation method, the calculation must be done from the outputs toward the inputs, which should remain constant and not be changed. In this step, the backpropagation algorithm uses an optimization algorithm such as gradient descent to change the weights and biases to make the differences between the desired and calculated outputs for each dataset minimal as shown in Equation (2.24) and Equation (2.25). In the following equations, *l* and *i* stand for the layer and the neuron at layer *l* and w_{ik} represents the weight between neuron *i* and *k* in different layers. This numerically expensive procedure must be repeated repeatedly with each training dataset to find the best value of the weights that leads to the most accurate value of the computed outputs [107].

$$\frac{\partial \mathrm{J}}{\partial w_{ik}^{l}} = \frac{\partial \mathrm{J}}{\partial f_{i}^{l}} \frac{\partial f_{i}^{l}}{\partial w_{ik}^{l}} \tag{2.24}$$

$$\frac{\partial \mathrm{J}}{\partial b_{i}^{l}} = \frac{\partial \mathrm{J}}{\partial f_{i}^{l}} \frac{\partial f_{i}^{l}}{\partial b_{i}^{l}} \tag{2.25}$$

Yagawa demonstrated in detail the advantages of the neural network over conventional algorithms in computational mechanics to solve structural analysis issues, damage mechanics of welded structures, material modeling, and numerical simulation [99]. It has been shown that a trained ANN can predict the value of Poisson's ratio by considering a simple material model that describes plasticity and under one-time loading and two-times unloading [20]. Moreover, changing the input datasets and the ANN's architecture leads to a more precise estimation of the Poisson's ratio [108]. In another work, three internal parameters of a complex viscoplastic material model based on the Chaboche work has been identified by ANN [109]. The robustness and trustworthiness of the trained ANN have been proved when it was used to predict the elastic modulus, yield strength, and the parameters of the viscoplastic model of different materials [110]. In another study, the ANN was

trained with the datasets obtained from numerical simulation to predict a purely kinematic and isotropic model [111]. In another investigation, a friction stir welded aluminum plate's mechanical properties with a thickness of 3 mm were quantified by a trained ANN. The results were then compared with material data obtained from the tensile test performed on the micro specimens produced from the weld seam [102]. Furthermore, it has been shown that a trained conventional neural network is capable of estimating the mechanical properties of a mineral material using the images captured by scanning electron microscopy from its structure at mesoscale [112]. In related research, artificial intelligence was used to establish a correlation between a composite structure's material data and the images taken from its complex microstructure [103].

Similarly, the chemical compositions and the process parameters in the production line of a hot rolled steel were used as the conventional neural network's input data to determine the mechanical properties. The results show a strong dependency between the amount of carbon content and the value of tensile strength. Moreover, the yield strength is dependent on the finishing rolling and coiling temperature [104]. In addition, deep learning was used to calculate the effective thickness of a shell element and the tensile strength of a steel structure with an H-section. The used conventional neural network was validated by polling and extracting the feature layers and evaluating the accuracy level [105]. A modified and developed conventional neural network was applied to predict the concrete's residual stress using the images captured from its microstructure with a portable digital microscope [106]. Moreover, the mechanical properties of different material types such as woods, cardboards, and plastics were identified using a microwave sensor and analyzing the collected data with machine learning algorithms [113]. Furthermore, Ullner shows that the available neural network and the analytical methods (representative stress-strain method) fail significantly to predict steel structures' mechanical properties when their yield strength is higher than 400 MPa. Any estimation of the welded steels' material data in both BM or WM with yield strength higher than this value leads to a dramatic difference between the result of the ANN and the tensile test as a reference value, as seen in Figure 2.7. Moreover, he shows that the result of the analytical approach known as the representative stress-strain method deviates significantly from the measured values of the tensile test when it is applied to estimate the mechanical properties of the welded AHSSs which have yield strength greater than 400 MPa and

1000 MPa in BM and WM, respectively. The investigation is performed on the TRIP steel HCT690T with the yield strength of 400 MPa on both BM and WM produced by RSW. The output of ANNs and analytical methods are compared with the result of tensile test on BM and the heat-treated and then quenched material of HCT690T [18].

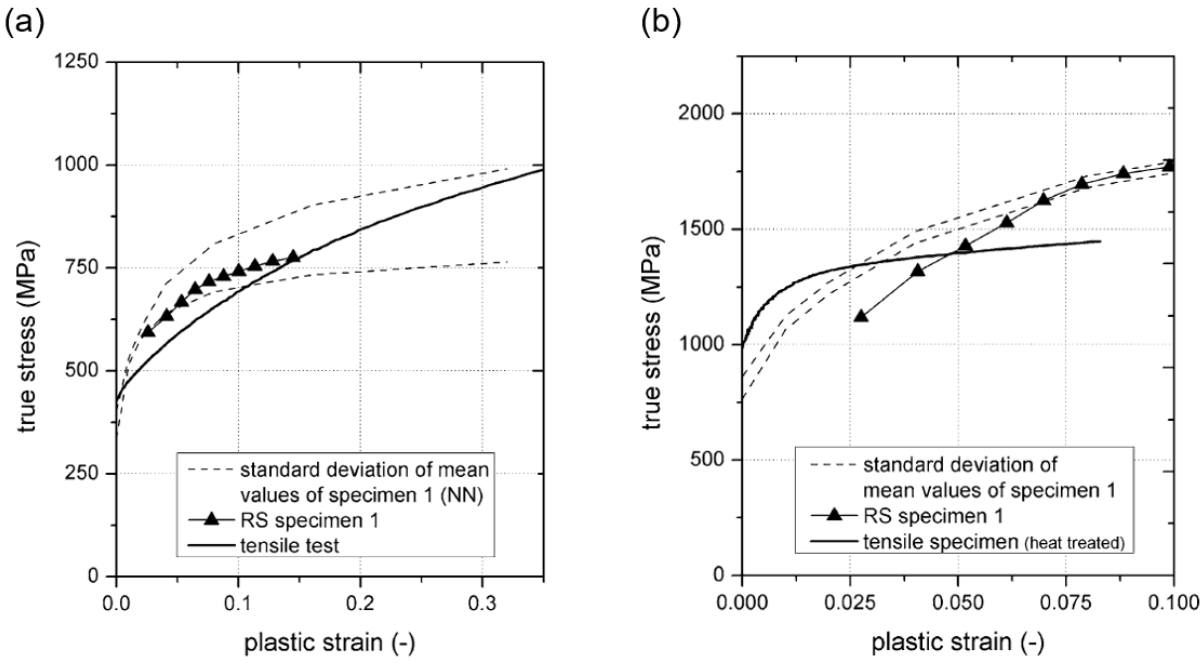

Figure 2.7 Comparison between the calculated stress-strain diagram from the representative stress-strain method (RS specimen) and the predicted material data using the current available neural network (NN) with the tensile test as a reference value; (a) all materials used are the base material of AHSS (HCT690T); (b) tensile tests are carried out on heat treated metal of AHSS (HCT690T) which is heated to 1200 ℃ and then immediately cooled with water, the indentations are performed on the weld seam of RSW made of HCT690T [18]

Consequently, the observation that the current and available ANNs and the representative stress-strain method (analytical approach) cannot predict the material data of AHSSs when the yield strength is higher than 400 MPa is the research question of the current work. The objective of the present work is to train ANNs capable of predicting the mechanical properties of welded AHSSs in different welded zones such as BM, WM or HAZ together with the IIT data. Therefore, DP steels and a high strength fine grained structural steel (S690QL) as commonly used AHSSs with yield strength higher than 350 MPa are used in the current research to examine the performance of the trained ANNs. The first step to achieve this goal is to determine the mechanical properties of the AHSSs used, which will be performed in the next chapter.

3. Material Characterization with Tensile Test

Among the various welding technologies, resistance spot welding (RSW) and laser beam welding (LBW) play a significant role in the automobile industry's joining methods. The application of those technologies for the automotive body alters the microstructure in the welded areas. It is necessary to identify the mechanical properties of the welded advanced high strength steels (AHSSs) to be able to make a reliable statement about the material behavior and the strength of weld metal (WM). Therefore, this research work aims to develop an artificial neural network (ANN) with which the welded AHSSs' mechanical properties typical in automotive engineering and their joints such as heat affected zone (HAZ) or WM can be determined locally without performing the tensile test. Therefore, it is needed in the first step to determine the material parameters which are used later to check the validity and performance of the trained ANN.

3.1. Methodology

The primary issue with welded AHSSs' mechanical behavior is how they respond to uniaxial loading situation in different zones. Therefore, the stress-strain behavior of the various zones of a welded joint should be investigated. The conventional method is uniaxial tensile test with a dog-bone sample to draw the stress-strain diagram as a representative of the elastoplastic behavior of metals. However, it is impossible to produce a conventional tensile specimen from the WM due to inhomogeneous material in the welded zones and the tiny size of the WM. It is common to use the thermomechanical simulator [14] to reproduce the microstructure of WM in a larger

area. Since such equipment and infrastructure is not available in the research institute where the current project is conducted, a novel method is proposed to determine the material parameters of WM without the need for a thermomechanical simulator.

In this methodology, it is first necessary to weld two plates with the industrial welding parameters and perform a metallographic investigation to analyze the microstructure and hardness of the WM resulting from the conventional welding parameters. Subsequently, the welding parameters were changed several times to find the optimal welding parameters to reproduce the microstructure of WM as large as possible in only one plate. Therefore, it is necessary to perform the metallographic analysis again to study the microstructure and hardness of the reproduced WM with optimal welding parameters. Then, the tensile specimens must be made from the welded plates containing different materials such as BM and WM. Since the strength of the WM produced by RSW is higher than that of the BM, it is necessary to make a notch in the WM to ensure that the fracture occurs definitely in the WM. On the other hand, the stress-strain diagrams of the notched and smooth tensile specimens are different. Therefore, it is necessary to perform a tensile test on both notched and smooth tensile specimens to find out the geometry factor and the relationship between the two diagrams. With the value of the geometry factor, it is possible to calculate the stress-strain of the welded smooth tensile specimens from the welded notched tensile specimens. However, the first step to begin with this methodology is to characterize and learn about the AHSSs used in the current research.

3.1.1. Material Characterization

Several AHSSs have been used in the current research work, which contain DP-steels such as DP600, DP800 and DP1000, and a high strength fine grained structural steel such as S690QL. The significance of these steels is their low carbon content. In DP-steels, the high amount of manganese, silicon and chromium allows shaping a two-phase microstructure with higher strength yields without decreasing ductility [21]. DP-steels are widely used in the automotive industry to manufacture the body of automobiles, and structural steels are mostly used in the constructions. The conventional welding methods used for DP steels are RSW or LBW, and for high strength fine grained structural steels are LBW or Arc welding. The investigations of

the current research are carried out on the base metal of DP600, DP800, DP1000 and S690QL and on the welded joints of DP600 and DP1000 made of RSW and WM of S690QL made of LBW.

The cold-rolled, and zinc-coated steel plates of DP600 with a thickness of 1 mm, zinc-coated steel plates of DP800 with a thickness of 1.5 mm, and the blank plates of DP1000 with a 2 mm thickness, and the blank plates of S690QL with 8 mm thickness are used. The chemical compositions of the selected steels are summarized in Table 3.1.

Table 3.1 Chemical compositions of used materials, in weight %.

Material	C	Si	Mn	Cr	Mo	Al	Fe
DP1000	0.11	0.5	2.14	0.03	0.002	0.04	balance
DP800 + ZE	0.14	0.8	1.47	0.1	0.01	0.015	balance
DP600 + ZE75/75	0.1	0.14	1.4	0.16	0.18	0.02	balance
S690QL	0.2	0.8	1.7	1.5	0.7	-	balance

The metallic sheets were prepared using metallographic techniques and the etching solution employed was a 2% Nital solution. Figure 3.1 (a) and (b), captured by light microscopy, show the two-phase microstructure of the DP600 and DP1000 steel sheets, respectively, which contains a soft matrix (ferritic phase) with islands of the martensitic phase. The soft ferrite matrix is responsible for ductility (formability), and the martensitic phase increases strength in DP steels. Figure 3.1 (c) shows the high strength fine grained structural steel S690QL, which contains two phases of bainitic and martensitic microstructure. Since in the present research only the mechanical properties of DP800 in base material are considered and it was not welded by any techniques, the metallographic investigations on DP800 were not performed.

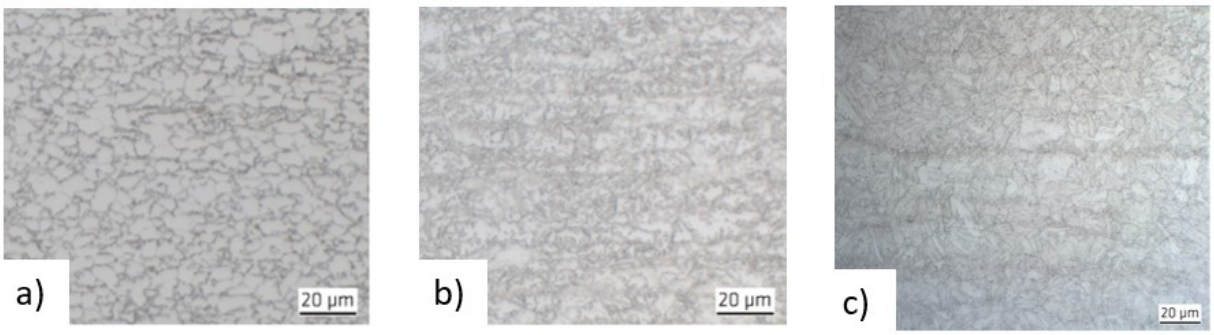

Figure 3.1 Microstructure of base metal; (a) DP600; (b) DP1000; (c) S690QL; light microscopy

3.1.2. Resistance Spot Welding

A C-type servo motor spot weld-gun was applied for RSW of steel plates with a medium-frequency (1000 Hz) direct-current transformer. The geometry of the water-cooled electrode caps provided according to what was suggested in reference [114]. The samples with dimensions of 80×30×2 mm^3 made from both DP600 and DP1000 steel plates. Then two steel sheets (similar material) of DP1000 and DP600 were welded according to the industrial welding parameters [115] as demonstrated in Table 3.2.

Table 3.2 Industrial welding parameters related to RSW of two plates based on following guideline [115]

Material	Electrode force in kN	Holding time in ms	Electric current in kA	Electrode cape
DP1000	5	140	9	F16
DP600	3.5	260	8	F16

For the fabrication of the dog bone tensile specimens, it is necessary to have a large volume of a homogeneous material such as WM or BM on hand to produce the tensile specimens. Due to the lack of infrastructure in the research institute, it was not possible to manufacture the micro tensile specimens or reproduce the microstructure of WM in a larger area with a thermomechanical simulator, so it has been tried to vary the welding parameters to find the optimal parameters that can reproduce the similar microstructure of WM in a larger area. The four parameters of electrode force, holding time during welding, electric current and electrode cap have been altered more than

100 times based on the interval given in Table 3.3 in order to find the optimal welding parameters.

Table 3.3 Variation of the welding parameters of RSW on plate (both DP600 and DP1000) to find the optimal welding parameters to reproduce the WM as large as possible in one plate

Electrode force in kN	Holding time in ms	Electric current in kA	Electrode cape
0.5 to 9	100 to 606	4.5 to 20	A-B-E-F-G

The new welding parameters should meet the following requirements so that they can be selected as optimal parameters to reproduce the microstructure of the WM in a steel plate: a) the microstructure of the weld nugget from two plates and the weld nugget from one plate must be similar; b) the surface deformation should be kept to a minimum since the plates must later be used to prepare tensile specimens; c) finally, the weld nugget should be provided with a maximum size since they must be used as tensile specimens.

In order to have a better overview about the combination of the changes in the welding parameters, the variation configuration of the RSW parameters are presented in Figures 3.2 to 3.5 and compared with the conventional industrial RSW parameters according on the guidelines [115]. RSW has been repeated with different types of electrode caps, as they have different geometries and by changing them, the level of pressure on the surface of the sample and the size of the reproduced microstructure can be drastically affected. For example, the electrode cap A16 has a flat surface tip and, as expected, leads to less deformation at the surface of the welded specimens compared to the specimens welded with the electrode cap of F16, since the latter has a rounder geometry at its surface tip compared to A16. Another important parameter is the holding time in the RSW process, and expected that with its increase the size of the WM grows too. Therefore, RSW has been started with a holding time of about 100 ms and raised to more than 600 ms, which corresponds to the maximum capacity of the used infrastructure. Subsequently, RSW was continued with a holding time of 600 ms and other parameters such as electrode force and electric current were changed to find the optimal welding parameters under the condition that no splash is visible, by repeating the welding process twice for each parameter combination.

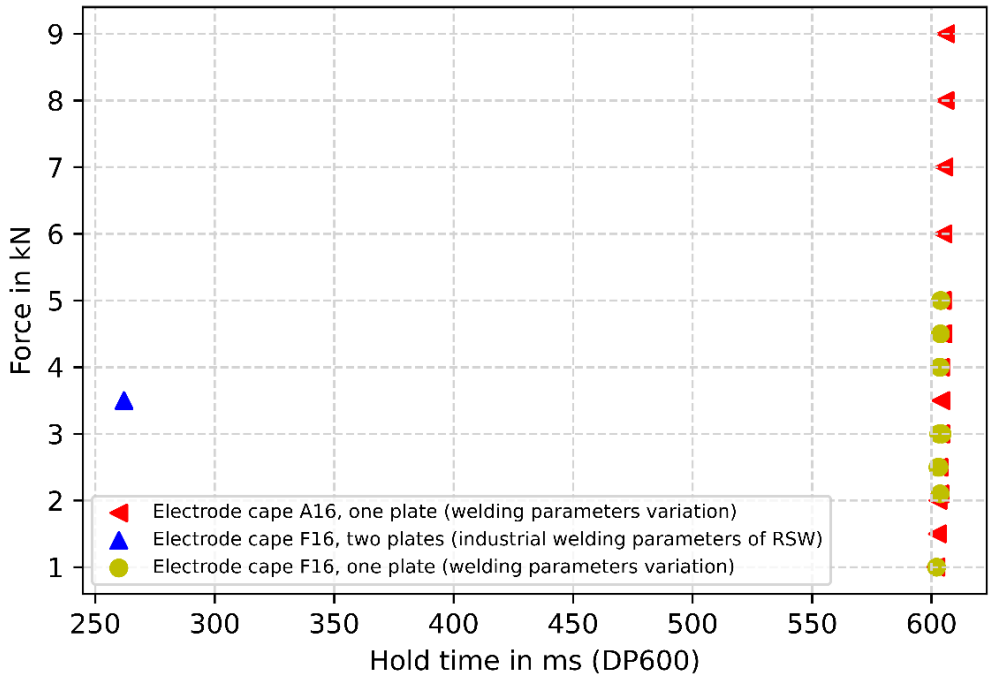

Figure 3.2 Variation configuration of the electrode force, holding time and electrode cape as the welding parameters of RSW for DP600 in order to find the optimal welding parameters to reproduce the WM as large as possible in one plate and comparison with the industrial [115] welding parameters

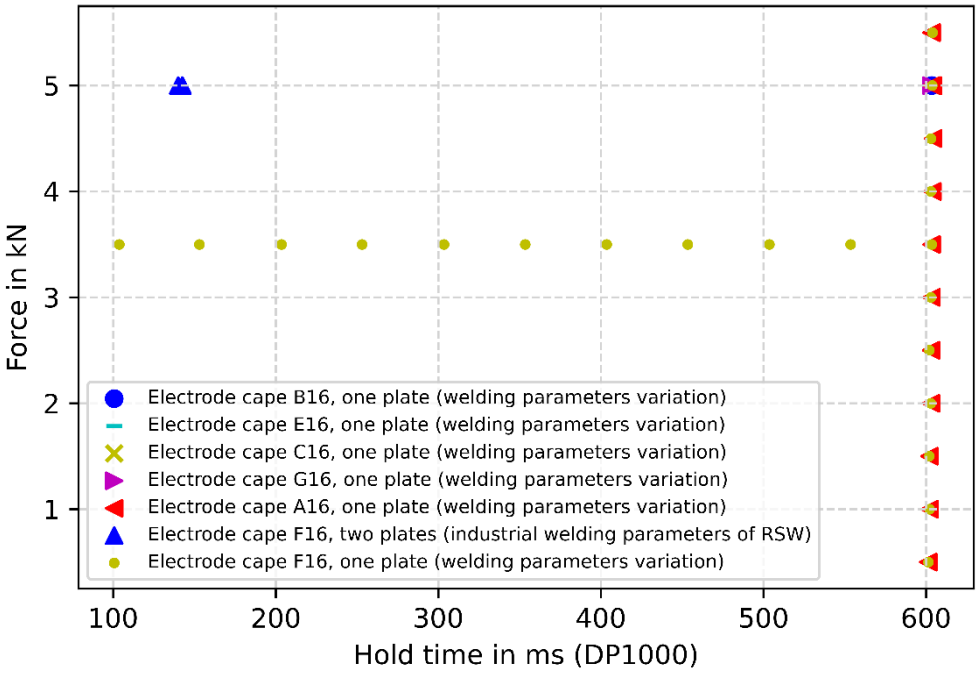

Figure 3.3 Variation configuration of the electrode force, holding time and electrode cape as the welding parameters of RSW for DP1000 in order to find the optimal welding parameters to reproduce the WM as large as possible in one plate and comparison with the industrial [115] welding parameters

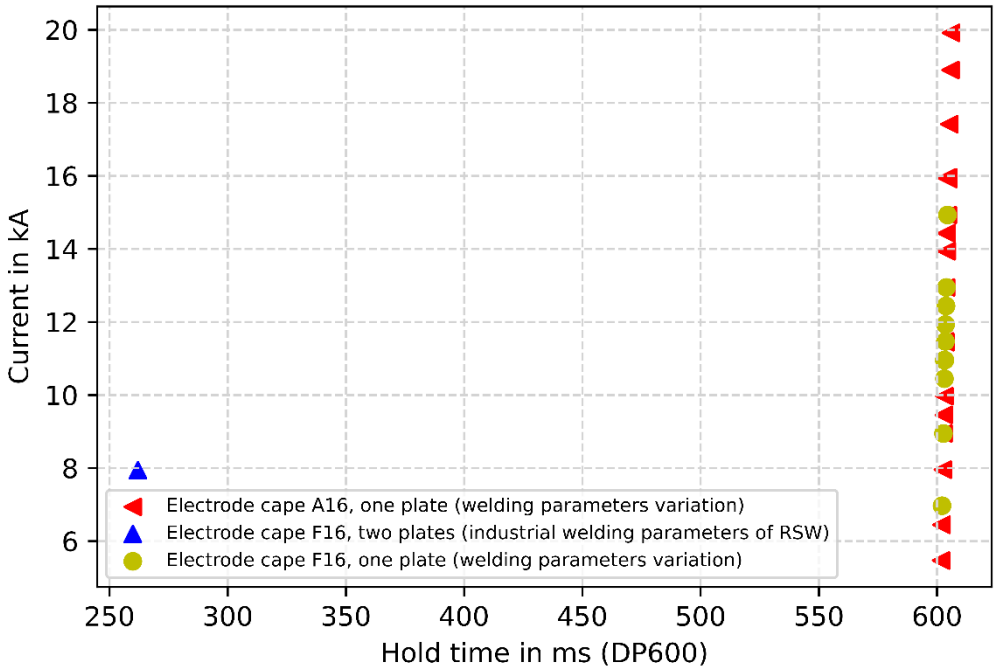

Figure 3.4 Variation configuration of the electrical current, holding time and electrode cape as the welding parameters of RSW for DP600 in order to find the optimal welding parameters to reproduce the WM as large as possible in one plate and comparison with the industrial [115] welding parameters

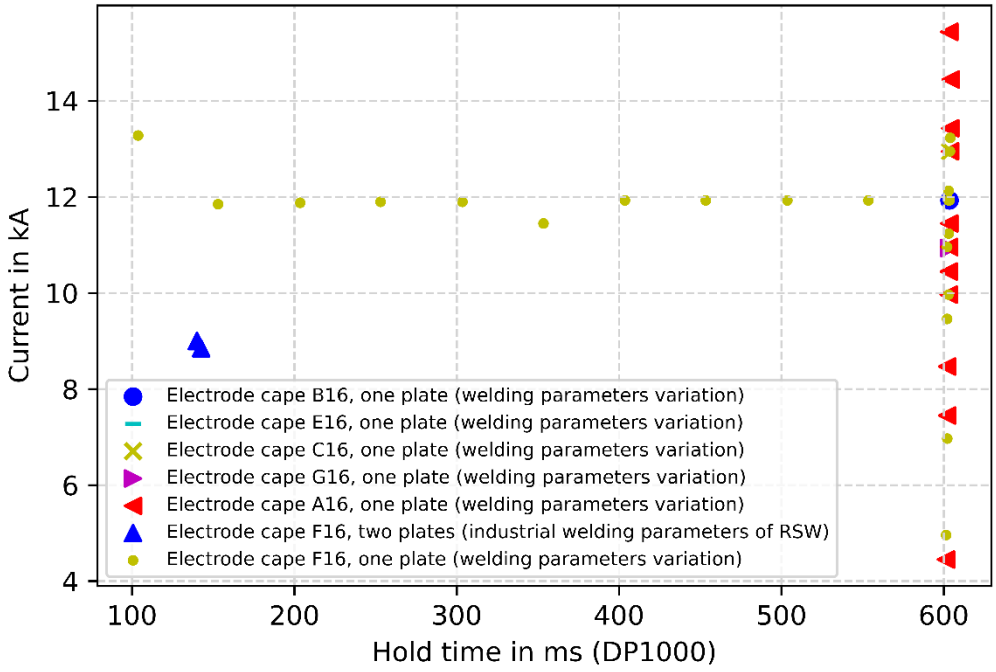

Figure 3.5 Variation configuration of the electrical current, holding time and electrode cape as the welding parameters of RSW for DP1000 to find the optimal welding parameters to reproduce the WM as large as possible in one plate and comparison with the industrial [115] welding parameters

The investigation shows that there is a direct relationship between the magnitude of the electrode force, the electric current and the size of the reproduced WM when the RSW is applied to only one plate. When the magnitude of the electric current is increased, the value of the electrode force must also be increased and the size of the WM grows as a consequence. However, a high value of electrode force leads to the formation of small cracks on the surface of the specimens, as shown in Figure 3.6, which should not be present in tensile specimens. Therefore, there should be a compromise between the desired size of reproduced WM and the magnitude of the electric current and electrode force.

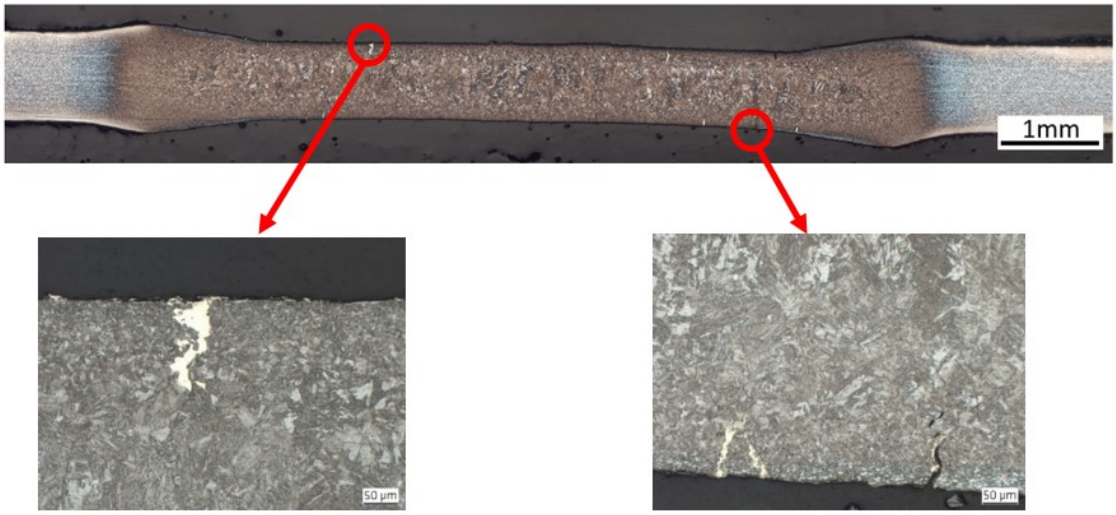

Figure 3.6 Formation of microcracks on the surface of DP600 specimen after increasing the electrode force to 8 kN, electric current to 19 kA and holding time to 600 ms by using the electrode cape of A16

Considering all the above requirements and restrictions, the parameters shown in Table 3.4 are chosen as the optimal RSW parameters to reproduce the microstructure of WM in one plate as large as possible. In Section 3.2.1, called "Metallographic Analysis", the microstructure of the reproduced WM with the following parameters is investigated and compared in details with the microstructure of the RSW based on the industrial welding parameters.

Table 3.4 The optimal welding parameters to reproduce the WM of RSW on one plate

Material	Electrode force in kN	Hold time in ms	Electric current in kA	Electrode cape
DP600	5	600	16	A16
DP1000	5	600	13.5	A16

3.1.3. Laser Beam Welding

In the current research work, LBW was performed using a TruDisk 16002 Yb:YAG disk laser, which is a solid-state laser source and has a maximum power of 16 kW with a wavelength of 1030 nm. The AHSSs of DP600, DP1000 and S690QL were welded by LBW technique to investigate their microstructure and material properties. Figure 3.7 shows the experimental setup and the position of the DP600 steel during LBW.

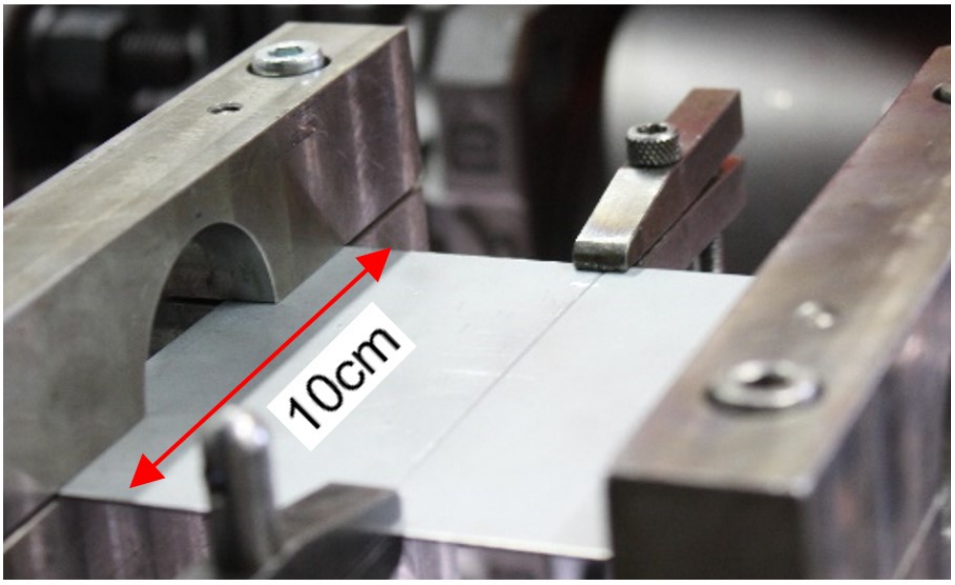

Figure 3.7 Experimental setup and position of DP600 steel during LBW with TruDisk 16002 Yb:YAG disk laser

At the beginning, two plates of DP600 and DP1000 were positioned alongside each other as shown in Figure 3.7. Then, the parameters of LBW such as welding velocity and defocusing are kept constant at 1.8 m/min and 0 mm, respectively. The power of the laser beam was slightly increased to find out the proper laser power which is able to weld thoroughly two steel sheets made of DP600 and DP1000. The steel sheets placed next to each other are made of the same material. The same procedure is followed again for the S690QL, except that the welding velocity remains constant at the level of 2 m/min. The above processes lead to the parameters of LBW as shown in Table 3.5.

Table 3.5 Welding parameters of LBW on AHSSs

Material	Power in Kw	Defocusing in mm	Velocity in m/min
DP600	1.6	0	1.8
DP1000	2.4	0	1.8
S690QL	8	0	2

In the next steps, more than 84 plates of DP600 and DP1000 were blind welded by varying the parameters of LBW in an interval as given in Table 3.6. The objective is to find the optimal welding parameters that result in the largest possible WM with similar microstructure to the WM obtained from the parameters in Table 3.5. In addition to the similarity of the microstructure, it is important to know that the deformation due to LBW on the plates and the deformation on the surface of the specimens must be kept to a minimum, since the tensile specimens must be produced later from the welded plates.

The welding velocity again remains constant at 1.8 m/min and the defocus and laser power were changed proportionally to each other to induce more energy during welding. It has been shown that increasing the laser power and defocus results in a larger and wider weld nugget, however, the desired microstructure cannot be reproduced. In Section 3.2.1, "Metallographic Analysis", the microstructure of the reproduced WM with parameters from Table 3.6 is investigated and compared in details with the microstructure of the LBW based on the welding parameters from Table 3.5.

Table 3.6 Variation of welding parameters of LBW to find the optimal welding parameters

Power in kW	Defocusing in mm	Velocity in m/min
1 to 16	-100 to 0	1.8

3.1.4. Tensile Test

The objective of performing the quasi-static tensile test is to determine the mechanical properties of the used AHSSs and their WMs in order to later check the accuracy and performance of the trained ANNs. The conventional test can be conducted on the specimens made of the base material of the AHSSs. However, the challenge is to determine the stress-strain diagram of the WMs, since its size is not large enough to produce a homogeneous tensile specimen from them. Therefore, a novel

methodology is introduced in this research work to identify the material data of the WM from the welded notched tensile specimens. In such a methodology, the following steps must be taken:

- Preparation of smooth tensile specimens from BM of used AHSSs
- Preparation of the notched tensile specimens from the welded and not welded plates of used AHSSs
- Comparison of the stress-strain diagrams of the notched and smooth tensile specimens of BM to determine the geometry factor
- Calculation of the stress-strain diagram of the WM by using the geometry factor and the stress-strain diagram of the notched welded tensile specimens
- Review the methodology by numerically simulating the tensile specimens and comparing the results with the results of the experiments
- Validate the determined material parameters by comparing them with available data from the literature

Therefore, in the first step, it is necessary to explain the geometry of the tensile specimens and the experimental setups for performing the tensile test on notched specimens.

3.1.4.1. Experimental Analysis

The tensile specimens were made from BM of AHSSs as shown in Figure 3.8 to determine the mechanical properties of BM. The geometry of the tensile specimens of DP600 with a thickness of 1 mm, DP800 with a thickness of 1.5 mm, DP1000 with a thickness of 2 mm, and S690QL with a thickness of 8 mm are shown in Figure 3.8 from (a) to (d), respectively. The geometry of the specimens is determined according to the guidelines [50]. The specimens were first cut using the waterjet cutting technique and then the edges were milled to produce a homogeneous specimen with accurate geometry and no microcracks.

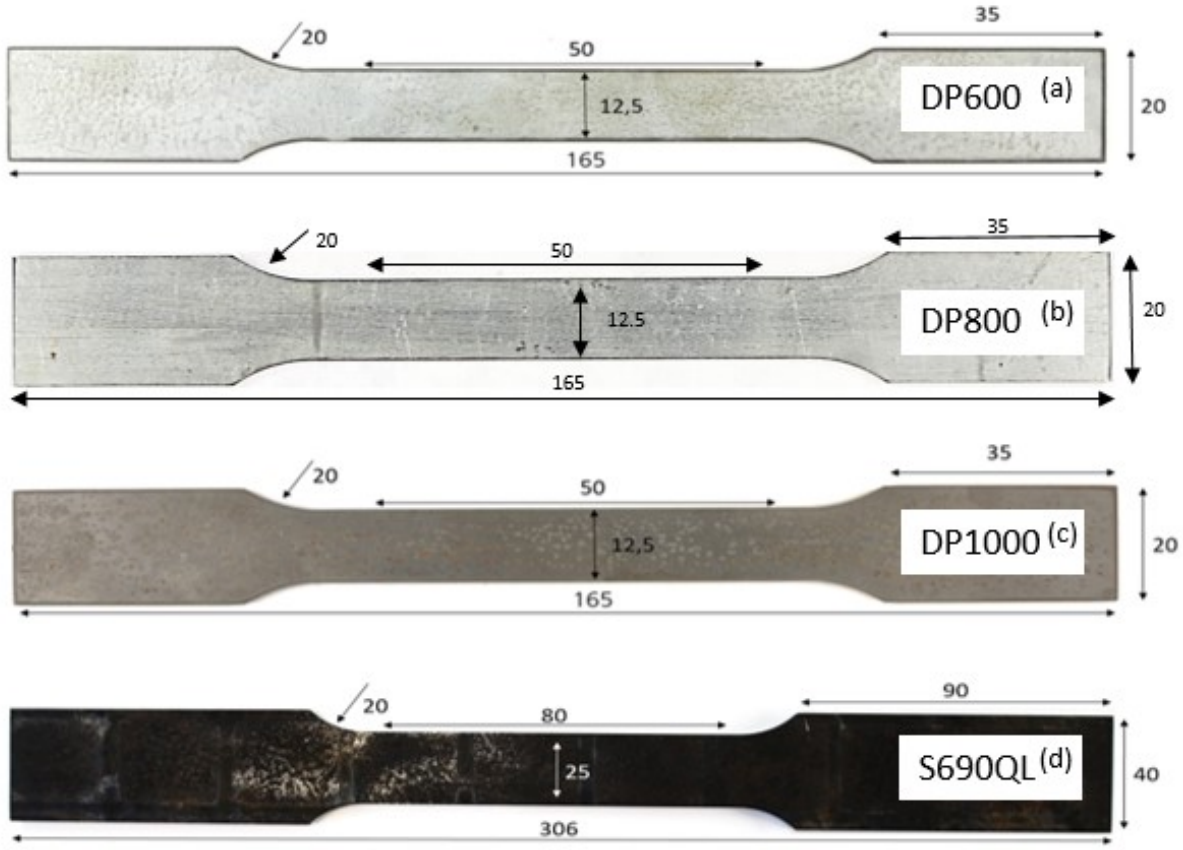

Figure 3.8 Geometry of tensile specimens prepared for tensile test according to guideline [50]; (a) DP600 with thickness of 1mm; (b) DP800 with thickness of 1.5mm; (c) DP1000 with thickness of 2mm; (d) S690QL with thickness of 8mm

Besides, it is essential to quantify the mechanical properties of WM to validate the trained ANN with their material data, since the yield strength of WM resulting from RSW is higher than the corresponding BM, therefore, the trained ANN can be tested in the upper range of the training interval. The tensile specimens made from the welded steel sheets must contain a notch in the area where the WM is located. The reason for such a geometry is that the yield strength of WM is higher than that of BM and the notch or the reduced geometry forces the fracture to occur exactly in WM, thereby enabling the determination of the material behavior of WM. However, the geometry of the welded notched tensile specimens are depended on the size of the WM. It is mentioned in the literature that the WM length should be considered larger than the distance between notches to minimize the impact of inhomogeneity caused by the welding process. Furthermore, the distance between notches should be also greater than or equal the notch radius to decrease the impact of strain hardening on the concentration stress coefficient caused due to notched geometry [63]. The

mentioned criteria were followed during the preparation of the welded notched tensile specimens.

The mechanical behavior of metals in a tensile test is affected by stresses and strains experienced in the specimen. However, the presence of notches and cracks affect deformations in fracture mechanics. A notch, or any other stress concentration regions will experience higher applied stress than other unaffected zones. Technically, the mechanical properties of a metal with a smooth sample is different from a notched sample. The tensile yield strength of steels in a notched sample are recorded greater than those smooth samples in a uniaxial tensile test. The maximum amount of stress ahead of the notch is a function of the notch's geometry on the specimen [116]. Therefore, it is necessary to perform the tensile test on both smooth and notched tensile specimens of BM to compare them with each other and determine the influence of the notch on the stress-strain diagram and quantify it in terms of geometry factor. With the value of the geometry factor, it is possible to calculate the stress-strain diagram of the smooth specimens as a reference value from the notched specimens [63].

Figure 3.9 shows the geometry of the tensile specimens prepared to determine the mechanical properties of the WM resulting from RSW. The notch geometry depends on the size of the WM produced on a single plate of DP600. In Section 3.2.1, "Metallographic Analysis", the microstructure and size of the reproduced WM with the optimized and varied welding parameters are studied in details. Figure 3.9 (a) and (b) shows the geometry of the smooth and notched tensile specimens from BM, respectively. The quasi-static tensile test is performed on both specimens to calculate the geometry factor. Figure 3.9 (c) shows the geometry of the welded notched tensile specimens from DP600. The notch is accurately positioned on WM to force the fracture in WM to obtain the total stress-strain curve of WM. Since the yield strength of DP600 in BM is extremely lower than the yield strength of DP600 in WM, it is therefore possible that the fracture occurs outside of the notch and in BM. Consequently, additional notched tensile specimens, as shown in Figure 3.9 (d) and (e), are prepared with a larger notch radius of BM and WM, respectively, to ensure that the fracture takes place in the WM.

The final dimensions of the tensile specimens of DP600, Figure 3.9 from (a) to (e), were cut from the plates using a waterjet cutting machine. Then, the edges of the cut

specimens were finished by milling to produce the specimens as accurately as possible. Finally, the specimens were ground on the top and bottom surfaces to remove the heat-affected zones and the deformations on the specimen surface caused by the electrode force. Therefore, the final thickness of the DP600 tensile specimens was reduced from 1 mm to 0.4 mm. Next, the specimens were sandblasted at the clamping section to increases the surface roughness locally and consequently prevents slippage during clamping.

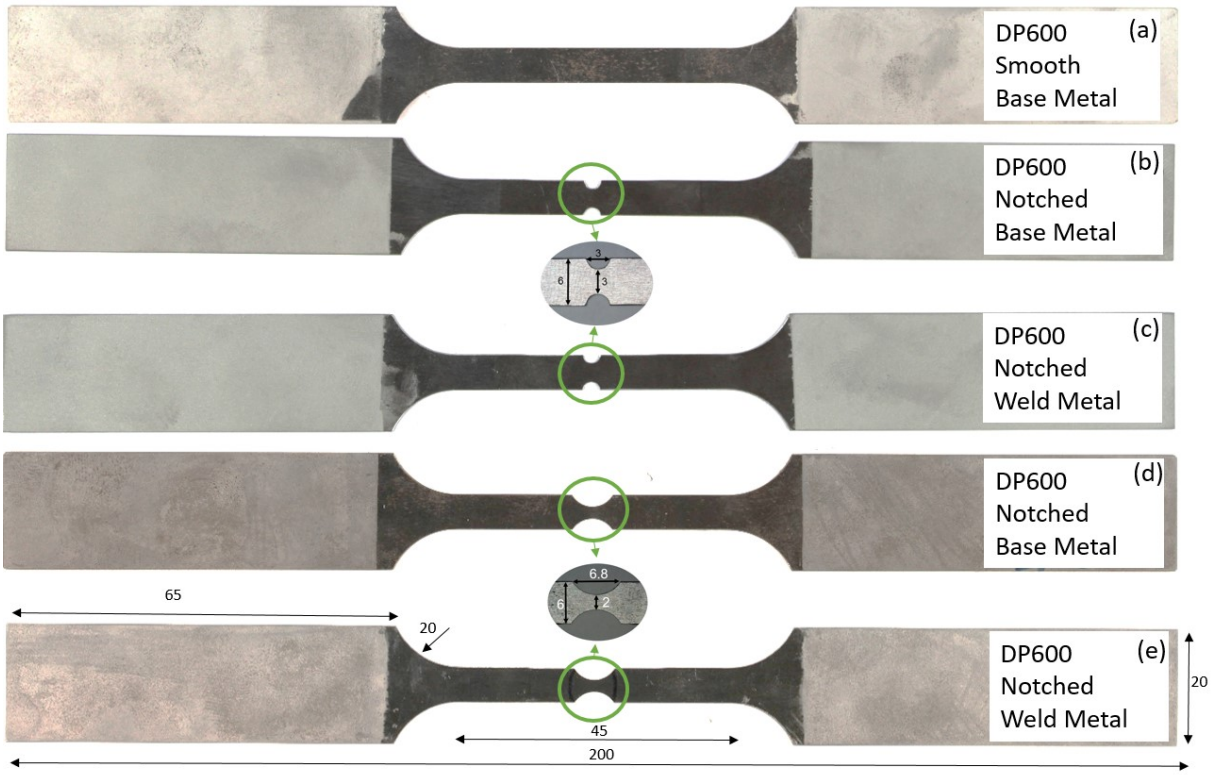

Figure 3.9 Geometry of tensile specimens prepared for tensile test; (a) DP600 with thickness of 0.4 mm, smooth sample made of BM; (b) DP600 with thickness of 0.4 mm, distance between notches of 3 mm and made of BM; (c) DP600 with thickness of 0.4 mm, distance between notches of 3 mm and WM in notched area; (d) DP600 with thickness of 0.4 mm, distance between notches of 2 mm and made of BM; (e) DP600 with thickness of 0.4 mm, distance between notches of 2 mm and WM in notched area

In the same way, Figure 3.10 shows the geometry of the tensile specimens prepared to determine the mechanical properties of the WM resulting from RSW of DP1000. Figure 3.10 (a) and (b) show the geometry of the smooth and notched tensile specimens from BM, accordingly. Figure 3.10 (c) presents the geometry of the welded notched tensile specimens from DP1000. As the yield strength of DP1000 in BM is higher than the yield strength of DP600 in BM, it is not necessary to prepare more tensile specimens with larger notch radius. The final dimensions of the tensile

specimens of DP1000, Figure 3.10 from (a) to (c), were first cut from the plates using a waterjet cutting machine and then machined by milling. Finally, the specimens were ground on the top and bottom surfaces, and the final thickness of the DP1000 tensile specimens was reduced from 2 mm to 0.9 mm. The specimens were then sandblasted at the clamping area to prevent slippage during tensile test.

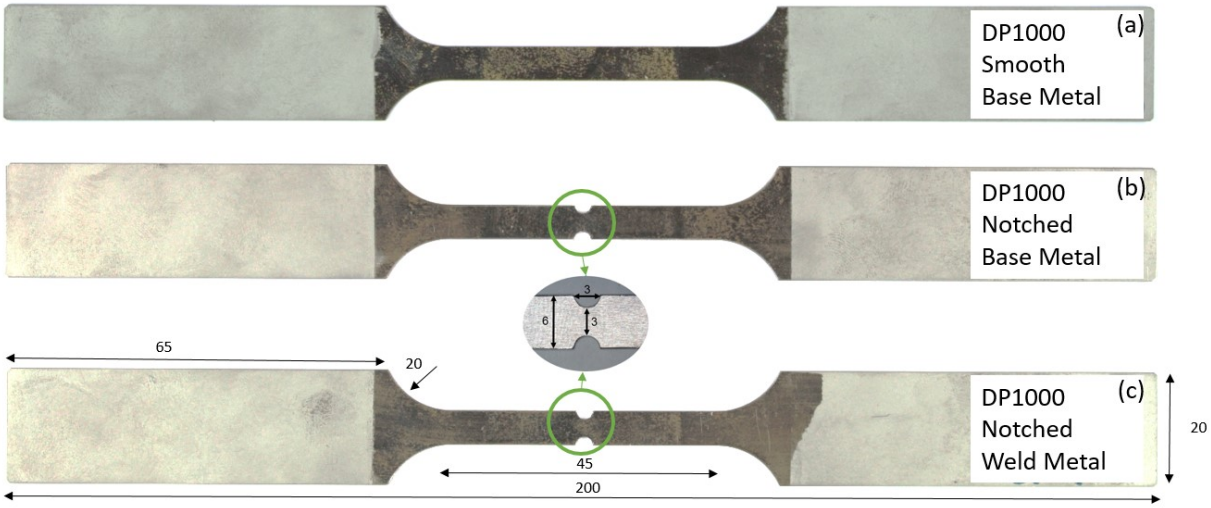

Figure 3.10 Geometry of tensile specimens prepared for tensile test; (a) DP1000 with thickness of 0.9 mm, smooth sample made of BM; (b) DP1000 with thickness of 0.9 mm, notched sample made of BM; (c) DP1000 with thickness of 0.9 mm, notched sample with WM in notched area

The strain controlled tensile test was performed on the smooth tensile specimens made of DP600, DP800, DP1000 and S690QL steel sheets with a strain rate of 10^{-3} s^{-1}. The strain was measured globally at a extensometer length of 50 mm. Next, the tensile test was performed on notched tensile specimens with the strain rate of 4×10^{-5} s^{-1}. The strain was measured locally and optically on place where the fracture occurs with a virtual extensometer length of 1 mm using a commercial 3D-digital image correlation (DIC) system GOM Aramis 4m as shown in Figure 3.11. Aramis, as a contactless strain measurement system, operates at scales from one micrometer to meters, depending on whether two states of a specimen are being compared. The position of pixel subsets based on contrast in the original images can be compared with images of the deformed samples to calculate the strain profile. By coloring the samples with white paint and then spraying a black paint on the surface of the sample, the stochastic patterns can be generated. Furthermore, the strain rate must be adjusted according to the length of the reduced zone of the notched tensile specimen. Since the length of the reduced region is smaller than that of the smooth tensile

specimens for the notched specimens, the quasi-static tensile test must be performed with a much smaller strain rate on notched specimens compared to that required for smooth samples to guarantee a quasi-static tensile test.

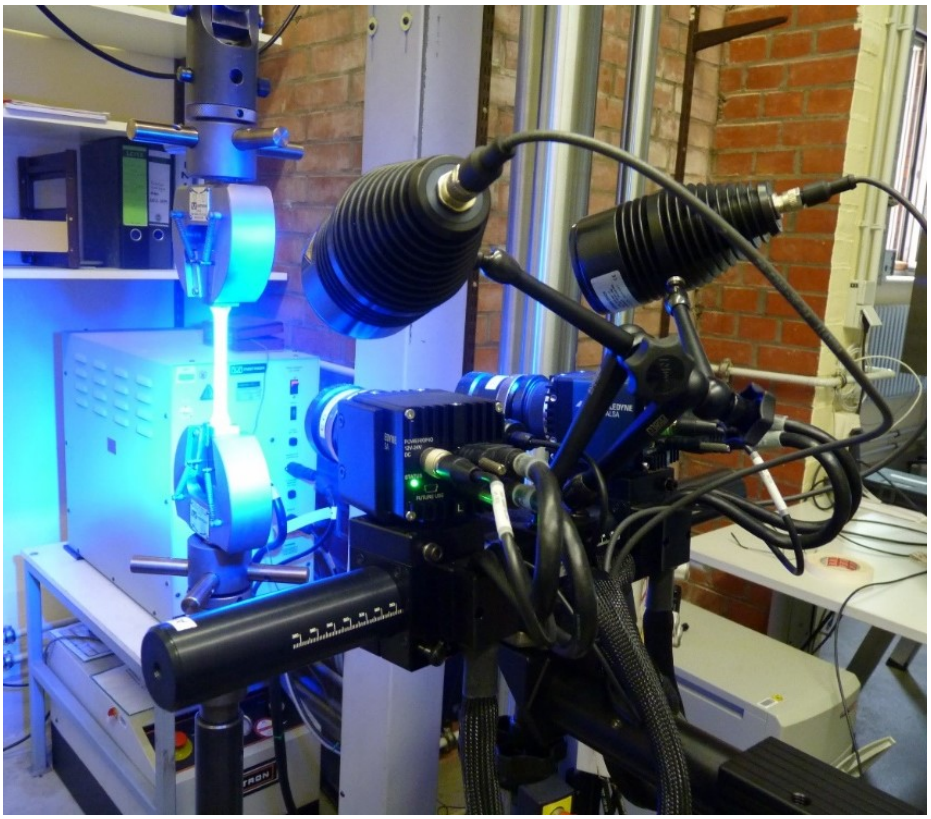

Figure 3.11 performing of quasi-static tensile test and measuring of strain optically with a commercial 3D Digital Image Correlation (DIC) system of GOM Aramis 4m

3.1.4.2. Numerical Approach

The smooth and notched tensile specimens of DP600 and DP1000 were numerically simulated based on the geometry of Figures 3.9 and 3.10. Figure 3.12 (a) and (b) presents the simulation models of the notched tensile specimens of DP1000 and DP600, respectively. The specimens were fixed on the bottom side, and a load was continuously applied to the sample's upper side. A two-dimensional simulation was carried out with four-node plane elements. A mesh size of 0.05 mm in the notch and 1 mm in the remaining tensile specimen was used. To calculate the local strain in the welded area, the displacement of four points in the notch was investigated, as schematically shown in Figure 3.12 (a). Calculating the distance between point 1 and point 2 results in the specimen's changing cross-section during the tensile test which is needed to determine the true stress. With the displacement of points 3 and 4, the

specimen's strain can be investigated locally in the notched area. This corresponds to the operating principle of virtual extensometers for evaluating tensile tests with the DIC system and determining of the true strain. As a result, the true stress-strain curves can be determined with the actual cross-sections, true strains, and applied loads.

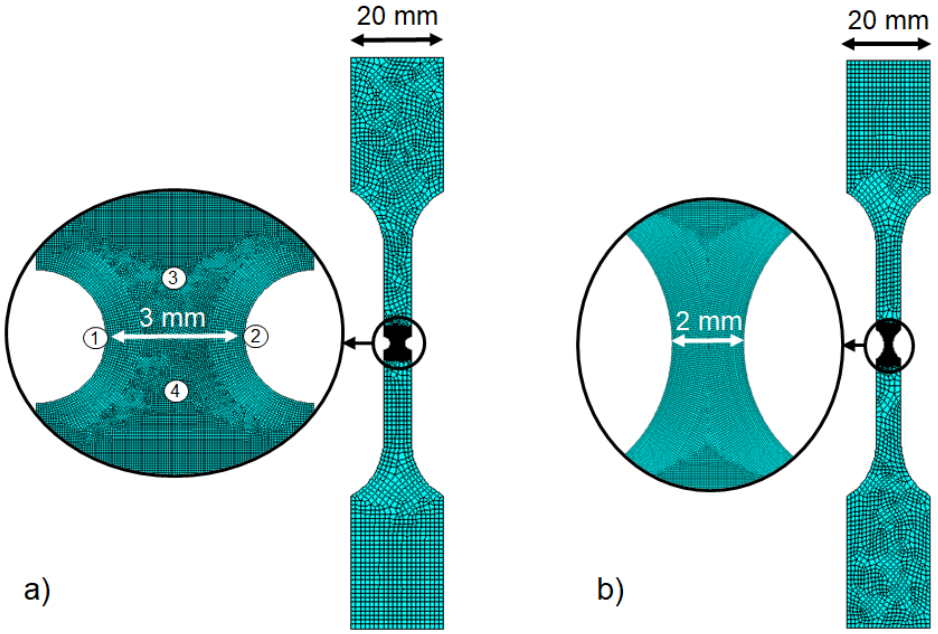

Figure 3.12 Numerical Simulation model of the notched specimens; (a) notched geometry of DP1000; (b) notched geometry of DP600 with larger notch radius

The material parameters of a nonlinear isotropic strain hardening material model as shown in Figure 2.2 and Equation (2.1) for the smooth sample of DP1000 BM can be determined by inverse simulation. This is done by simulating the tensile tests with varying material parameters randomly until a minimum mean squared error between the simulation and experimental results has been reached. With this approach, the material parameters for the DP1000 BM are obtained. Subsequently, the notched specimen with the notch geometry shown in Figure 3.12 (a) was simulated with the same material model parameters of DP1000 BM to only investigate the influence of this notch geometry on the stress-strain behavior of BM. The geometry factor for DP1000 was calculated by comparing both of the aforementioned stress-strain curves. Similarly, the material parameters for welded (RSW) and notched DP1000 can be determined by using the experimental data from the tensile tests and inverse simulation, as described above. Those material model parameters for welded and notched specimens of DP1000 are then multiplied by the geometric factors to

calculate the material parameters for smooth and welded specimens from DP1000. Finally, the notched and welded specimen is simulated with the calculated model parameters for smooth and welded specimens and compared with the tensile tests' results to validate the simulation result.

The same procedure is used to calculate the material parameters of DP600. However, a modified notch geometry with larger notch radius, as shown in Figure 3.9 (d) and (e), must be used since the tensile tests on the notched specimens with small notch geometry have shown that fracture occurs outside the notched and welded (RSW) region of the DP600 specimen. Consequently, new geometry factors for DP600 must be determined using the same approach as explained above. In the same way, the material model parameters for welded and notched DP600 are calculated by inverse simulation and multiplied by the geometry factor of the modified notch geometry to determine the material model parameters for smooth and welded DP600. Then, the tensile test for the notched specimen is simulated with the material model parameters of the smooth and welded specimens and compared with the experimental results to validate the simulation model of DP600.

3.2. Results and Discussion

In this section, the results of each step in the experimental and numerical analysis performed to determine the mechanical properties of BM and WM of AHSSs are presented and discussed in details. First of all, the macrostructure and microstructure of the welded AHSSs from RSW and LBW are shown and described. Then, the results of the tensile test on the smooth and notched tensile specimens from both BM and WM are presented and compared with each other to determine the material data of BM and WM. Finally, the presented methodology is validated with the numerical simulation result and checked against the available literature data.

3.2.1. Metallographic Analysis

The aim of performing the metallographic analysis is to study the microstructure of the reproduced WM resulting from the varied and optimal welding parameters. It is necessary to verify that both WMs obtained from welding of the plates with industrial and optimal welding parameters have the similar microstructure. The first step is to

compare the images taken from the microstructure of the WMs using the light microscope with similar scale. Then, the hardness measurement must be performed on different scales to analyze in details the different zones of the welded joints.

Figures 3.13 and 3.14 compare the microstructure of DP600 and DP1000 in different zones with each other. Figures 3.13 and 3.14 from (a) to (d) show the microstructure of BM, WM resulting from RSW on two plates with the industrial welding parameters as shown in Table 3.2, WM resulting from RSW on one plate with optimal welding parameters as shown in Table 3.4, and WM made from LBW with the welding parameters as shown in Table 3.5. It can be seen that a mixture of ferrite and martensite microstructure in BM of both DP600 and DP1000 is completely transformed into columnar martensite grains after welding with different techniques.

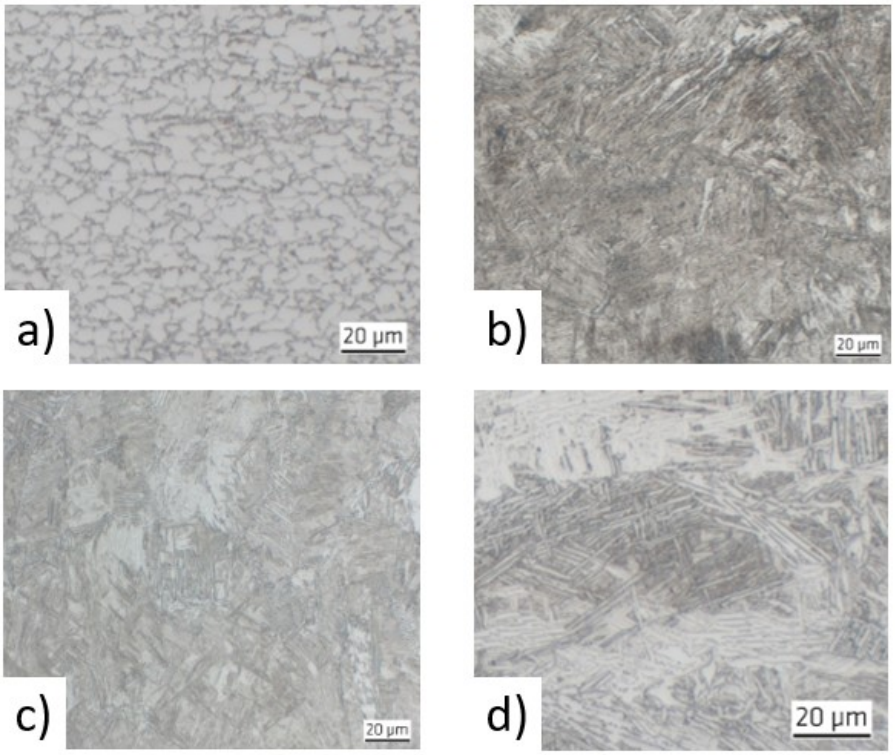

Figure 3.13 Microstructure of DP600: (a) base metal; (b) WM of RSW of two plates; (c) reproduced WM of RSW of one plate; (d) WM of LBW.

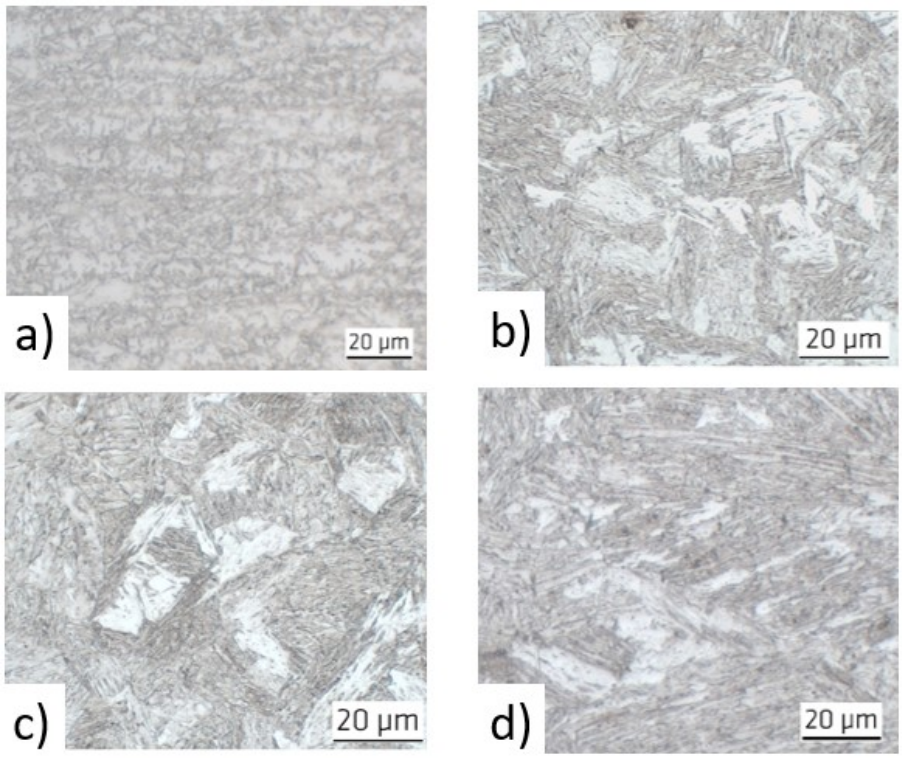

Figure 3.14 Microstructure of DP1000: (a) base metal; (b) WM of RSW of two plates; (c) reproduced WM of RSW of one plate; (d) WM of LBW.

Figure 3.15 compares the microstructure of BM of high strength fine grained structural steel S690QL with WM from LBW with parameters from Table 3.5. It can be seen that the two phases of bainitic and martensitic microstructure of BM are fully converted to martensitic microstructure.

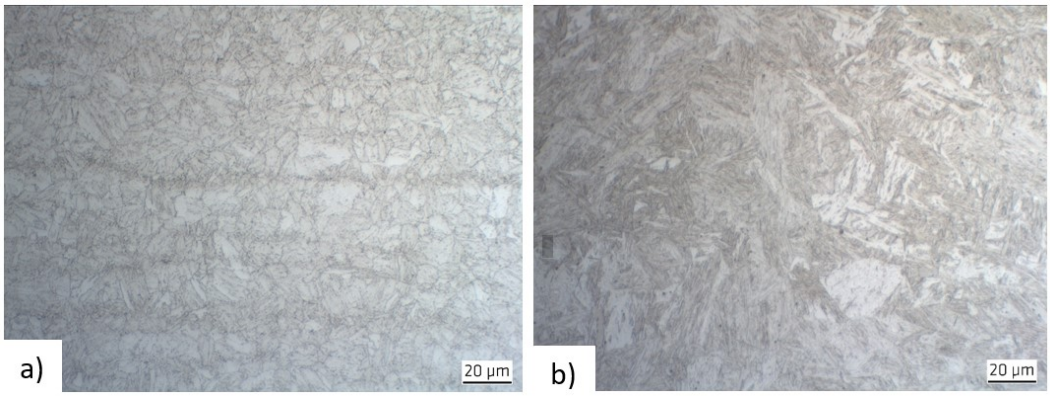

Figure 3.15 Microstructure of S690QL: (a) base metal; (b) WM of LBW

Investigations have shown that the martensitic microstructure is formed in the WM of DP-steels, when the cooling time of $t_{8/5}$ (i.e., the time it takes for the WM or HAZ to cool from 800 °C to 500 °C) is less than three seconds. However, the weld metal's cooling rate in RSW method is expected to be around 400 K/s [117]. After

conventional RSW and under experiencing such a high cooling rate, the ferrite and martensite microstructure of the DP-steels used in the present work is wholly transformed into a martensite microstructure with the hardness value exceeding 350 HV1.

As a result, the heating and cooling curves of HAZ during the RSW and LBW on DP1000 specimens with welding parameters of Tables 3.4 and 3.5, respectively, must be recorded and compared with each other to make a statement about the microstructure of welded joints. For this purpose, the temperature curve for each welding process was measured using four thermocouples (type K) which were installed on the surface of each specimen close enough to WM but in HAZ. The heating and cooling curves for each thermocouple were determined and are summarized in Figure 3.16 (LBW) and Figure 3.17 (RSW). During welding, two thermocouples on the surface of each specimen were completely burned and therefore could not provide any information. Consequently, only the heating and cooling curves of two thermocouples are shown in each diagram.

Both Figures 3.16 and 3.17 show that the cooling time from about 800 °C to 500 °C is at most less than 0.5 s, depending on the welding technique and the position of the thermocouples. For example, thermocouples 1 and 2 are located 3 and 4 mm, respectively, away from the centerline of the WM resulting from the RSW. According to Time Temperature Transformation (TTT) diagrams of DP-steels [99], such a high cooling rate can lead to a similar microstructure of martensite after welding and indicates a hardness value of more than 350 HV1. This can be confirmed later by performing of hardness measurements on WM of DP-steels.

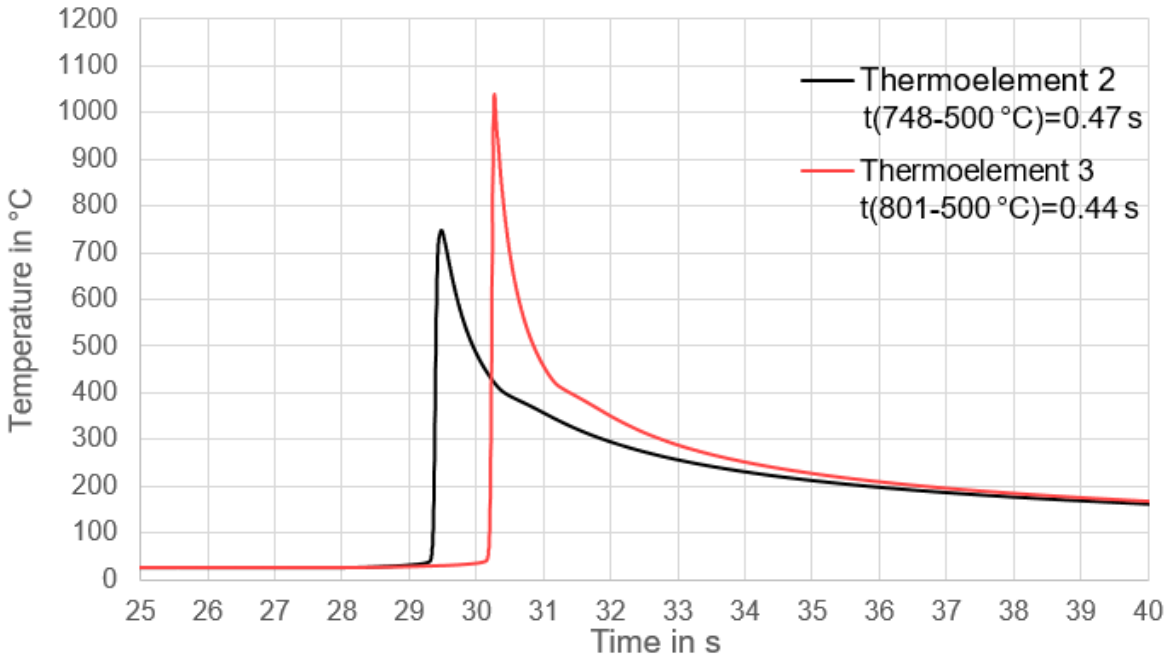

Figure 3.16 Heating and cooling curves in the HAZ of LBW of DP1000, four thermocouples (thermoelements) were installed but the information were received from two of them

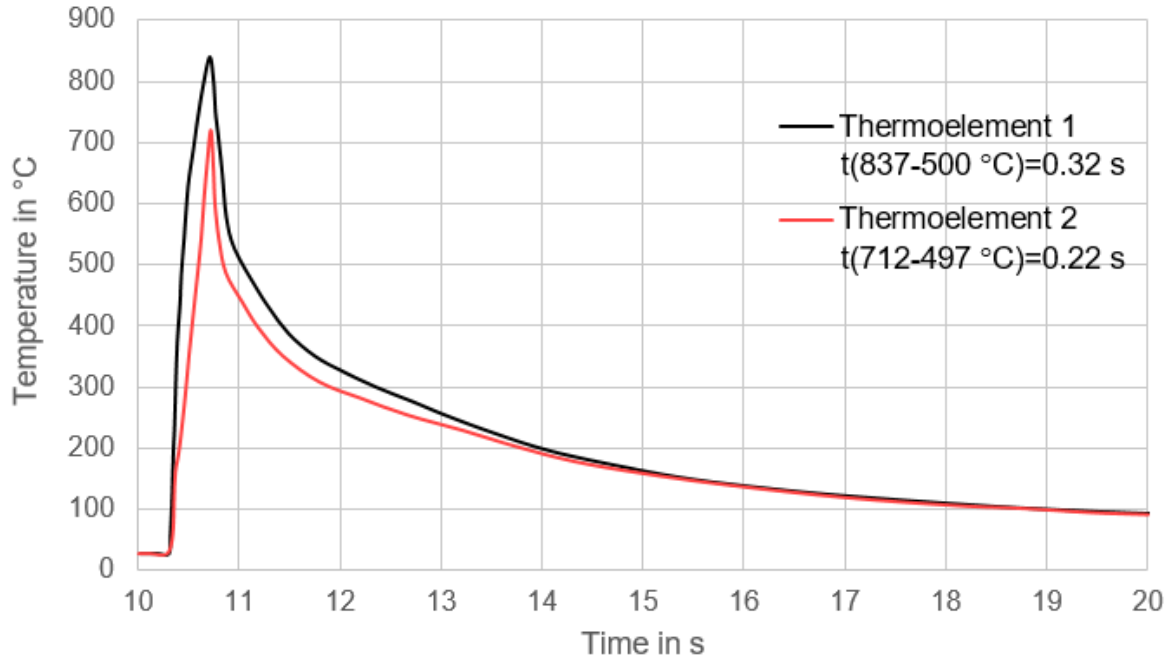

Figure 3.17 Heating and cooling curves in the HAZ of RSW on one plate of DP1000, four thermocouples (thermoelements) were installed but the information were received from two of them

The macrostructure of the welded joints of RSW and LBW of DP600 and DP1000 are shown in Figures 3.18 and 3.19 to gain a better overview of the size of the WM and HAZ. The metallographic investigation from steel plates of DP600 and DP1000 as seen in Figures 3.18 and 3.19, respectively, show that the weld nugget diameter for

the plates with industrial welding parameters (Table 3.1) is larger than the minimum nugget diameter of $4\sqrt{t}$ [115]. In this equation, "t" is the plate thickness and is equal to 2 mm and 1 mm for DP1000 and DP600, respectively. Furthermore, the weld nugget diameter became around 10% and 22% bigger after welding the DP600 and DP1000 steel sheets, respectively, with the new welding parameters (Table 3.5) compared with the industrial welding parameters (Table 3.1) . Although the applied electrode force is approximately similar in both optimum and industrial welding parameters, the surface deformation after the welding of one plate is reduced compared to the surface deformation resulted from welding of two plates due to the changing of electrode cap from F16 to A16.

Therefore, the new welding parameter sets lead to the bigger weld nugget size, smaller surface deformation, and similar microstructure. This makes it possible to produce the notched welded tensile specimens from the steel plates that are welded with the optimal welding parameters. However, it is necessary to perform a hardness measurement to obtain more information about the size and microstructure of the different zones in the welded joints.

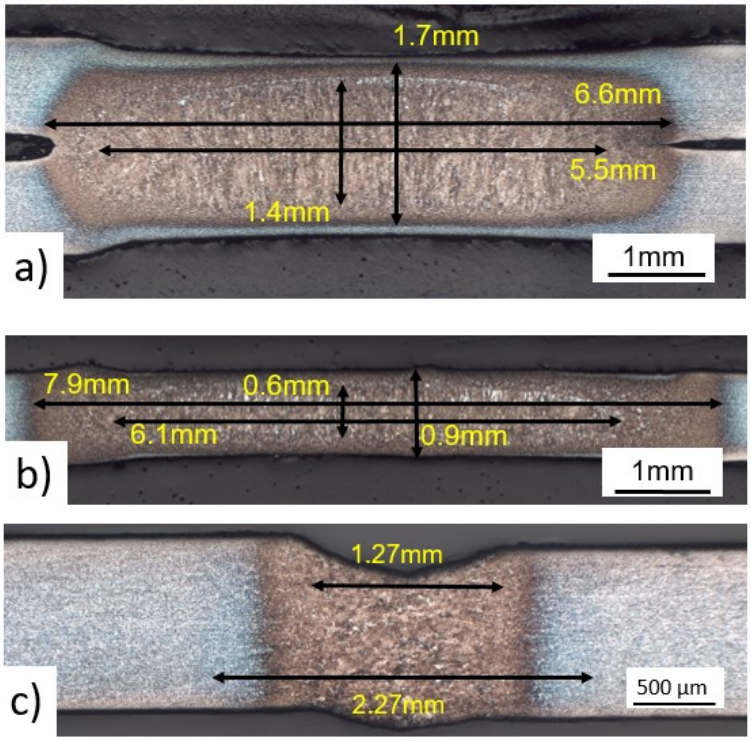

Figure 3.18 Macrostructure of welded joint of DP600: (a) RSW of two plates; (b) reproduced WM of RSW of one plate; (c) LBW.

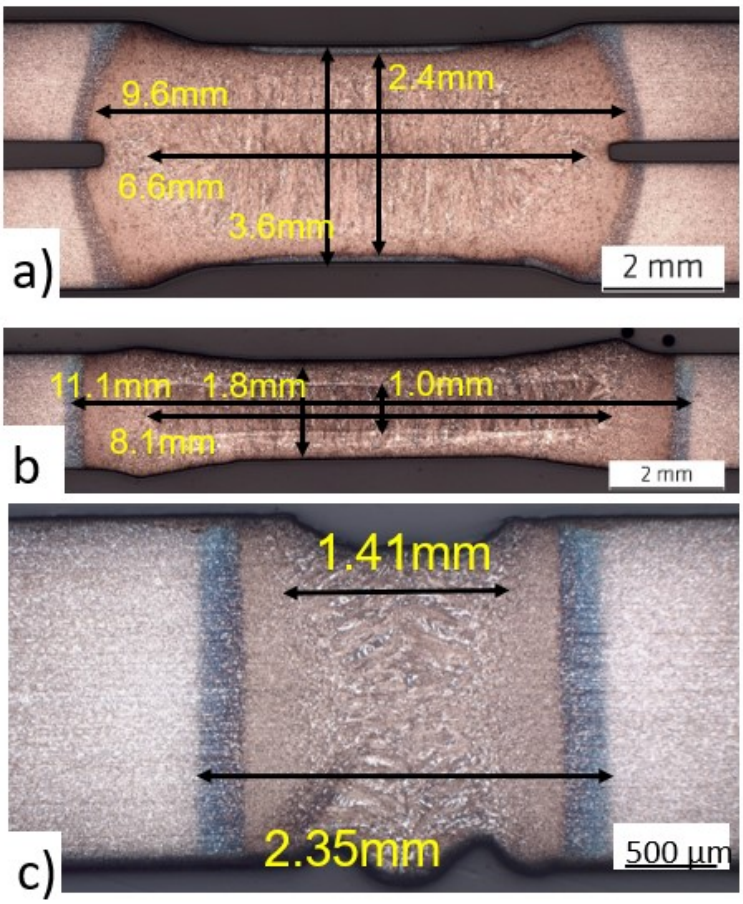

Figure 3.19 Macrostructure of welded joint of DP1000: (a) RSW of two plates; (b) reproduced WM of RSW of one plate; (c) LBW

Vickers hardness test in scale of HV0.1 for both welding methods and DP-steels completed according to [119]. Figures 3.20 and 3.21 show the mapping of hardness value (HV0.1) for DP600 and DP1000. Each indentation was automatically performed on the samples with 0.1 mm distance from the last one in each direction (X and Y) in order to measure the Vickers hardness value (HV0.1) based on what has been described in reference [119]. The total number of indentations for DP600 in RSW of two plates and one plate is 4296 and 2436, respectively. However, 11050, 4944 and 3520 indentations were required to cover the entire welded joints of DP1000 in RSW of one plate and two plates as well as the welded joint of LBW, respectively. Then, the value of each indentation is assigned to a color to get an overall view of how hardness is disturbed in the welded structure.

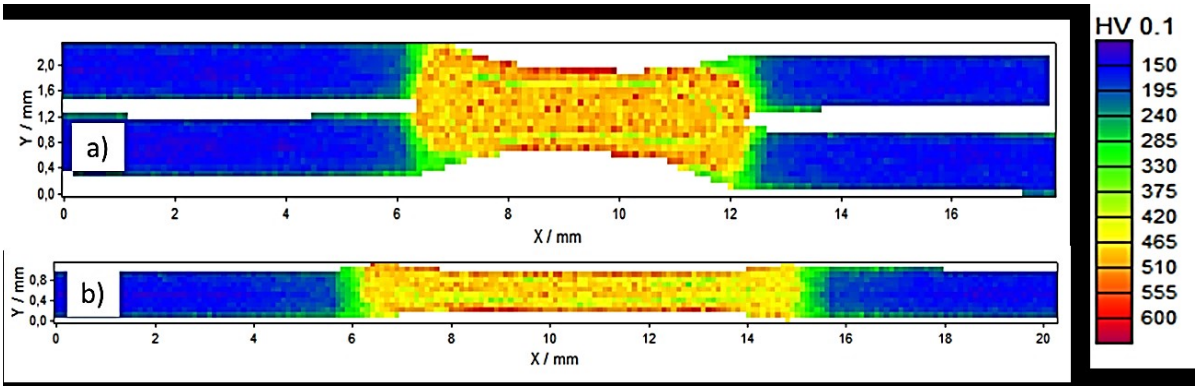

Figure 3.20 Hardness (HV0.1) mapping of DP600: (a) RSW of two plates (4296 indentations); (b) RSW of one plate (2436 indentations).

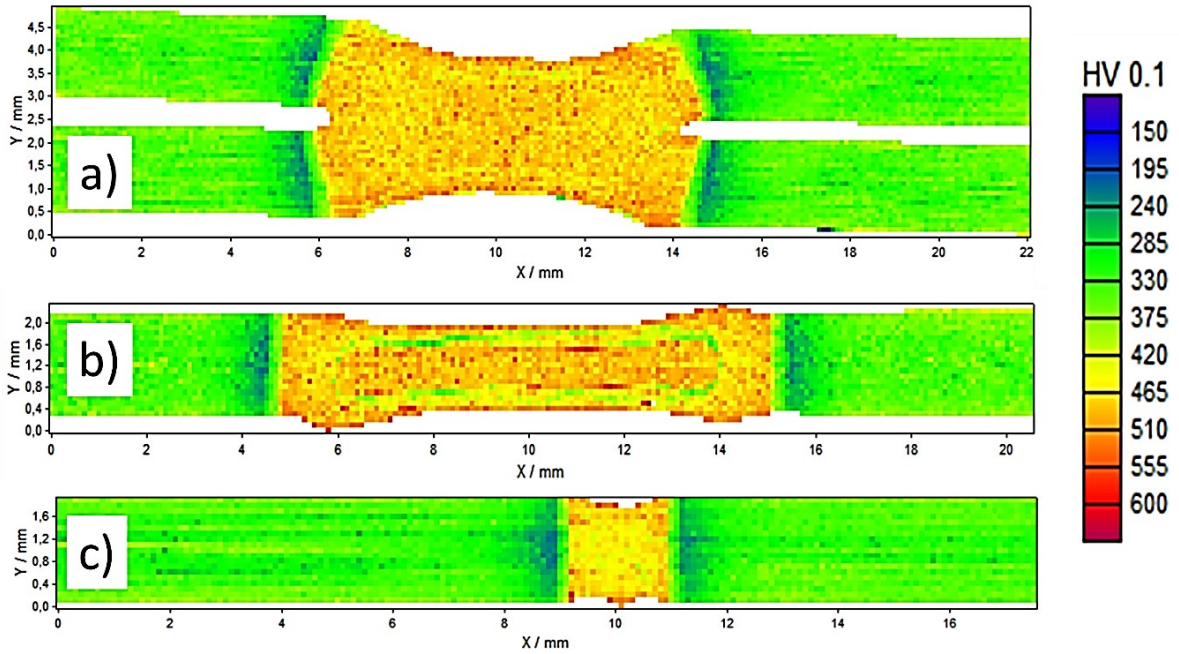

Figure 3.21 Hardness (HV0.1) mapping of DP1000: (a) RSW of two plates (11050 indentations); (b) RSW of one plate (4944 indentations); (c) LBW (3520 indentations).

The images resulted from the microstructure of RSW on one and two plates of DP600 and DP1000 show that both consist of the columnar grain of the martensitic microstructure. As expected, the Vickers hardness value of the WM of DP600 and DP1000 steels is above 400 HV1 due to the martensitic microstructure. However, as seen in Figure 3.20 (a) and (b) as well as in Figure 3.21 (b), the Vickers hardness measurement at the scale of HV0.1 shows a soft region between the WM and the HAZ. This soft area, shown as a green elliptical ring, only becomes visible by performing the indentation at scale of HV0.1. The softening at the WM boundary occurs due to carbon separation due to different cooling rate of WM and the HAZ. It results in the transformation of the low-carbon austenite into bainite-ferrite or ferrite-

martensite phase. As seen in Figure 3.22, the carbon content in the WM and HAZ is almost 0.2%. However, the carbon content is drastically reduced to almost 0.1% in a tiny area of less than 100 µm between the WM and the HAZ and leads in a softer area in the fusion zone with a ferrite microstructure, while the surrounding part has a martensite microstructure with a higher hardness value [120].

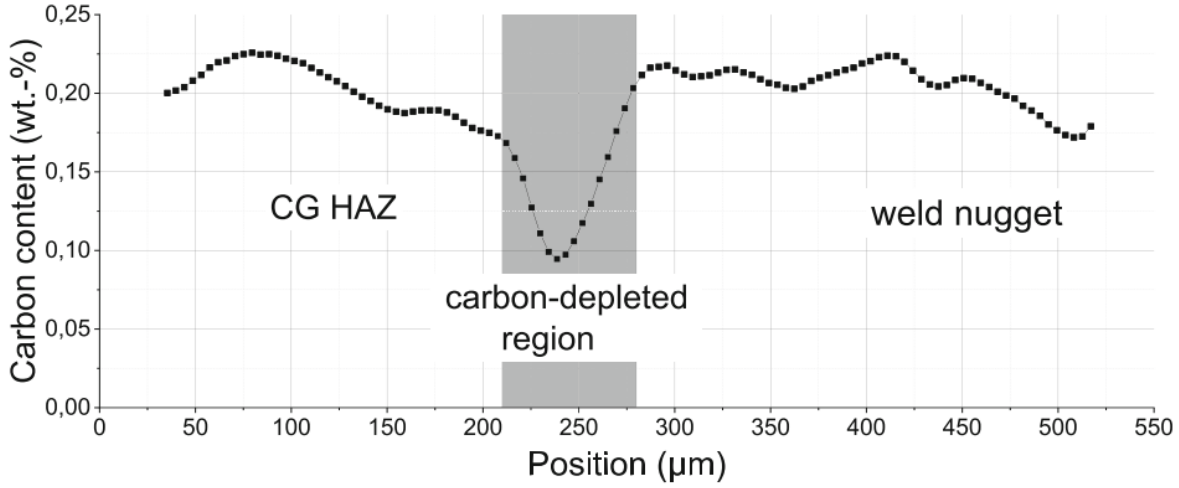

Figure 3.22 Comparison the amount of the carbon content in WM, the border of the WM and the HAZ and finally in the HAZ [120]

On the other hand, this soft area on the upper and lower side of the specimens has no significant influence on determining the weld metal's mechanical properties because it was removed by grinding during the tensile specimens' preparation. Moreover, the fracture occurs precisely in the notched area where the distance between the notches is the minimum. This area is far from the softer region and therefore cannot influence the measured stress-strain diagram by tensile test. As a result, the introduced parameters of the RSW can be used to reproduce the microstructure of the weld seam in a larger area, with lower surface deformation, similar microstructure, and without using the thermomechanical simulator.

Figure 3.23 compares the result of Vickers hardness measurement on HV1 scale performed on DP600 and DP1000 steels by RSW and LBW and S690QL by LBW. The LBW is performed with the industrial welding parameters as described in Table 3.5, and the RSW in one and two plates with the welding parameters of Table 3.2 and 3.4, respectively. It can be observed that the hardness value of WM from the different welding techniques is more than 350 HV1, which again shows the existence of the whole martensitic microstructure in this area.

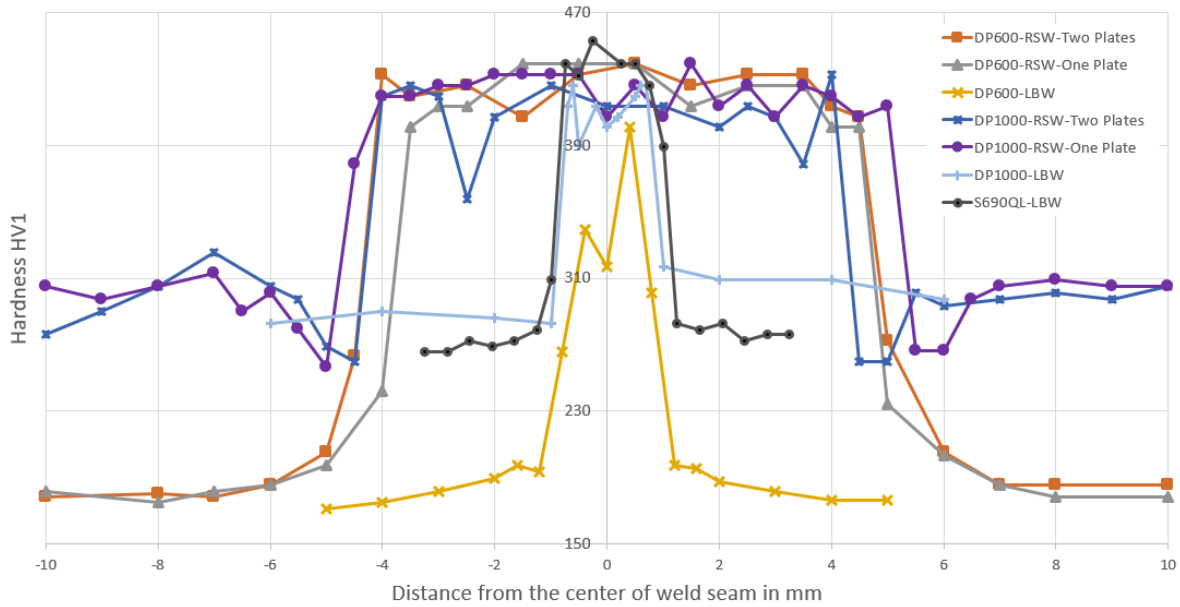

Figure 3.23 Comparison between Vickers hardness value (HV1) of DP600, DP1000 and S690QL welded with RSW and LBW. LBW on all steel plates is carried out with the welding parameters from Table 3.5, and RSW on one plate and two plates is conducted with the welding parameters from Table 3.2 and 3.4, respectively.

As seen in Figure 3.18(b), 3.19(b) and 3.23, the size of the WM reproduced by LBW with conventional welding parameters as mentioned in Table 3.5 is smaller than 2 mm for all steel grades used in this work such as DP600, DP1000 and S690QL. With the parameters mentioned in Table 3.5, the weld width becomes extremely small to produce the notched tensile specimens. In the current project, an attempt was made to reproduce the weld microstructure of the LBW process in a larger volume by varying the welding parameters such as power, defocusing and the welding velocity to induce more energy into the plates by increasing the welding power and decreasing the defocusing to increase the weld size in an interval as mentioned in Table 3.6 as mentioned in Section 3.1.3. Figure 3.24 compares the Vickers hardness value of the welded joints of DP600 obtained by LBW with the conventional welding parameters and the varied parameters in the interval of Table 3.6. For the conventional welding parameters, the welding velocity, power (p) and defocus are 1.8 mm/min, 1.6 kW and 0 mm, respectively. Then, the plates were welded at a constant velocity of 1.8 mm/min and the power was changed between 3.6 and 4.8 kW and the defocus between -40 and -100 mm. It can be seen that the weld size becomes much larger by changing the welding parameters, however, a similar microstructure cannot be reproduced. When the welding parameters are varied, the resulting microstructure's hardness value is between 250 and 300 HV1. According to the isothermal Time Temperature

Transformation (TTT) diagram of the DP-steels, it can consequently be justified that this hardness value cannot be for the martensitic microstructure [102].

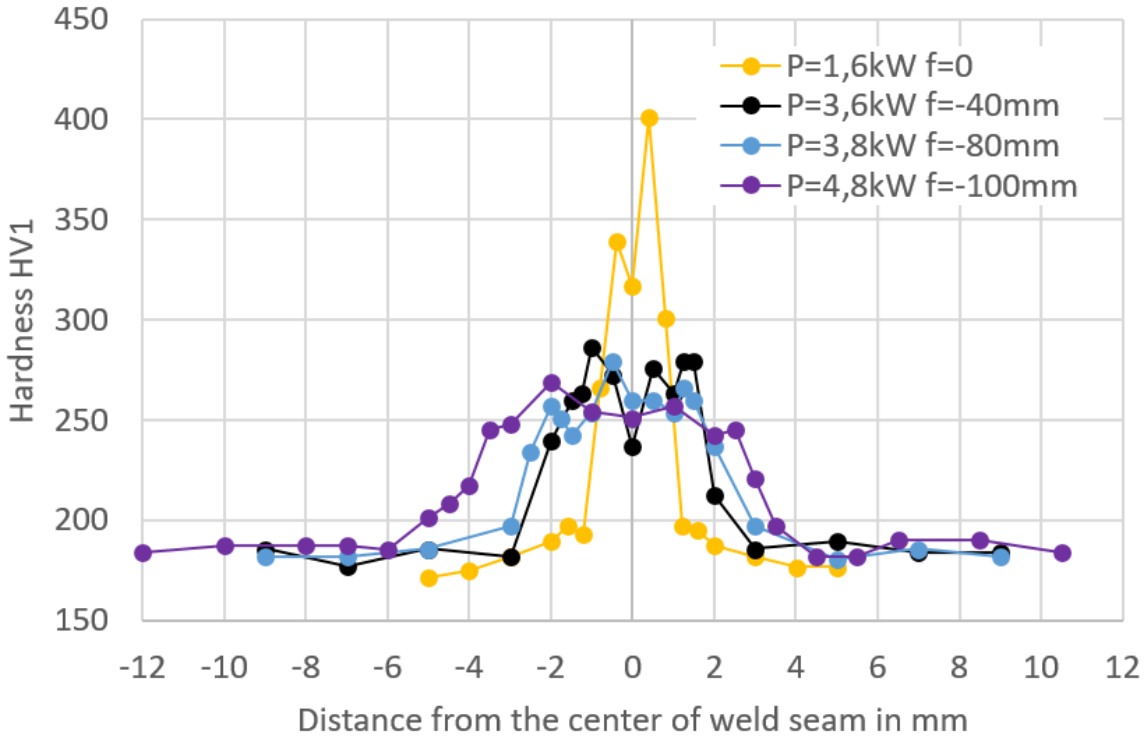

Figure 3.24 Comparison between Vickers hardness value (HV1) of DP600 welded with LBW with different welding parameters. LBW on sample of DP600 is carried out with constant welding velocity of 1.8 mm/min and different laser beam power (p) and defocus (f)

Similarly, Figure 3.25 compares the Vickers hardness value of DP1000 WMs from LBW with the conventional and varied welding parameters in the interval of Table 3.6. For the conventional welding parameters, the welding velocity, power (p) and defocus are 1.8 mm/min, 2.4 kW and 0 mm, respectively. Then, the plates were welded with similar velocity and the power was changed between 8.4 and 13.7 kW and the defocus between -40 and -100 mm. Exactly the same as DP600, the size of WM becomes much larger by changing the welding parameters, nevertheless, the new welding parameters cannot generate the similar microstructure. The hardness value of the resulting microstructure is between 250 and 400 HV1, which does not belong to the martensitic microstructure. Therefore, the attempts to reproduce the WM of LBW on a larger volume by varying the welding parameters failed.

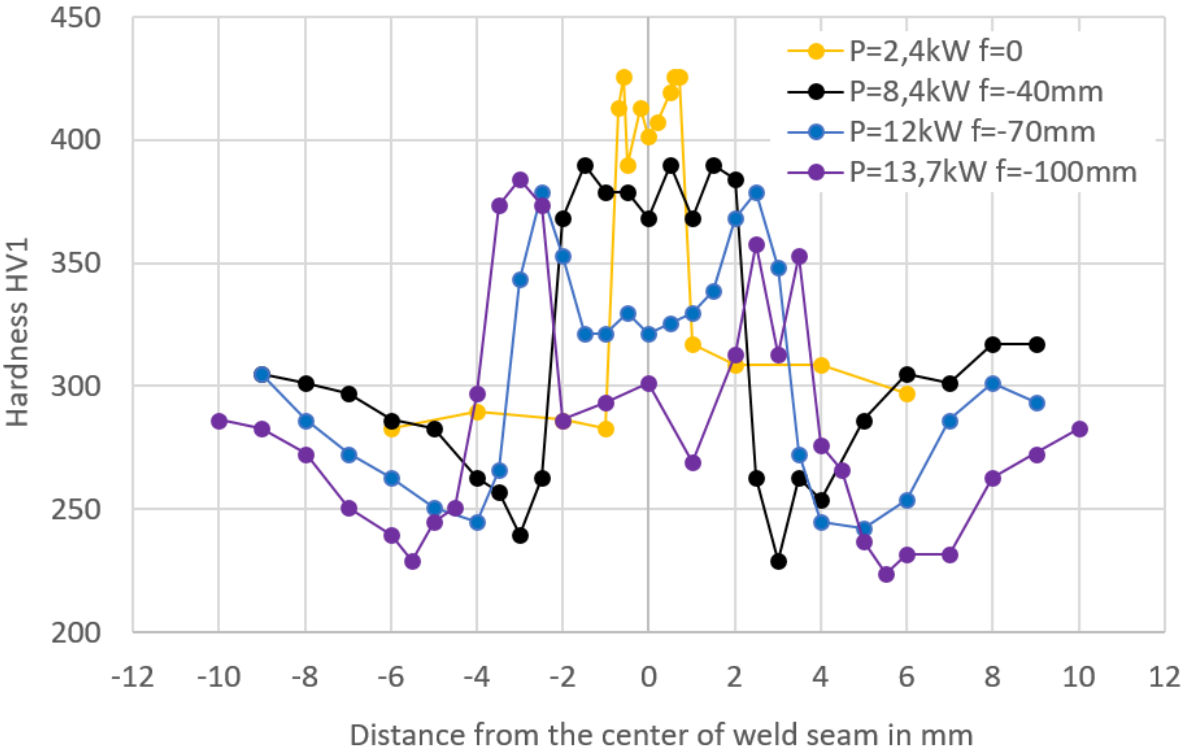

Figure 3.25 Comparison between Vickers hardness value (HV1) of DP1000 welded with LBW with different welding parameters. LBW on sample of DP1000 is carried out with constant welding velocity of 1.8 mm/min and different laser beam power (p) and defocus (f)

In summary, it has been shown that it is possible to regenerate the microstructure of the WM from RSW of two steel sheets in only one sheet and in a larger area by changing the welding parameters. However, it is not possible to reproduce the WM of LBW in a bigger area with the same methodology. Therefore, the mechanical properties of the WM of RSW can be determined from notched tensile specimens, as described in the next section. Nevertheless, the mechanical properties of WM of LBW can be obtained by performing the instrumented indentation test together with inverse analysis by the finite element method as explained in chapter 4.

3.2.2. Determining the Material Parameters

The objective of this section is to demonstrate initially the experimental results of the tensile tests performed on the smooth and notched tensile specimens from BM or WM of the utilized AHSSs. In the second part of this section, the accuracy of the material model used to describe the mechanical properties of the AHSSs in both BM and WM is evaluated. In the next step, the material parameters of WM from RSW of DP600 and DP1000 are calculated based on the geometry factor obtained by

comparing the smooth and notched tensile specimens from BM. Then, the introduced methodology is verified by comparing the experimental result of the notched-welded tensile specimens with the stress-strain diagram obtained from the simulated notched tensile specimens with the calculated material parameters of WM.

3.2.2.1. Experimental Analysis

The quasi-static tensile tests were performed on the smooth and notched tensile specimens of BM and WM. The strain was measured locally using the DIC systems as described in Section "3.1.4.1. Experimental Analysis". Figure 3.26 shows the local strain distributions on the notched and welded tensile specimens of DP600 and DP1000. As shown in Figure 3.26 (a), the strain distribution on the notched and welded tensile specimens with the geometry shown in Figure 3.9 (e) is maximum in the notched region where the WM is located. Therefore, such geometry can lead to the determination of the mechanical properties of DP600 WM from RSW. Figure 3.26 (b) shows the local strain distribution on the notched-welded tensile specimens of DP1000 with the geometry as depicted in Figure 3.10 (c). It can be seen that the maximum strain appears as well in the notched region where the WM is available.

However, performing the tensile test on the notched and welded tensile specimens of DP600 with small notch radius with the geometry of Figure 3.9 (c) shows that the maximum value of local strain occurs outside the notched region, as shown in Figure 3.26 (c). This is because the yield strength of DP600 WM is extremely higher than that of DP600 BM. Therefore, a notch with a radius of 1.5 mm is not large enough to observe the fracture in WM and consequently the stress-strain diagram of WM DP600 cannot be obtained. This is the reason why two different types of notched tensile specimens of DP600 are produced. However, since the aim of the current research is to determine the mechanical properties of WM DP600 from RSW, further analysis is performed only on the notched tensile specimens of DP600 with a large notch size with the geometry of Figure 3.9 (d) and Figure 3.9 (e).

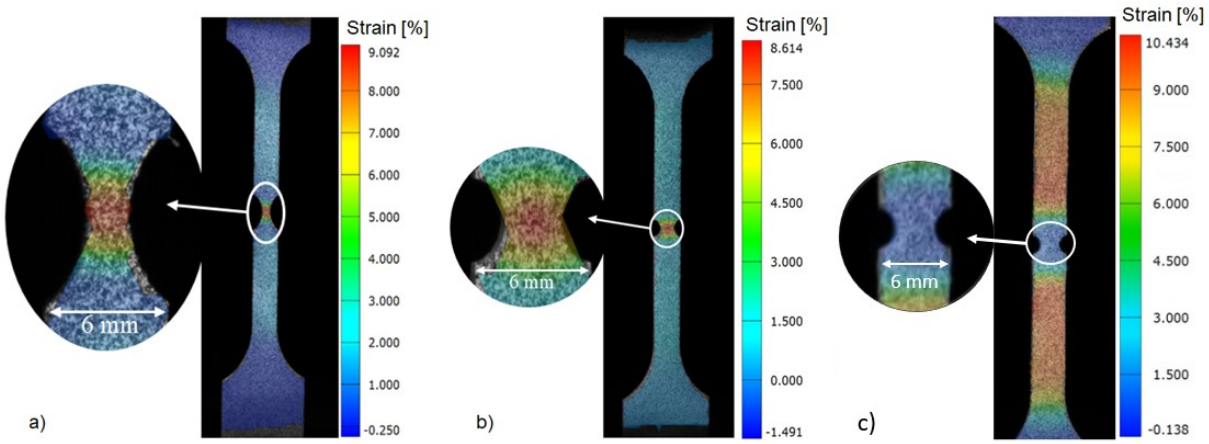

Figure 3.26 Strain distribution of the notched and welded (RSW) specimens before fracture; (a) DP600 with large notch radius with the geometry of Figure 3.9 (e); (b) DP1000 with notch radius as shown in Figure 3.10 (c); (c) DP600 with small notch radius with the geometry of Figure 3.9 (c)

Table 3.7 shows the mechanical properties of the AHSS in BM and WM obtained by performing the tensile test on the smooth or notched tensile specimens. As shown in Figure 3.8 (a) and Figure 3.9 (a), the smooth tensile specimens of DP600 were prepared with two different geometries. However, the stress-strain curves obtained by performing the tensile test on both specimens are similar. The reason for making the smooth tensile specimens with the geometry of Figure 3.9 (a) is to compare two identical specimens, one containing a notch (Figure 3.9 (b)) and the other one smooth (Figure 3.9 (a)), in order to calculate the geometry factor. The same procedure was repeated for DP1000 with the specimen geometry as presented in Figure 3.8 (c) and Figure 3.10 (a).

Tensile test was performed on three specimens of each used AHSS or in other words each sample type such as smooth or notched specimens and then the average results were calculated and presented in Table 3.7. Analyzing the result of the notched and notched-welded specimens of DP600 and DP1000 show that RSW leads to a reduced total elongation at the maximum force. It can be concluded that the microstructural changes reduce ductility and increase the strength of the material. The yield and tensile strength are enhanced by 140% and 87% in the case of DP600 and by 44% and by 28% for DP1000 after RSW. The higher magnitude in the growth of yield and tensile strength after welding of DP600 compared to DP1000 may result from the fact that DP600 BM has lower strength than DP1000 BM. However, the WM of both steels has a similar martensitic microstructure after RSW.

Table 3.7 Mechanical properties of DP600, DP800, DP1000 and S690QL (mean values) based on the true stress-strain diagram

Material		Yield strength in MPa	Tensile strength in MPa	Strain hardening exponent	Total elongation at maximum force in %
DP600	Smooth sample	360 ± 1.73	633 ± 2	0.216 ± 0.002	18.7 ± 1.1
	Notched sample	430 ± 10.07	698 ± 2	0.124 ± 0.009	15.8 ± 1.37
	Notched-welded sample (RSW)	1036 ± 3.06	1304 ± 10.82	0.049 ± 0.008	4.18 ± 0.26
DP800	Smooth sample	531 ± 2	877 ± 6	0.165 ± 0.002	14.27 ± 1.3
S690QL	Smooth sample	690 ± 2.69	883 ± 2.1	0.162 ± 0.003	12.2 ± 0.98
DP1000	Smooth sample	630 ± 2.08	1025 ± 1.53	0.096 ± 0.002	8.3 ± 0.036
	Notched sample	800 ± 36.3	1145 ± 8.08	0.104 ± 0.003	8.7 ± 0.376
	Notched-welded sample (RSW)	1150 ± 20.5	1460 ± 13.44	0.057 ± 0.008	4.3 ± 0.25

The stress-strain diagrams from the tensile tests performed on different tensile specimens of DP600 are shown in Figure 3.27. The tensile test was performed three times on each specimen of DP600 and the mean value and standard deviation are shown in Figure 3.27 and Table 3.7, respectively. The geometry of the smooth, notched and notch-welded tensile specimens of DP600 with thickness of 0.4 mm are shown in Figure 3.9 (a), Figure 3.9 (d) and Figure 3.9 (e), respectively. As explained in Section 3.1.4.1, called experimental analysis, the center of a virtual extensometer with a length of 1 mm is located in WM exactly where the crack starts and the fracture occurs to measure the true strain. Then, the applied force on each side of the tensile specimens was divided by the actual cross-section of the notched area obtained from the optical measurement with the Aramis system to calculate the true stress.

It can be observed that the stress-strain diagrams of the smooth and notched tensile specimens of DP600 from BM are parallel to each other, though the magnitude of the true stress obtained from the notched tensile specimens is higher than that of the smooth specimens, due to the stress concentration factor caused by the notched geometry. Nevertheless, it is possible to transfer and map the stress-strain diagrams of notched and smooth specimens if the value of the geometry factor is available, which will be calculated in the next section. The stress-strain diagram of the notched specimens from WM of DP600 shows an extremely higher value of true stress compared to the specimens from BM. This is expected due to the martensitic microstructure and the consequently higher strength of WM, as well as the existence of the notch in the tensile specimens.

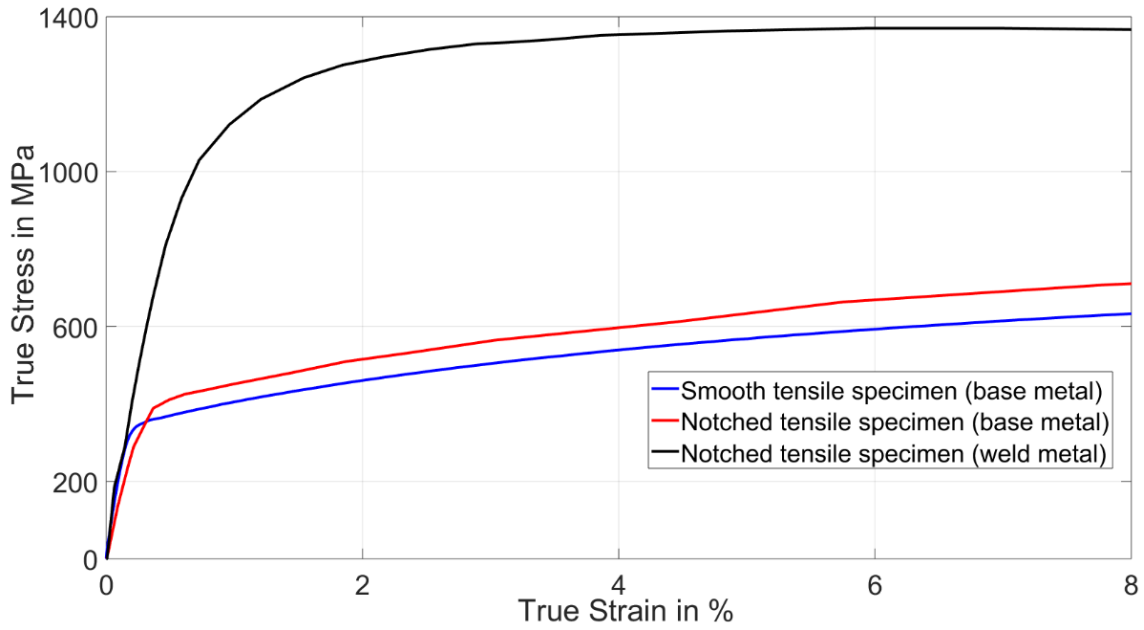

Figure 3.27 True stress–strain curves of smooth, notched, and notched-welded (RSW) specimens of DP600 (mean value), the geometry of the samples are shown in Figure 3.9 (a), Figure 3.9 (d) and Figure 3.9 (e) respectively

On a similar basis, Figure 3.28 shows the stress-strain diagrams from the tensile tests performed on different tensile specimens of DP1000. Exactly the same as DP600, the tensile test was performed three times on each specimen of DP1000. The mean and standard deviation are shown in Figure 3.28 and Table 3.7 accordingly. Figure 3.10 (a), Figure 3.10 (b) and Figure 3.10 (c) show the geometry of the smooth, notched and notch-welded tensile specimens of DP1000 with thickness of 1 mm. The methodology for measuring the true stress-strain diagram of the DP1000 specimens is similar for the DP600 specimens.

Predictably and similar to DP600, the stress-strain curve measured on the notched-welded specimens of DP1000 is in a much higher level than the stress-strain diagram of specimens from BM DP1000 due to the martensitic microstructure in the notched region. Although the magnitude of the true stress obtained from the notched tensile specimens of BM DP1000 is higher than the true stress of the smooth specimen as a result of the notch, both graphs are parallel to each other.

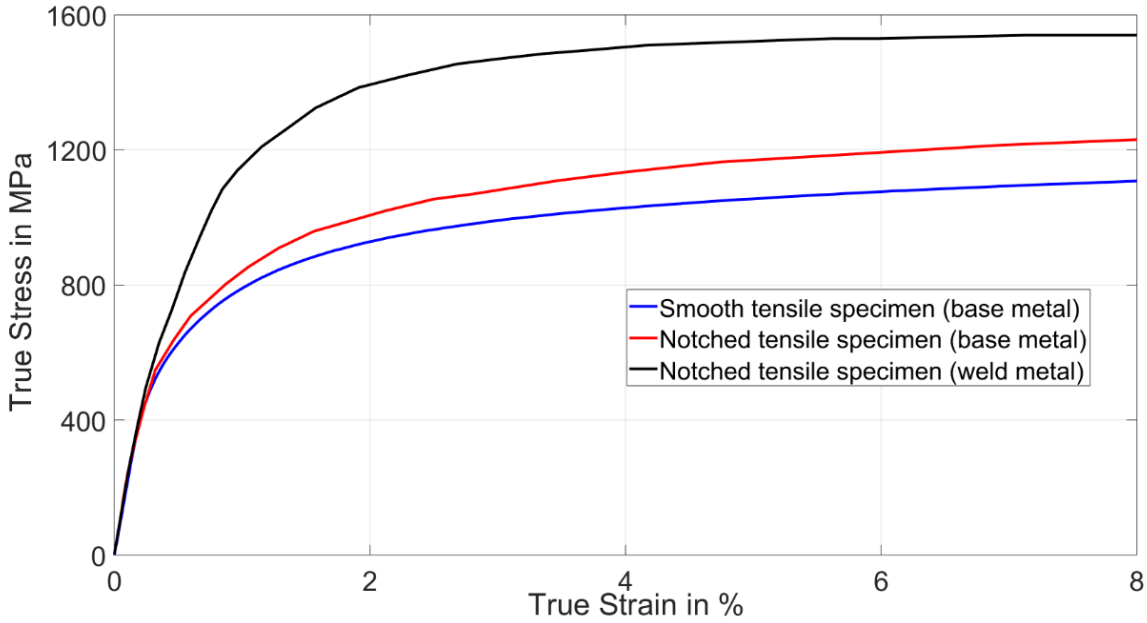

Figure 3.28 True stress–strain curves of smooth, notched, and notched-welded (RSW) specimens of DP1000 (mean value), the geometry of the samples are shown in Figure 3.10

The mechanical properties of WM based on the smooth tensile specimens, which is the focus of this section, can be calculated from multiplying the geometry factor by the stress-strain diagram of the notch-welded tensile specimens which will be explained in more details in the next section.

3.2.2.2. Numerical Analysis

The focus of the present work is to determine the material parameters of AHSSs in both BM and WM using the trained ANN together with the IIT data. Since welding does not significantly change the magnitude of the elastic modulus, the behavior of AHSSs in both WM and BM is similar in the elastic region. However, the parameters describing the plastic behavior of AHSSs, such as yield strength, tensile strength, and ductility, are remarkably varied after welding. Therefore, the trained ANN must concentrate on calculating the stress-strain diagram in the plastic region, which is above the yield point. On the other hand, IIT cannot predict the total strain of AHSSs and fail to calculate the total strain at fracture. Consequently, a material model capable of calculating the stress-strain diagram of AHSSs in the plastic region up to the maximum value of the experienced engineering stress as accurately as possible must be used.

Voce nonlinear isotropic strain hardening material model as described in Equation (2.1) and Figure 2.2 with four parameters of yield strength ($R_{p0.2}$ in MPa), slop of tangent line at maximum value of overstress (R_0 in MPa), the differences between the yield strength and the tangent line at maximum value of overstress at the point where the plastic strain is zero (R_∞ in MPa) and the saturation rate (b) can describe the plastic behavior of the AHSSs in both BM and WM up to maximum value of overstress as exactly as possible. The above material parameters were calculated from the true stress-strain diagram of the AHSSs and presented in Table 3.8. To determine the material parameters, the tensile specimens were numerically simulated and the material parameters were repeatedly changed to find the best matches, which are obtained when there is the least mean squared error between the stress-strain curves from the tensile test and the numerical simulation.

The parameters of the Voce material model are calibrated based on the true stress-strain diagram of AHSS in the strain hardening range, which goes from yield strength to ultimate strength, based on the type of microstructure and steels used. The calibration of the material model was performed in an interval starting with DP600 BM, which has the lowest yield strength equal to 360 MPa, and ending with the measured yield strength at 1150 MPa, which belongs to the notched-welded specimens of DP1000. It is not required to make the calibration of the material model parameters larger and expand them to other ranges, since the parameters are later varied only in the interval of the least and most strength steels used, and must calculate the true stress-strain diagram in the plastic range up to the ultimate strength.

Table 3.8 Material model parameters of DP600, DP800, DP1000 and S690QL determined based on Voce non-linear isotropic hardening model from the true stress-strain diagram

Material		$R_{p0.2}$ in MPa	R_0 in MPa	R_∞ in MPa	b
DP600	Smooth sample	360	710	268	22
	Notched sample	430	1300	207	25
	Notched-Welded sample (RSW)	1036	120	325	125
DP800	Smooth sample	531	440	422	27
S690QL	Smooth sample	690	393	184	17
DP1000	Smooth sample	630	1100	390	72
	Notched sample	800	1250	340	75
	Notched-Welded sample (RSW)	1150	200	380	100

The computed true stress as the output of the material model in a certain range of plastic strain is compared with the measured true stress at the corresponding plastic strain to investigate the accuracy of the used material model and its presented parameters to calculate the stress-strain curves of AHSSs. For example, the difference between the magnitude of the true stress at 1% plastic strain between the result of the tensile test on the smooth specimens and the material model is 6 and 36 MPa for DP600 and DP1000, respectively, as seen in Figure 3.29. At 4% plastic strain, the accuracy of the material model in calculating the true stress increases and the stated differences decrease to about 5 and 1 MPa for DP600 and DP1000, accordingly. At plastic strain of ultimate strength, which is more than 18% and 8% for DP600 and DP1000, respectively, the differences between the measured and calculated true stress reaches to 2 and 6 MPa, correspondingly. Similarly, the material model can predict the true stress at 1% plastic strain of DP800 BM with an accuracy of 6 MPa. The deviation between the model output and the measured value of the tensile test at DP800 BM at 4% and 14% plastic strain is only 1 MPa.

The used material model can additionally estimate the true stress-strain curve of the notched tensile specimens with an extremely high accuracy. The differences between the true stress at plastic strain of 3% and 6% between the output of material model and the measured value from the notched tensile specimens of DP600 BM is 6 and 8 MPa, respectively. The mentioned differences decrease by notched tensile specimens of DP1000 BM at plastic strain of 2% and 6% to around 3 MPa each. Besides, the applied material model works well to calculate the true stress-strain of notched-welded tensile specimens. As an example, the mismatch between the true stress at 1% and 4% plastic strain of notched-welded tensile samples of DP1000 is about 7 and 2 MPa, correspondingly. As a result, it can be concluded that the used material model is able to follow the true stress-strain curves of AHSSs in both BM and WM with an extremely high accuracy.

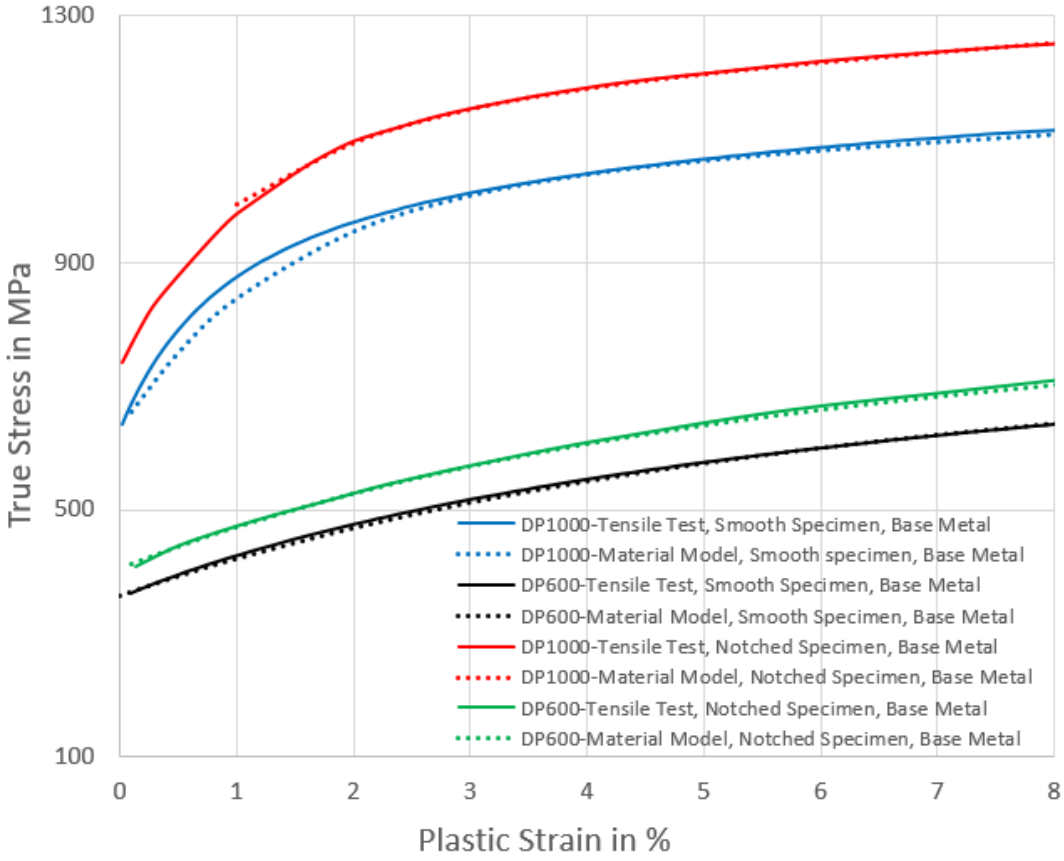

Figure 3.29 Comparison between the true stress-strain diagram obtained from the notched and smooth tensile specimens from BM of DP600 and DP1000 with the stress-strain diagram calculated according to the determined material model parameters of DP600 and DP1000 steels

Following computation of the material model parameters for the different types of specimens from BM and WM of AHSSs, there is a need to compute the material model parameters of AHSSs in WM based on the smooth-welded tensile specimens. Since such a specimen type was not provided, it is required to calculate the material parameters of WM by multiplying the material parameters of notched-welded tensile specimens by the geometry factor. The geometry factor must be calculated by comparing the notched and smooth tensile specimens of BM made of similar material. Figures 3.27 and 3.28 compare the experimental stress-strain responses of notched and smooth tensile specimens of DP600 and DP1000, respectively, and show that they are parallel to each other. However, further investigation is needed to analyze the effect of thickness and size of notch radius on the stress-strain diagram of a material. Then, a tensile specimen based on the geometry of Figure 3.10 (b) was numerically simulated with the material parameters of the smooth specimen of DP1000, as shown in Table 3.8. The simulation was repeated several times with different plate thicknesses (0.4 and 0.9 mm) and different geometry ratios (0.4, 1, 2

and 4) which is the division of the distance between the notches (D) by the notch radius (R).

As seen in Figure 3.30 and as expected, the stress-strain curve moves upwards with increasing geometry ratio. The stress-strain curves of smooth specimens with a thickness of 0.4 and 0.9 mm are similar and located in the lowest position. In contrast, the stress-strain diagram of DP1000 with a geometry ratio of 4 is in the uppermost interval. However, changing the geometry ratio with similar plate thickness shifts the diagrams up or down parallel to each other. Depending on the geometry ratio, the specimens with thicker plate may have a higher or lower amount of overstress. For example, stress-strain path is higher for thicker plate specimens than for thinner specimens when the geometry ratio is equal to or less than 1. On the other hand, it can be observed that with increasing geometry ratio, the deviation between the stress-strain curves of a specimen with different thickness becomes larger at higher values of plastic strain. Furthermore, the stress-strain curve of notched specimens with an extremely high geometry ratio, such as 10, is no longer parallel to smooth tensile specimen. However, the geometry ratio of the specimens used in this work is equal to or less than 2, and consequently, the resulting stress-strain curves of the notched specimens are parallel to the smooth specimens, as observed from the experimental and numerical results. Therefore, it is possible to calculate the mechanical properties of smooth-welded tensile specimens from the notched-welded tensile specimens by having the value of geometry factor.

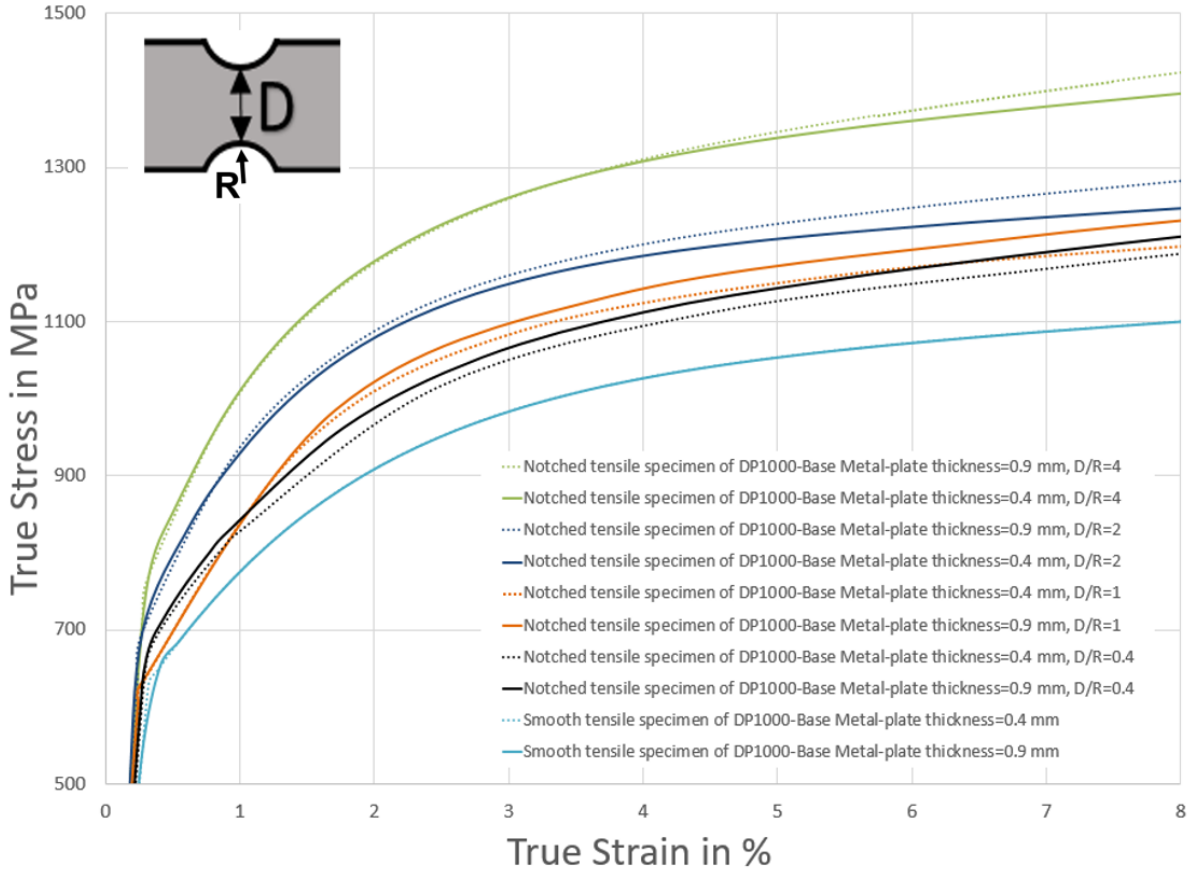

Figure 3.30 Comparison between the true stress-strain curves of smooth and notched tensile specimens based on the different value of geometry ratio (D/R) and plate thickness for the DP1000 BM; geometry ratio is the division of the distance between the notches (D) by the notch radius (R)

The geometry factor of DP600 and DP1000 specimens can be calculated by comparing the material model parameters of smooth and notched tensile specimens made of base metal with the geometry described in Figure 3.9 (a and d) and Figure 3.10 (a and b), respectively, and with the parameters listed in Table 3.8. The notch radius of the DP600 specimens is larger than the notch radius of the DP1000 specimens, therefore the geometry ratio of the DP600 specimens is smaller than that of the DP1000 specimens and is 0.51 compared to the value of 2 for the DP1000 specimens. The resulting geometry factor calculated for each material model parameter of DP600 and DP1000 specimens are shown in Table 3.9 which quantifies the effect of notch geometry on the deviation of material parameters calculated from smooth standard tensile specimens.

As seen in Table 3.9, the geometry factor of two material model parameters ($R_{p0.2}$ and R_{∞}) of DP1000 are higher than DP600 because the geometry ratio of DP1000 specimens, which is 2, are higher than that of DP600 specimens, which is 0.51. It can

be justified so that increasing these two parameters which describe the yield strength and the ultimate maximum overstress, respectively, can move the stress-strain diagram upward. It is also explained that increasing the geometry ratio can shift the stress-strain diagram towards the top. Consequently, the geometry factor of two material model parameters is anticipated to grow by raising the geometry ratio. However, the geometry factor of two other material parameters which describe the slop of tangent line at maximum value of overstress (R_0) and the saturation rate (b) are higher for DP600 compared to DP1000 specimens. These two material parameters show how fast the ultimate stress can be reached and are related to the slope of the stress-strain curves. As seen in Figure 3.30, the thickness of the specimens can change the line slope of stress-strain diagram and as mentioned the thickness of DP600 and DP1000 are not similar. Therefore, the narrower magnitude of geometry ratio and plate thickness of DP600 specimens compared to DP1000 cause the stress-strain diagram of DP600 notched specimens to move upward less than the stress-strain diagram of DP1000 notched specimens, though with a higher saturation rate.

Table 3.9 Geometry factors between the smooth and notched specimens made from base metal of DP600 and DP1000 obtained from true stress-strain diagram

Material		$R_{p0.2}$ in MPa	R_0 in MPa	R_∞ in MPa	b
DP600	Geometric factors	1.19	1.83	0.77	1.14
DP1000	Geometric factors	1.27	1.14	0.87	1.04

In the last step, using the geometry factor from Table 3.9 and the material parameters of notched tensile specimens, the material model parameters of the weld metal based on a smooth-welded tensile specimen are calculated and presented in Table 3.10. As seen, the differences between the material parameters of WM in DP600 and DP1000 are smaller than the differences between the material parameters of BM of both steels due to the complete martensitic microstructure in WM made by RSW. For instance, the yield strength of DP1000 BM is around 75% higher than the yield strength of DP600 BM, however, the yield strength of DP600 WM is only 4% lower than the yield strength of DP1000 WM. The other material parameters such as saturation rate and ultimate maximum overstress follows also the similar pattern. On the other hand, the comparison of the material parameters of WM with BM of a steel, such as DP600, shows that the yield strength increases dramatically around 140%, yet the material

parameters that identify the ductility of a steel show a different behavior. For example, the differences between the ultimate stress and yield strength increases with the enhancement of the saturation parameter after RSW of DP600 steel, which shows that the WM reaches its maximum overstress magnitude extremely faster than BM describing the brittle behavior of WM.

Table 3.10 Material model parameters of DP600 and DP1000 on weld metal resulted from RSW

Material		$R_{p0.2}$ in MPa	R_0 in MPa	R_∞ in MPa	b
DP600	Smooth-welded sample	867	65	420	110
DP1000	Smooth-welded sample	906	175	437	96

To verify the accuracy of used material model and obtained material parameters, tensile specimens of DP600 and DP1000 are simulated numerically by using the determined material model parameters and then the output of simulation model is compared with the measured true stress-strain curve from the tensile test. As described in Section "3.1.4.2. Numerical Approach", the true stress-strain diagram of AHSSs is measured using the DIC system, and the calculated true stress is computed by constantly considering the actual cross section, which is located exactly in the center of the notch region and is perpendicular to it. On the other hand, the true strain is calculated by computation of the displacements between two points located on each side of the fracture path in the notch area. The smooth and notched tensile specimens of BM were simulated with material parameters obtained from smooth tensile specimen as standard sample. Then, the notched-welded specimens were simulated with two types of material parameters; the region where the WM is located was simulated with material parameters of smooth-welded specimens, as mentioned in Table 3.10, and the other region belonging to the base metal is simulated with the material parameters of smooth tensile specimens of BM. With this methodology, it is possible to confirm the correctness of the calculated material parameters of the WM.

Figure 3.31 compares the true stress-strain curves obtained from the quasi-static tensile test and the numerical simulation of tensile specimens with the determined material parameters of the DP600 specimens. As expected, the simulation model used the determined material model parameters can follow the experimental results with extremely high accuracy, especially for DP600 BM. However, a slight deviation between the curves obtained from numerical and experimental work on notched-

welded specimens of DP600 can be observed after 4% plastic strain. This difference can be justified by the fact that it was tried to find the best match for the material parameters only up to the ultimate strength and the plastic strain higher than almost 4% exceeds this limit for notched-welded DP600 specimens.

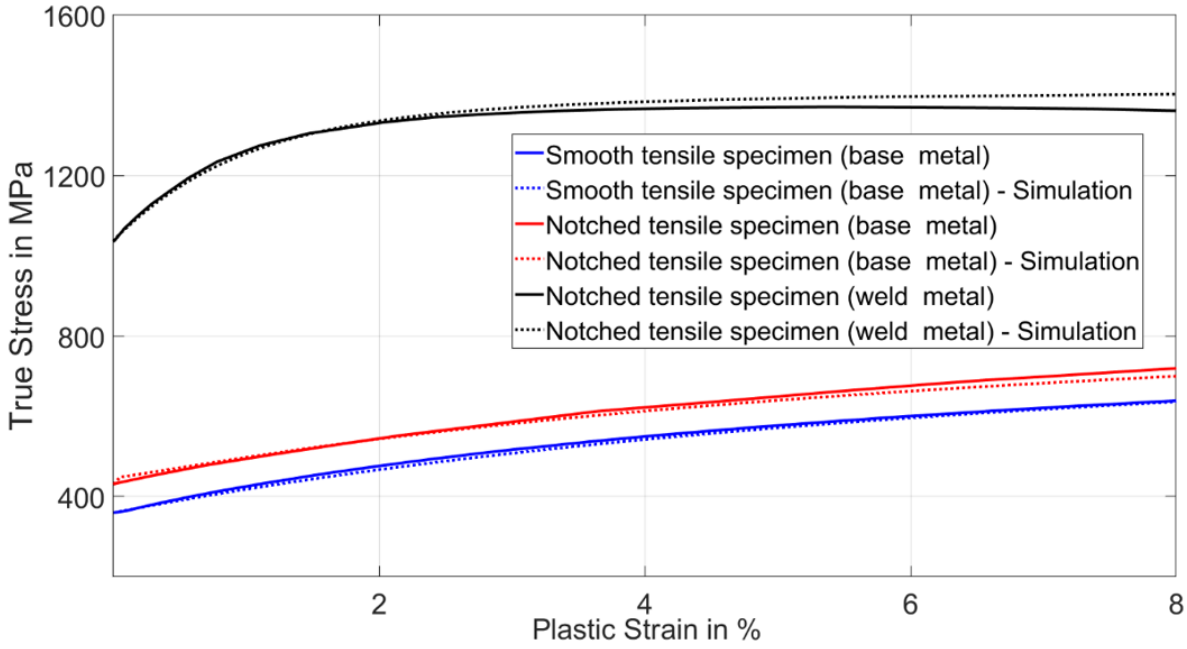

Figure 3.31 Comparison between the true stress–strain curves of smooth, notched, and notched-welded (RSW) specimens of DP600 (mean value) with stress-strain curve obtained from the numerical simulation model of tensile specimens with material model parameters of Table 3.7

As with DP600, a comparison between the output of the simulation model for DP1000 tensile specimens and the measured output is shown in Figure 3.32. As expected and similar to DP600, the simulation model using the determined material model parameters of DP1000 agrees with the experimental results with extremely high accuracy. However, it can be observed that there is a wider deviation between the tensile test result and the numerical simulation in smooth tensile specimens when the plastic strain is less than 2%. It can be justified by the fact that the calibration of the material model on DP1000 BM at 1% plastic strain, as explained before, has a higher deviation (36 MPa) compared to other ranges of plastic strain for other steels, consequently a little difference can be noticed in this case.

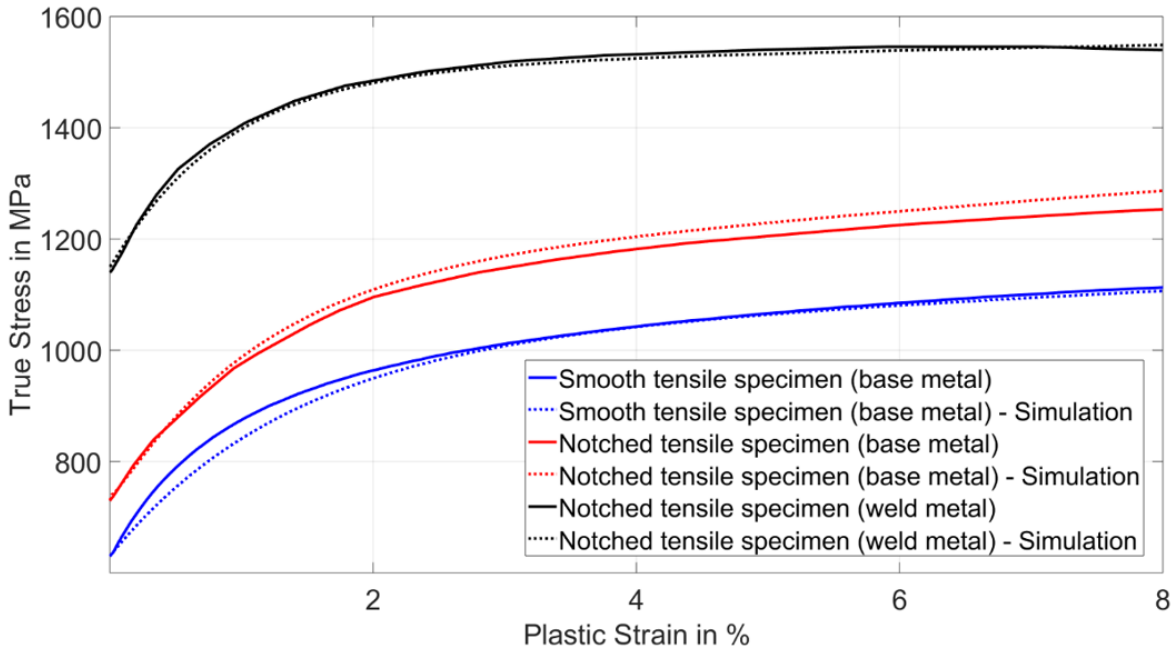

Figure 3.32 Comparison between the true stress–strain curves of smooth, notched, and notched-welded (RSW) specimens of DP1000 (mean value) with stress-strain curve obtained from the numerical simulation model of tensile specimens with material model parameters of Table 3.7

In summary, it can be confirmed once again that the introduced material model and its identified parameters based on the concept of geometry factor can estimate the mechanical properties of AHSSs in both WM and BM with quite high accuracy. In the next step, the obtained results will be confirmed with the available data from other research works.

3.2.3. Methodology Validation

The calculated material model parameters of WM from RSW of DP600 and DP1000 specimens with thickness of 0.4 and 0.9 mm, respectively, are compared with the results of Dancette [7] in Figure 3.33 to validate the introduced method. Dancette investigated the mechanical properties of HAZ from RSW DP980 with sheet thicknesses of 1 and 3 mm. He used a Gleeble 3500 thermomechanical simulator system to reproduce the microstructure of HAZ from RSW in larger area to prepare a smooth tensile specimen and then perform the quasi-static tensile test. The DP980 plates with thickness of 1 and 3 mm are heated both firstly to 1200 ℃ and then the cooled with different rate. The cooling time DP980 with thickness of 1 mm ($t_{8/5}$∼1s) is less than DP980 with thickness of 3 mm ($t_{8/5}$ ∼2s). As can be seen in Figure 3.33 on

the stress-strain curves of DP980, different plate thicknesses and different cooling rates resulting in different microstructure cause a deviation of almost 200 MPa in ultimate tensile strength. Therefore, it is expected that DP600 and DP1000 plates initially welded at thicknesses of 1 and 2 mm and then ground to thicknesses of 0.4 and 0.9 mm exhibit slight variation in the stress-strain curves when compared with each other. However, the stress-strain diagram of DP600 and DP1000 WM lies exactly between the DP980 HAZ sheets with martensitic microstructure and shows similar behavior to them.

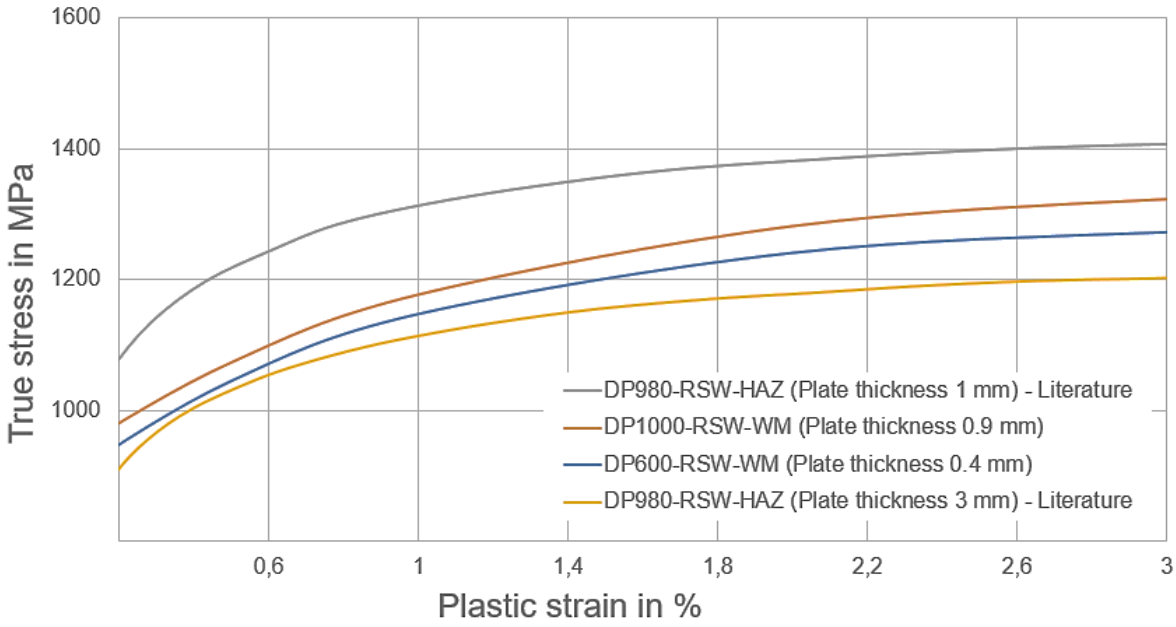

Figure 3.33 Comparison between the true stress-strain diagram of WM from RSW of DP600 and DP1000 plates calculated in the current research work with the result of stress-strain diagrams according to martensitic microstructure of HAZ DP980 of RSW from the literature [7] which uses a thermomechanical simulator to reproduce the martensitic HAZ microstructure in a larger region

The comparison between the results obtained from the literature [7] and the methodology used in the current research work confirms again the robustness and trustworthiness of the obtained diagram for characterizing the mechanical properties of WM without using a thermomechanical simulator. As explained in details, the differences in the stress-strain curves are originated from the different cooling rate of RSW on DP600 and DP1000 plates compared to the simulated DP980 plates. On the other hand, different geometries and thicknesses of the tensile specimens may slightly change the stress-strain diagram. The result of this chapter will be used in the next sections to validate the numerical model of IIT and also the correctness and accuracy of the trained ANNs to determine the material model parameters of AHSSs in WM and BM.

4. Instrumented Indentation Technique

The first step to train and validate the ANNs capable of determining the mechanical properties of AHSSs in both BM and WM is to calculate the material model parameters of the test steels, which were measured and calculated in the third chapter. However, the mechanical properties of WM from LBW or HAZ from RSW cannot be calculated using the methodology presented in the third chapter due to the small size of the target zone. Therefore, in this chapter, another methodology based on the inverse analysis of the instrumented indentation test (technique), as explained in the section " 2.4.2. Inverse Analysis by means of Finite Element Method", is applied to calculate the mechanical properties of the mentioned zones.

Moreover, it is necessary to study the procedure of performing the IIT to understand the resulting force-indentation depth curves and additionally deformed surfaces caused by the indentation test. The experimental analysis of the IIT and the measured data can be used to validate the numerical simulation model of the IIT, which must later be applied to generate a large volume of datasets to train the ANNs. Moreover, the measured force-indentation depth curves and the deformed surfaces with corresponding material model parameters of the investigated steels are finally used to test the accuracy of the trained ANNs.

The current chapter first begins with an explanation of the instrumented indentation testing machine as the core of the methodology used to achieve the two objectives already mentioned. Then, the procedure for performing the IIT and the steps for providing the specimens for the indentation test are described. In the next step, the optical measurement equipment used to examine the deformed surface of the

indented specimens is presented. Afterwards, in the present chapter, the results of the IIT on the AHSSs in BM and WM are depicted and the profile of the indented surfaces that is measured with the optical sensor is demonstrated. Finally, the numerical simulation model of the IIT with the applied boundary conditions and mesh sizes is outlined and its accuracy is discussed, and the results are compared with the findings of the experimental analysis. At the end, the material model parameters of WM of LBW and HAZ of RSW are calculated with the validated numerical simulation model of IIT according to the concept of inverse analysis.

4.1. Methodology

The conduction of IIT is to some extent similar to hardness measurement, though the force and indentation depth must be recorded simultaneously by incrementing the magnitude of the applied force, and this information can be aggregated in the form of a force-indentation depth curve. Thus, the main difference between IIT and hardness measurement that is relevant to the current research is the ability of collecting more information (feature of datasets) with IIT compared to conventional hardness measurement. In this section, the experimental setup for performing IIT on BM or WM of DP600, DP800, DP1000 and S690QL is firstly explained, and then the optical sensors used to examine the deformed surface of the indented specimens are shown. Then, the numerical model of IIT is presented and the boundary conditions that need to be considered in the numerical simulation are discussed.

4.1.1. Performing of Instrumented Indentation Test

The indentation tests were performed with the ZHU2.5/Z2.5 testing machine (ZwickRoell, Kennesaw, GA, USA) equipped with a hardness measurement head and fully automatic X/Y table. A digital displacement measuring system using a glass scale with a resolution of 0.02 µm, a force sensor that electromechanically measures the applied forces between 5 and 2500 N, and a replaceable indenter are installed in the hardness measuring head. An optical unit which consists of a light microscope with four lenses which has a charge coupled device camera and a sliding carrier is additionally a part of IIT machine and located next to the hardness measurement head. The sliding carrier allows adjustment of the specimen location between the

microscope and the loading assembly by simply moving the unit, thus ensuring that the specimen under test does not move. Figure 4.1 shows ZwickRoell ZHU 2.5 indentation testing machine with its different components.

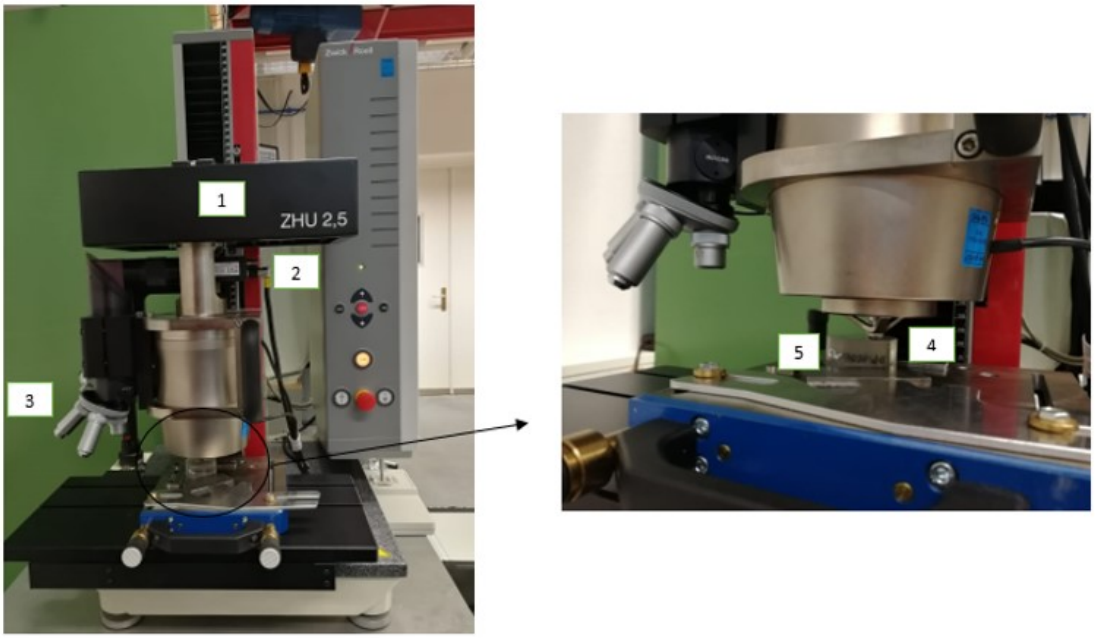

Figure 4.1 ZwickRoell ZHU 2.5 indentation testing machine with its components: 1) loading unit 2) displacement measurement system 3) light microscope 4) indenter and 5) test specimen

All tests were carried out using a spherical diamond indenter from ZwickRoell with a tip radius of 0.2 mm on high strength dual phase steels DP600, DP800, DP1000 and fine-grained structural steel S690QL. The IIT was conducted on the BM, WM of RSW and LBW as well as the HAZ with maximum load of 120 N and the applied position-controlled load rate of 0.05 mm/min for all steel grades to achieve the indentation depth of 8-12% according to the nominal indenter radius of 0.2 mm. After reaching the maximum load and observing a waiting time of 2 s, the force on the specimen was removed at the unloading rate 0.05 mm/min. The test results are automatically summarized in graphical and tabular form for further statistical evaluation by using fully automatic control software called testXpert implemented in ZwickRoell ZHU 2.5 testing machine.

Special effort must be made on control of surface roughness to minimize the influence of the finishing process, such as grinding, over the quality of the indented surface of the specimens and thus reduce the potential uncertainty in the measurement of the force-indentation depth curve. Surface roughness accounts for the inaccuracy of the

contact zone at very low indentation depth. The uncertainty of the penetration depth is proportional to the average arithmetic mean of surface roughness. The measured indentation depth should be at least 20 times greater than the arithmetic mean of the surface roughness to limit its contribution on the uncertainty of the indentation depth measurement to a maximum of 5% [69]. It means that by inserting a spherical indenter with the maximum test load of 120 N on the steel specimens, the surface should have an arithmetic mean roughness (Ra) of 1.6 to 3.2 µm. In addition, the slope of the specimen surface must be taken into account during the IIT. The deviation between the specimen surface from the normal axis of force application must be less than 1° as mentioned in ISO 14577-1:2002 [69]. The specimen should rest firmly on an inelastic support to avoid movement during the test. The thickness of the specimen must be at least ten times the indentation depth or three times the diameter of the indented zone to minimize the influence of the support on the measurement findings. The investigated sample surface was mechanically ground, as the required surface roughness for performing of IIT at macroscale, which is conducted in the current project, should be between 1.6 and 3.2 µm. Further mechanical or chemical process such as polishing to reduce the surface roughness was not required. The samples of DP1000, DP800, DP600 and S690QL for performing of IIT, as shown in Figure 4.2, are embedded in resin to make them convenient to hold during the sample preparation (grinding) and easier to fix by carrying out the test.

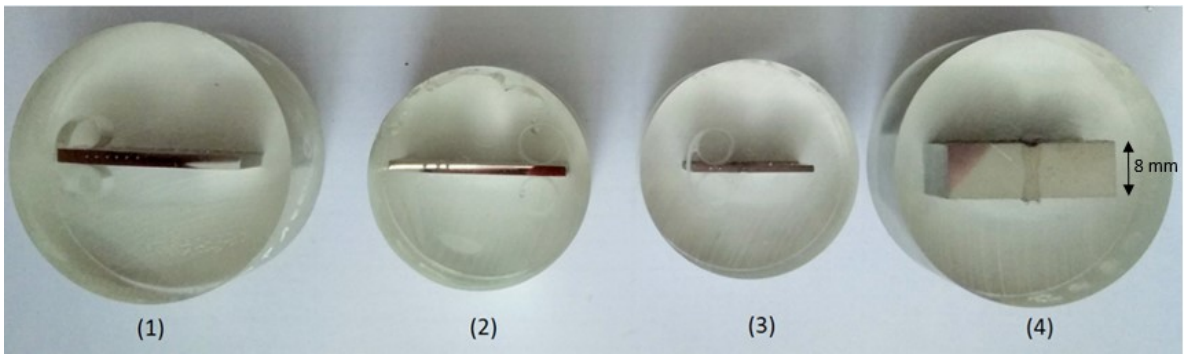

Figure 4.2 Samples of AHSSs for performing of IIT 1)DP1000; 2)DP800; 3)DP600 and 4)S690QL

4.1.2. Analysis of the Penetration Profile

Alicona Infinite Focus as an optical microscope with a high resolution 3D measurement system, which combines all the functionalities of a coordinate and

surface measuring machine, is used in the current work to examine the surface of samples after conducting of IIT. A semi-transparent mirror is used in Alicona system to direct and focus the light through the objective on the component. The light reflected from the specimen surface returns to the optical system and is directed onto the active surface to reproduce an image with information about color and dimension of sample. The signal processing unit scans only those parts of the image on which the light beam is focused to reconstruct and combine them into a final 3D image [122].

The microscope with movement range of 100x100×100 mm^3 is equipped with a motorized nosepiece and a set of five different types of special microscopic objectives which have different magnification scales from 2.5x to 100x and various working areas. The CFI LU Plan EPI ELWD objective with magnification scale of 20x, working area of 13 mm and field view of 0.286x0.218 mm^2 was used for determination of the indented profile in surface of all samples studied in this work.

In addition to the Alicona system, the deformation on the surface of the indented specimens was measured using the light microscope of ZwickRoell ZHU 2.5 indentation machine with a magnification scale of 40x, horizontal and vertical view fields of 220 and 165 µm, respectively, and the resolution of 0.2 µm per pixel.

4.1.3. Numerical Simulation of Indentation Test

A two-dimensional numerical simulation model of the IIT was established using eight-node elements with geometry and dimensions as shown in Figure 4.3. The PLANE183 element type with a quadratic displacement behavior and two degrees of freedom at each node was chosen for the simulation model, allowing the modeling of irregular meshes. A flexible-flexible contact pair was defined between the indenter tip (target) and the steel specimen (contact). Furthermore, the Lagrange method was used as the contact algorithm, which uses an iterative series of error updates to calculate the error factor to determine the Lagrange multiplier. The model was constructed axisymmetric to the y-axis, and the bottom of the sample was fixed. In the axis of symmetry, the edges are then fixed with a symmetry constraint and movement in the x-direction is prevented. In this way, it can be ensured that the indenter penetrates only vertically and the deformation is symmetrical. In the first loading step, the force (F) in the order of 120 N was applied uniformly and gradually

to the upper edge nodes of the quarter circle of the indenter and then removed again in the second loading phase. The friction coefficient is defined as 0.15 according to reference [123] for the contact between the diamond indentor with a linear elastic material behavior and the Young's modulus of 1140 GPa and Poisson's ratio of 0.07 and the steel specimen with the nonlinear isotropic strain hardening material model with the Equation (2.1).

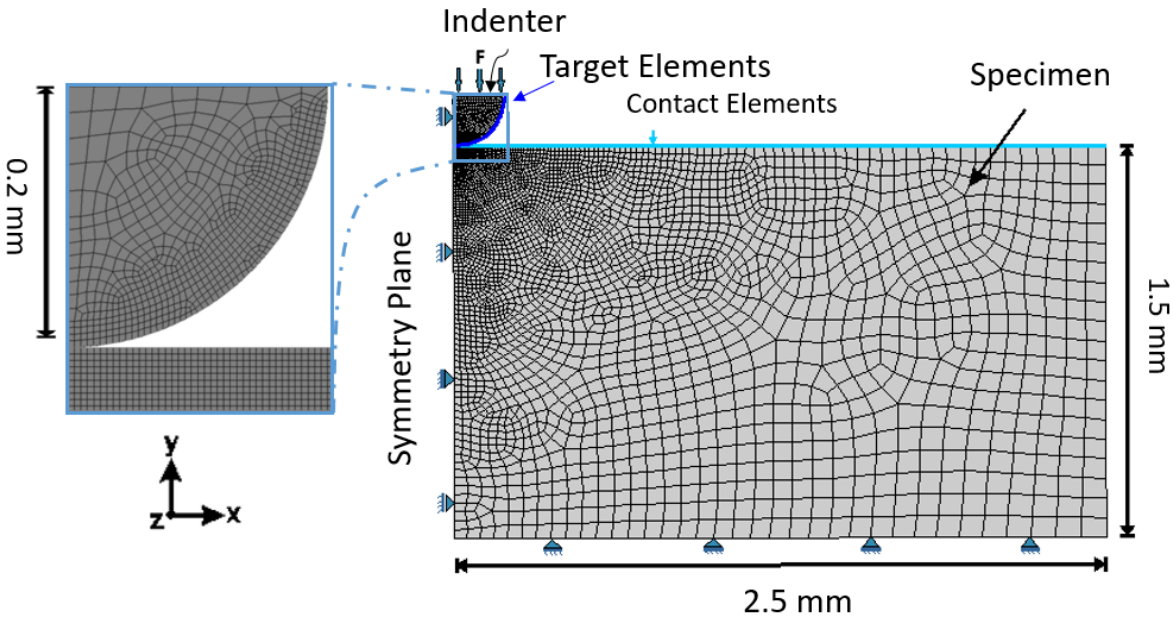

Figure 4.3 Geometry of the numerical simulation model of the instrumented indentation test

The mesh sensitivity analysis was performed for the DP1000 BM with a refinement of the mesh size especially in the contact area where the maximum deformation of the steel specimens occurs. Using different mesh sizes alters the calculation of the indentation depth at maximum load which is chosen as an indicator for the evaluation of the simulation model accuracy. As seen in Table 4.1, the difference between the indentation depth at 1 and 5 µm mesh size is less than 1%, although the simulation model with finer mesh size is more than 3 times computationally more expensive than a model with coarser mesh. Since using a coarser mesh size does not significantly change the accuracy and drastically reduces the computation time, especially in this case where the simulation model has to be run several hundred times to generate the training datasets of the ANN, a mesh size of 5.7 µm in the area of contact between the indenter and the sample and 18 µm in the rest of the model was chosen. It was noticed as well that the calculation time for softer material such as DP600 BM becomes much longer as more deformation occurs and thus the computation time rises.

Table 4.1 Mesh sensitivity analysis and variation of indentation depth for numerical simulation model of IIT by using material model parameters of DP1000 BM for indented specimen

Mesh size of contact elements in µm	Number of elements	Indentation depth at F_{max} in µm
20	3391	32,11
5	6417	31,33
2	7740	31,15
1	8882	31,10

The displacement and the load of a node in the middle of the contact between the indenter and the specimen were investigated to determine the load-indentation depth curve. Furthermore, the indenter's penetration profile was simulated by calculating the displacements of the nodes on the surface of the sample after applying the load. The material parameters for welded DP600, DP1000 and S690QL could be determined by inverse simulation. For this approach, in the first step, the indentation test was simulated with random values of the material model parameters as given in Equation (2.1). Subsequently, the simulation model was iteratively run with different material model parameters until a minimum mean squared error between the simulation and the experimental results of the indentation tests was obtained. In fact, such an approach can benefit from an optimization routines if additional information, such as the elastic modulus and yield strength, can be estimated in advance [70]. Using this approach, the difference between the simulation results and the experimental data was minimal, and therefore, the material parameters for WM of LBW and the HAZ of RSW were obtained. Furthermore, numerical simulations were carried out with the material parameters for the BM and WM of RSW, as already determined from the tensile tests, to validate the results.

4.2. Results and Discussion

In this section, the experimental results from the IIT such as force-indentation depth curves of the target microstructure and the profile from the surface of the indented samples taken by the Alicona system and light microscopy are presented first. Then, the outputs of the numerical simulation model of IIT are introduced and the accuracy of the model is discussed based on the experimental data. Finally, the material model parameters of the weld zones of AHSSs, which were not determined in Chapter 3,

are calculated by performing the inverse simulation with the validated numerical model of IIT.

4.2.1. Force-Indentation Depth Curve

As mentioned in section "4.1. Methodology" of IIT, the indentation test was performed on DP600 in different zones such as BM and WM of RSW and LBW, DP800 in BM, DP1000 in BM and WM of RSW and LBW, as well as HAZ of RSW, and finally S690QL in BM as well as HAZ and WM of LBW. The aim was to perform the indentation test on all possible different zones of a welded joint, which is welded with different welding technologies. Nevertheless, the size of HAZ in LBW or RSW of DP600 and DP1000 was small so that it was not possible to perform the IIT in this area. For example, the HAZ in the LBW of DP1000 is less than 0.5 mm in width on each side, which makes it extremely difficult to perform IIT with an indenter tip radius of 0.2 mm and increases the test result uncertainty. However, reducing the indenter radius results in the need to increase the quality of the surface roughness and additionally increases the test uncertainty since the indenter may be pushed in different grains of the target microstructure, which have different properties and react or resist variously to the movement of the indenter. Thus, it was objected to perform the test on the welding zone with the small width to enhance the robustness and reliability of the test results.

The result of performing IIT on BM of DP800 and different weld zones of S690QL from LBW is shown in Figure 4.4 as a plot of force indentation depth (penetration) curve. The indentation test was repeated at least three times on each target microstructure to ensure the accuracy of the test procedure. Then, the average result of the tests were calculated and plotted in each figure. The results of performing IIT on DP800 BM three times and their average are shown in Figure 4.4, indicating that all curves follow a similar trend and the results are repeatable and robust enough. As expected, the indentation depth at the maximum force of the IIT procedure varies for different microstructures depending on the hardness and strength of the material. For example, the WM of S690QL resulting from LBW has the highest hardness value (more than 400 HV1) compared to other investigated zones in Figure 4.4, consequently, exhibits the lowest indentation depth. The hardness of S690QL in HAZ is greater than BM but smaller than WM, therefore it is located between these two

curves. On the other hand, the load was gradually removed after reaching the maximum level or the highest value of indentation depth. After the load is completely removed from the surface of the specimen, the material preserves the elastic deformation, but the plastic strain is left below the indented surface. The area between the unloading path and the vertical line (parallel to the y-axis) starting from the maximum force and the x-axis (penetration depth) determines the elastic work, which depends on the elastic modulus and yield strength of the investigated specimens [124]. Furthermore, there is a direct relationship between the ratio of elastic work to total work (elastic and plastic work) and the material properties and the hardness magnitude of the specimens [125]. Since all the investigated samples belong to the BM or WM of the AHSSs, the differences between the elastic modules of the investigated materials are negligible. Thus, the variation in the slope of the unloading path for the different materials results from the different magnitude of the yield strength and plastic behavior, as well as the variation in the value of the measured hardness in the studied specimens.

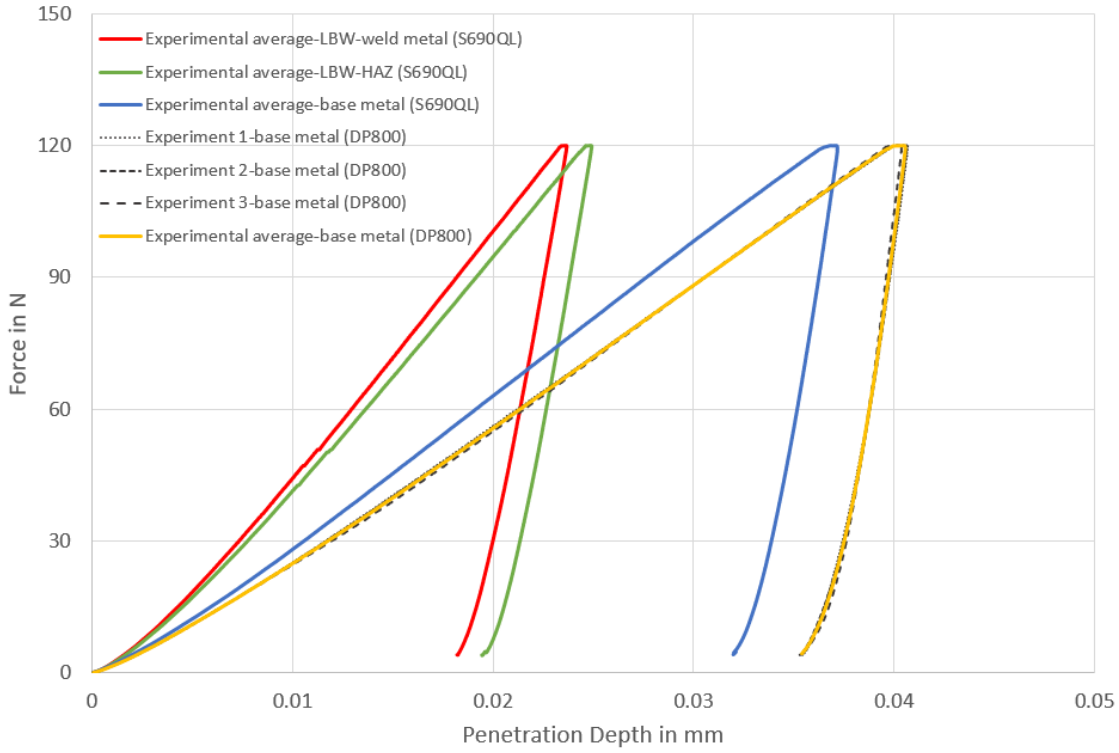

Figure 4.4 Force-Indentation (Penetration) depth curve for DP800 BM and S690QL in different zones of LBW joints such as BM, HAZ and WM

As shown in Figures 4.5 and 4.6, the experimental indentation depth in the WM of DP600 and DP1000 resulting from RSW is smaller than other zones. Similarly, the

WM indentation depth from LBW remains far from the indentation depth on BM and close to the WM from RSW. The results show that the penetration depth of HAZ resulting from the RSW of DP1000 is about 0.035 mm, which is the highest value compared to other penetration depths. It occurs due to softer microstructure of HAZ from RSW of DP1000, as seen in Figure 3.23, in comparison to other zones such as WM or BM. Furthermore, a comparison between the indentation depth on BM of DP600 and DP1000 shows that the resistance of DP1000 to deformation due to the penetration of an indenter is much higher than that of DP600.

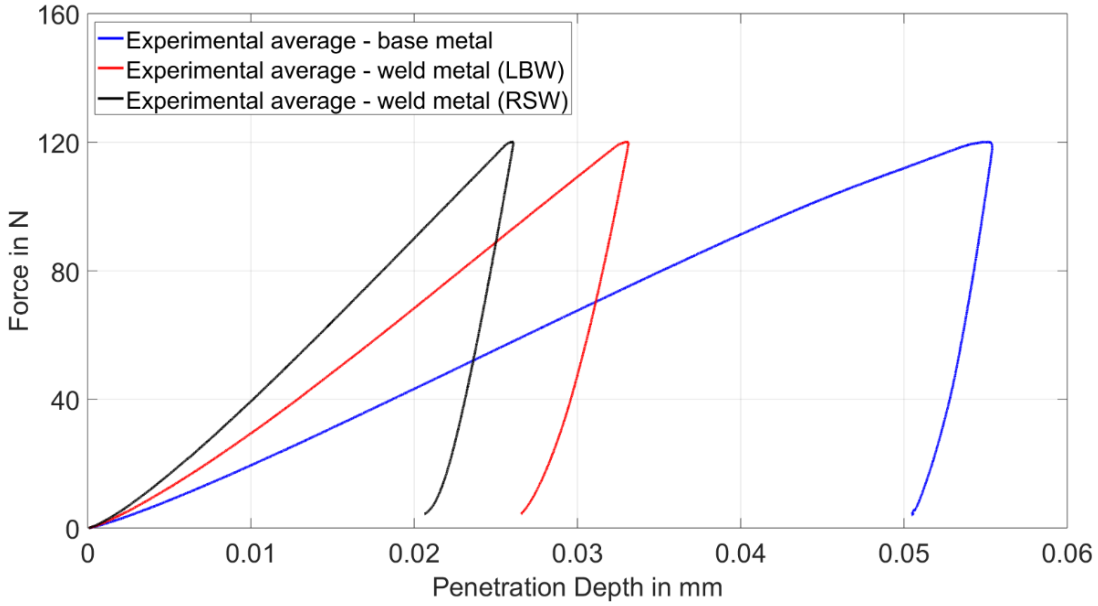

Figure 4.5 Force-Indentation (Penetration) depth curve for DP600 with different microstructure type such as BM, WM of RSW and LBW

The differences between the indentation depth of WM from LBW and RSW on both DP600 and DP1000, as seen in Figures 4.5 and 4.6, can be justified by evaluation of the measured Vickers hardness value on these zones, as shown in Figure 3.23. Suppose the hardness value in a particular zone is higher than the other zones. In that case, the penetration depth should be proportionally lower. Both WM contains the martensitic microstructure, however, the hardness value in WM of RSW for both steel types is higher than that in WM of LBW due to faster cooling time in RSW compared to LBW as measured and presented in Figures 3.16 and 3.17. According to Time Temperature Transformation (TTT) diagrams of DP-steels [99], such a short cooling time can lead to a martensitic microstructure, however, the hardness value increases significantly by raising the cooling time rate after welding.

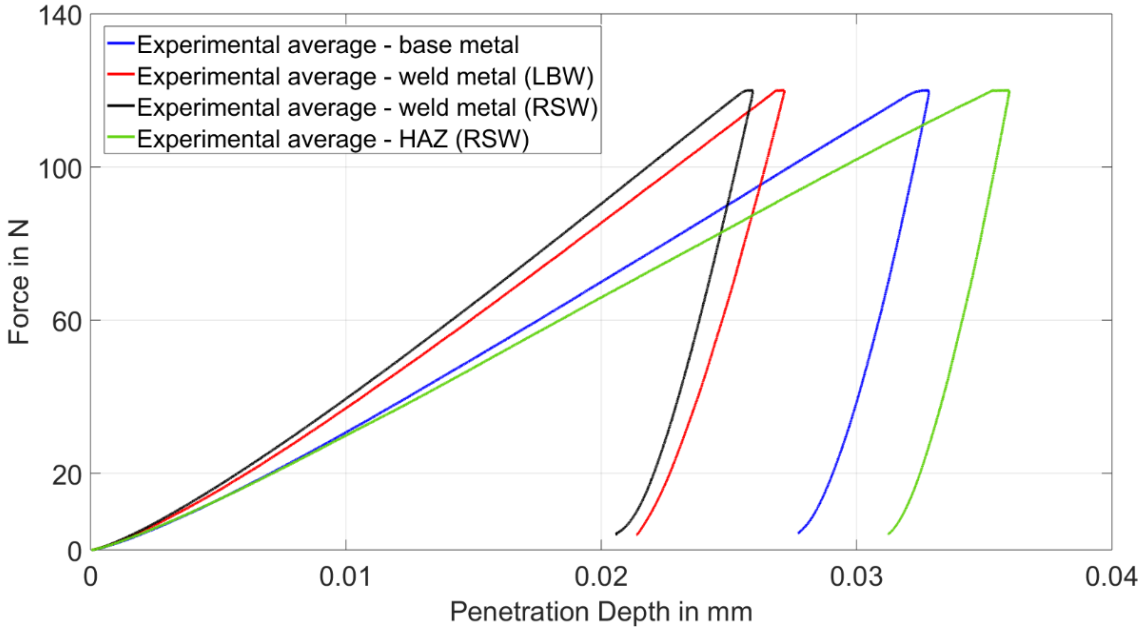

Figure 4.6 Force-Indentation (Penetration) depth curve for DP1000 with different microstructure type such as BM, WM of RSW and LBW as well as the HAZ of RSW

4.2.2. Profile of Deformed Surface

The surface of the indented samples has been investigated with a high-resolution 3D measurement system and a light microscopy as explained in section “4.1.2. Analysis of the Penetration Profile” to analyze the effect of indentation test on the surface of specimens after performing of the IIT. For instance, Figure 4.7 (a) shows the isometric 3D projection of the deformed surface of the D1000 WM produced from RSW after conducting of IIT, with color scale measurement next to it. Figure 4.7 (b) is similar to Figure 4.7 (a), except that the top view is illustrated. Furthermore, Figure 4.7 (c) presents the location and position of the path on which the profile of the indented surface is measured, as shown in Figure 4.7 (d). The similar measurements have been performed on all the indented samples of AHSSs in both BM and WM and then the findings are summarized in form of the penetration depth-distance diagrams and presented in Figures 4.9, 4.10 and 4.11. Since a spherical indenter has been used to perform the IIT and the test material under the indenter is homogeneous, only one-half of the profile from the indented surface, which is shown in Figure 4.7 (d), has been presented in the further process of this work.

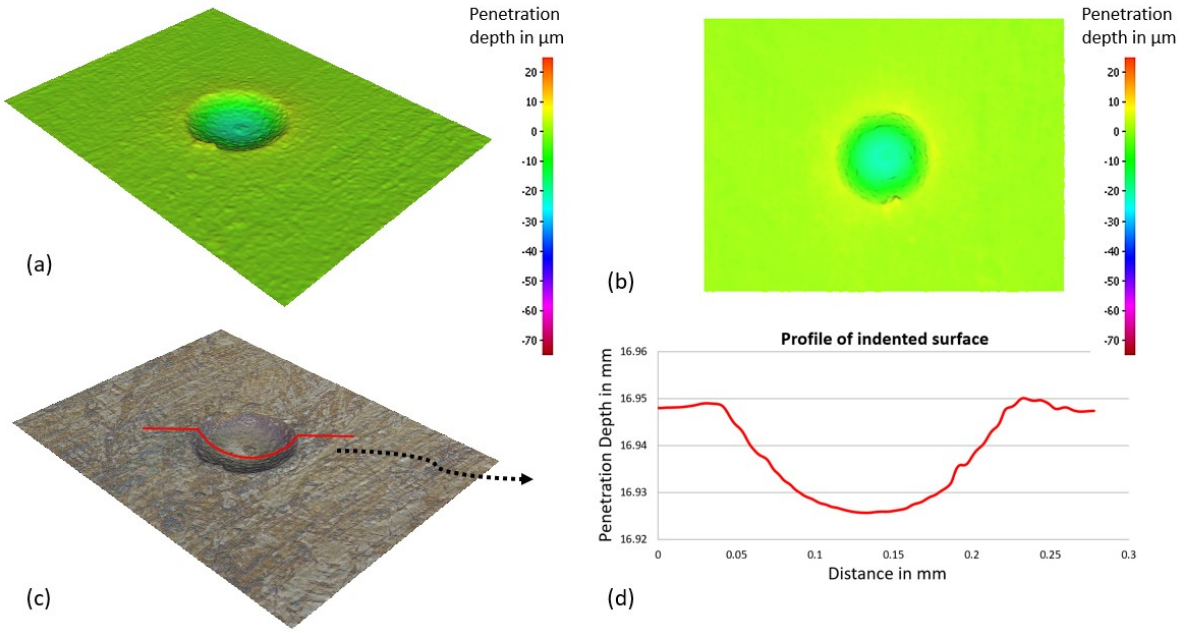

Figure 4.7 The deformed surface of the indented specimen produced from the WM of DP1000 with RSW, the measurement was performed with a high-resolution 3D measurement system (Alicona Infinite Focus) (a) 3D isometric projection of the indented surface (b) top view of the indented surface (c) 3D isometric projection of the indented surface with a red line to illustrate the path location of the profile of the indented surface (d) profile of the indented surface measured with the Alicona system from the path shown in (c)

Figure 4.8 (a) shows the top view of the indented surface of the DP1000 WM from RSW, measured with the Alicona system, without demonstration of the deformation measurement. Next to it, Figure 4.8 (b) shows the surface of the indented specimen taken with the light microscopy of the ZwickRoell ZHU 2.5 indentation testing machine. As seen in Figure 4.8 (b), the indentation results in a black hole whose size depends on the shape of the indenter and the sample type. The surrounding area is deformed and its shape and color has been changed after performing of the indentation. The data representing the deformation of the indented surface, shown in Figure 4.7 (b), Figure 4.7 (d), and Figure 4.8 (b), are later used in addition to the force indentation depth curves which are represented in section “4.2.1. Force-Indentation Depth Curve” to train the ANNs to characterize the mechanical properties of the welded AHSSs. However, throughout the rest of this section, the profile of the indented surface summarized in the form of penetration depth-distance curves for the indented specimens of S690QL, DP600, DP800 and DP1000 in various microstructure depending on the steel grades will be presented and discussed.

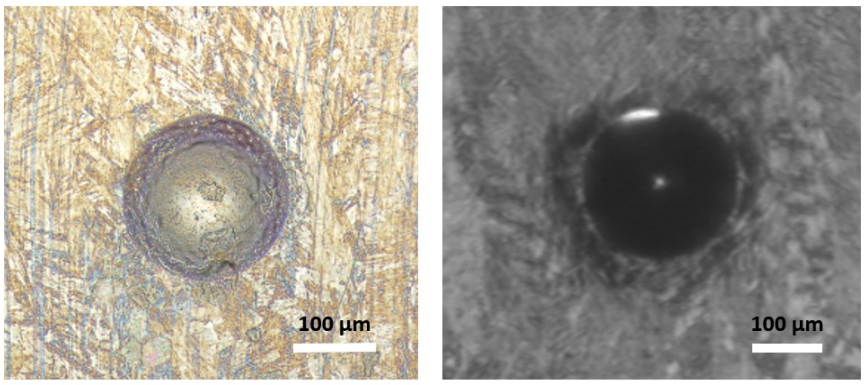

Figure 4.8 The deformed surface of the indented specimen produced from the WM of DP1000 with RSW (a) top view of the indented surface measured with Alicona system (b) top view of the indented surface measured with light microscopy of ZwickRoell ZHU 2.5 indentation testing machine

Figure 4.9 shows the profile of the indented surface based on the diagram shown in Figure 4.7 (d), except that it is only from the indentation center, which is a point with maximum value of indentation depth. The profile of the indented surface for some samples, such as S690QL WM from LBW, DP1000 WM from LBW, and DP1000 HAZ from RSW, were recorded twice and are shown in Figure 4.9 and Figure 4.11 to demonstrate the robustness and repeatability of the conducted measurement. As seen in the Figure 4.9, the indentation curve of S690QL WM from LBW in point 1 and 2 both follow the same course and show the similar indentation path. However, a small difference, which is less than 6 µm in the critical area, could result from the light reflection during the 3D measurement of the indented surface or the occurrence of the softer or harder microstructure. As expected, the indentation depth of DP800 BM is the deepest compared to the indentation depth of S690QL BM and WM, as it has the least yield strength among these three investigated microstructures. Moreover, the indentation paths of S690QL BM and DP800 BM are parallel to each other, as both have approximately similar plastic behaviors, which are reflected in the magnitude of tensile strength and strain hardening exponent, as shown in Table 3.7 for the smooth specimens of DP800 and S690QL. Furthermore, the WM of S690QL has the lowest penetration depth thanks to its strength and the presence of a martensitic microstructure. Another phenomenon observed in Figure 4.9 is the occurrence of pile up only for the BM of S690QL and DP800. It seems that the appearance of pile up or sink in is directly related to the strength and plastic behavior of the investigated material. However, this phenomenon will be discussed in details later.

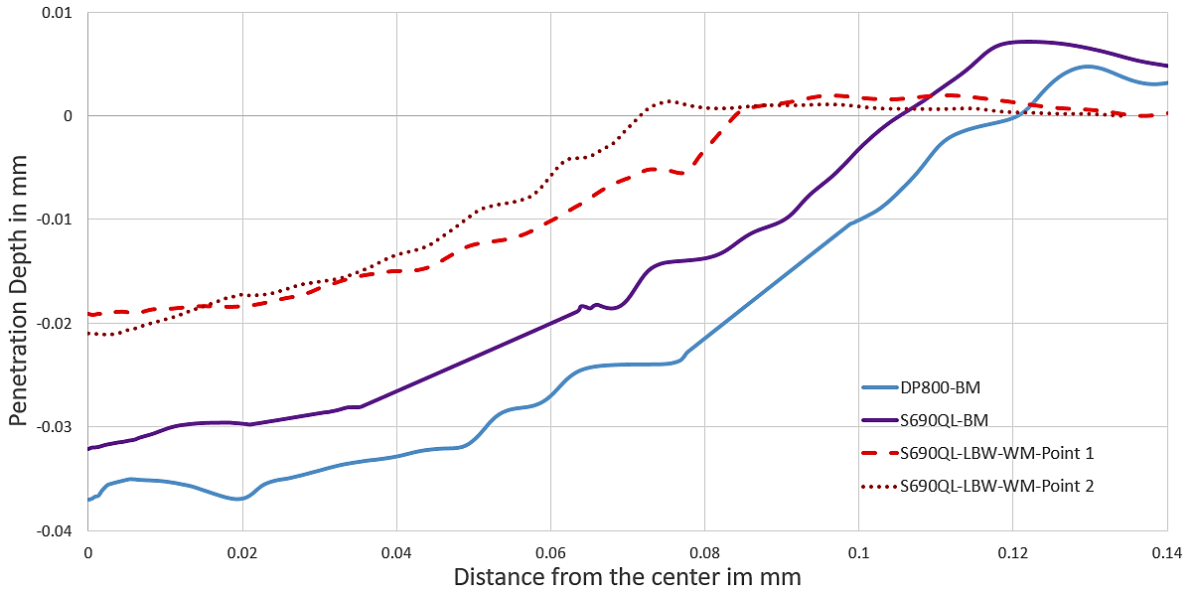

Figure 4.9 Profile of the indented surface from the indentation center (the point with maximum value of indentation depth) of DP800 BM, S690QL BM and WM of S690QL from LBW repeated twice (point 1 and point 2)

Figure 4.10 shows the indentation profile of DP600 specimens in different areas of welded zones such as BM and WM from RSW and LBW. The indentation profile of WM from both welding technologies, e.g. LBW and RSW, is close to each other due to the martensitic microstructure, though a slight difference in the order of less than 10 µm is observed in the center of the indentation. A similar pattern was observed in the indentation depth diagram of DP600 steel, as shown in Figure 4.5, such that the indentation depth of DP600 WM from RSW is less than DP600 WM from LBW at maximum indentation force. As shown in Figure 4.10, no pile up is observed in the profile of the indented specimens from WM. On the other hand, the indentation profile of DP600 BM is larger than the indentation depth of DP600 WM considering that the former material is softer and its yield and tensile strengths are lower than those of WM. Another point that can be observed in Figure 4.10 is an unexpected leap in the penetration profile of DP600 BM in around 0.12 mm far from the penetration center. In addition, the penetration profile of DP600 BM is expected to show the pile up effect similar to BM of DP800 or S690QL. Both phenomena can be justified by inaccuracies and possible errors in image recognition and finally regeneration of indentation path in Alicona system due to light reflection from indented DP600 BM sample or implemented image recognition algorithms in optical system as observed in 3D isometric projection of the indented surface.

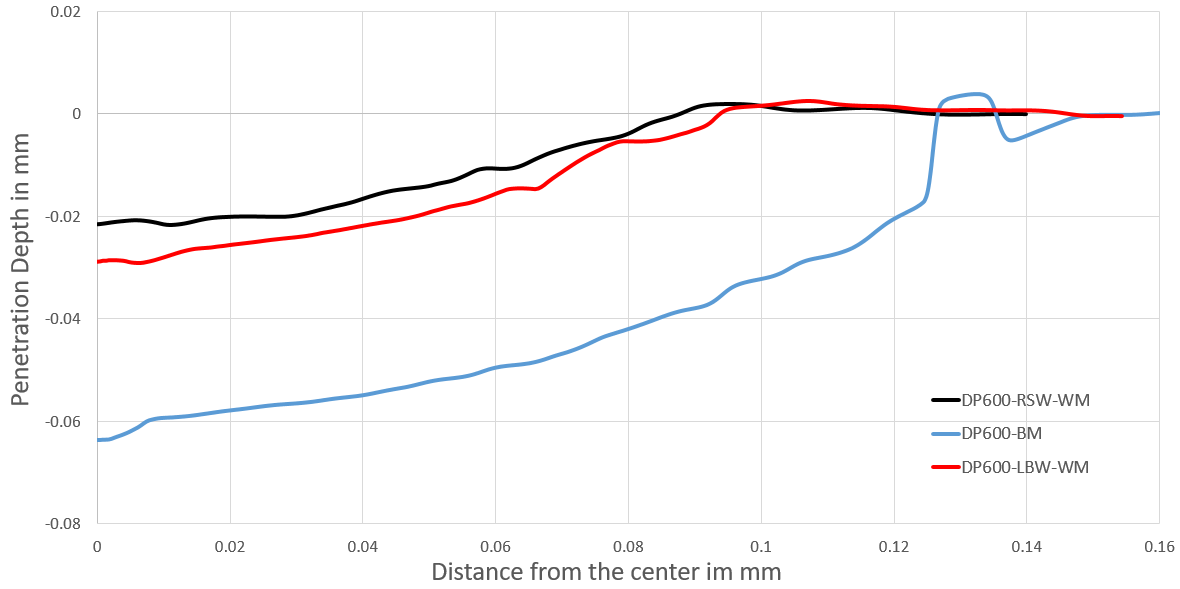

Figure 4.10 Profile of the indented surface from the indentation center (the point with the maximum value of the indentation depth) of DP600 BM, WM of DP600 from LBW and WM of DP600 from RSW

Figure 4.11 shows the deformation profile of DP1000 steel in BM, WM of LBW and RSW, and HAZ of RSW. The indentation profile of DP1000 from the HAZ of RSW and WM of LBW was recorded twice (point 1 and 2) to show the robustness and reliability of the measurement. Both recordings follow a similar pattern and agree together completely with a maximum difference of less than 4 µm in the area of largest deviation. Both WMs of RSW and LBW of DP1000 show the similar maximum penetration depth due to the similar martensitic microstructure, though a slight difference can be observed far from the penetration center and near the surface that is not affected by the penetration. The penetration path in the HAZ of DP1000 from RSW is deeper than the BM of DP1000 for both recorded routes. This phenomenon can be justified by considering the differences between the hardness measurement of the HAZ and the BM for DP1000, as shown in Figure 3.21 (a) and Figure 3.23 in the lines belonging to DP1000-RSW. As seen in the last two mentioned Figures, the hardness value in the HAZ of DP1000 from RSW is lower than BM of DP1000. Therefore, it is expected that the penetration depth of HAZ is larger than BM. In Figure 4.11, a slight pile up effect can be observed for all investigated materials, however, its magnitude is much smaller than the pile up size for the softer materials such as BM of DP800 or S690QL, which exceeded roughly 5 and 7 µm, respectively.

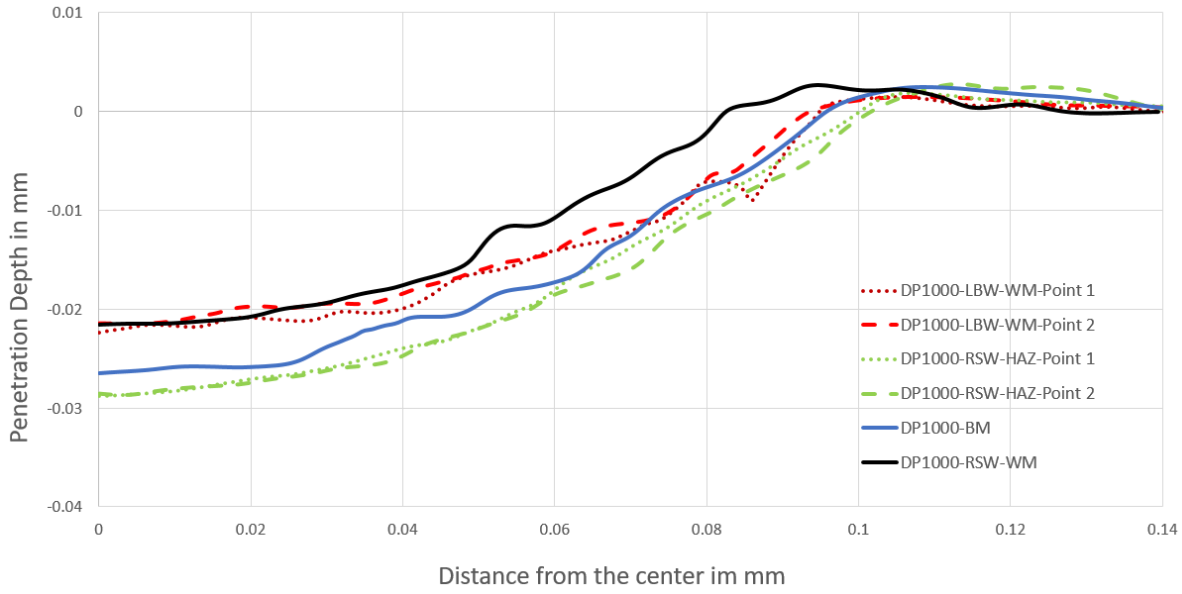

Figure 4.11 Profile of the indented surface from the indentation center (the point with the maximum value of the indentation depth) of DP1000 BM, WM of DP1000 from LBW repeated twice (point 1 and point 2), HAZ of DP1000 from RSW repeated twice (point 1 and point 2) and WM of DP1000 from RSW

4.2.3. Numerical Simulation of Indentation Test

The numerical simulation model of IIT, as explained in section "4.1.3. Numerical Simulation of Indentation Test" and shown in Figure 4.3, was performed with already determined material parameters of known steels, as demonstrated in Table 3.8 and Table 3.10. The calculated force-penetration depth curves and the profiles of the indented surface from the numerical simulation model were first compared with the experimental data as presented in Figure 4.12 and Figure 4.13, respectively, to validate the simulation model. Then, the validated model was used to perform the inverse analysis to calculate the material data of other weld zones that failed to be calculated in Chapter 3, such as WM of DP600, DP1000 and S690QL from LBW and HAZ of DP1000 from RSW and the results are shown in Table 4.2. Another goal of a validated simulation model of IIT is to generate a large volume of training datasets to later train the ANNs capable of calculating the mechanical properties of AHSSs in different welding zones.

Figure 4.12 compares the numerically and experimentally determined force-indentation depth curves to verify the simulation model. There is a strong agreement between the simulation and experimental results, especially when the penetration

depth is small. For instance, the agreement between the calculated and measured force-penetration depth curves for the sample DP1000 WM from RSW is significantly closer than the sample DP600 BM. Another observation is the deviation between the calculated and measured unloading curves for all the investigated samples, which is also reported in other research works such as [126] [127].

In order to achieve a stronger agreement between the results of the numerical simulation and the experimental analysis for the determination of the force-indentation depth curves, it is necessary to use a material model capable of calculating the strain hardening exponents as a function of the indentation test outputs [128] [129] [130]. The reason for this is that there is a positive correlation between the total work, including plastic and elastic work, resulting from the indentation test and the material properties, in particular the hardness of the substrate whose behavior is tightly comparable to the response of the specimens to the indentation test [125]. Another reason for the slight discrepancy between the numerical and experimental results could be due to the occurrence of creep because of the waiting time after loading and before unloading while performing the indentation test, which can be seen as a small flat line at maximum force in each force-indentation depth curves in Figure 4.12 [131] [132]. Another point to consider is the effect of contact stiffness as an indicator to generalize the force-displacement behavior between two contacting surfaces, which can be calculated as the slope of the tangent line in the region near the initial point of the unloading curves [133]. The contact stiffness depends on the geometry of the contact area, such as plastic and maximum indentation depth and surface roughness indicators, and its change can vary the slope of the unloading path resulting from the simulation model [80].

In summary, the current work presents a simulation model of IIT with strong agreement between the simulation and experimental results, especially for the material with high yield strength and measured hardness, whose investigation is the main objective of this current research work. In addition, more complex material models based on the indentation test and creep behavior can improve the accuracy of the simulation model for softer materials. However, the goal of training the ANNs in the current work is to obtain the material model parameters from a quasi-static tensile test, not to determine the parameters of a creep or indentation test based material model.

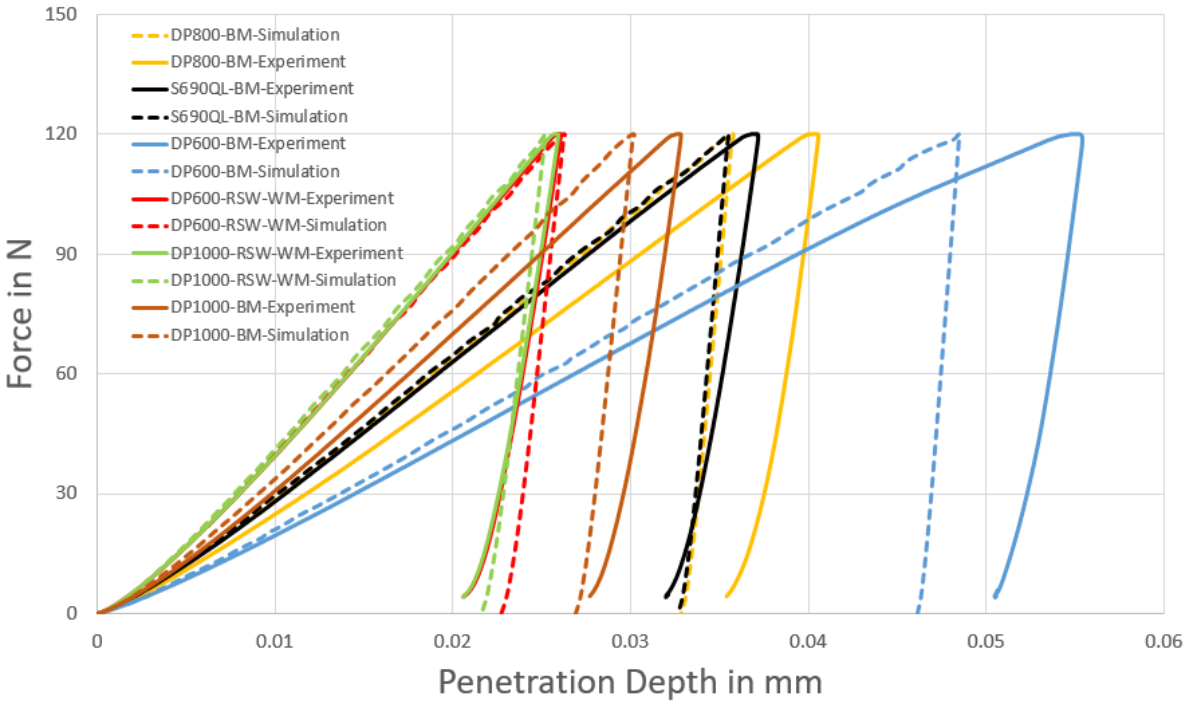

Figure 4.12 The comparison between the numerically calculated and the experimentally measured Force-Indentation (Penetration) depth curve for the specimens with the known material parameters to validate the numerical simulation model of IIT

Figure 4.13 compares the numerically calculated and the experimentally measured profiles of the indented specimen surface. The similar simulation model as used for the calculation of the Force-Indentation depth curves from Figure 4.12 and as explained in section "4.1.3 Numerical simulation of the indentation test" was used here. The only difference between the curves from the numerical work in Figure 4.12 and Figure 4.13 is that the indenter displacement was recorded and shown in Figure 4.12, however, the profile of the indented surface after performing of the indentation test in the simulation model was shown in Figure 4.13.

The first point that can be observed is the differences between the experimentally measured maximum indentation depth in Figure 4.12 and Figure 4.13. For instance, the maximum deviations between the maximum indentation depth in both figures are less than 9 and 7 µm for DP600 BM and DP1000 BM, respectively. For other investigated materials, the differences between the experimentally measured maximum penetration depth from Figure 4.12 and Figure 4.13 are less than 5 µm. The reason for recording different indentation depth values is that two different measuring devices were used to record the indentation depth in Figure 4.12 and Figure 4.13. The experimental data in Figure 4.12 is generated by the instrumented

indentation testing machine based on the movement of the indenter, in contrast to the experimental graphs in Figure 4.13, which are collected by inspecting the surface of the indented specimens with the 3D optical microscope, which can provide different information.

Furthermore, the indentation depths of both graphs can be expected to differ slightly because each measuring equipment has its own measurement error tolerance. For example, the error in the measured indentation depth from the instrumented indentation testing machine may come from the non-zero compliance of the test frame, which results in the movement of both indenters and the test frame and changes the original force-indentation depth curve [134]. On the other hand, the accuracy of the measured parameters by Alicona system can be affected due to the illumination direction and the position of the sample with different geometry to the axis of the light polarizer, as well as the variation of the focus of the microscope lens, which can ultimately have an impact on the measured profile of the indented surface [135].

As seen in Figure 4.13, there is a strong agreement between the simulation and experimental data describing the profile of the indented surface, especially for material with higher magnitude of yield strength and hardness value. For example, the differences between the numerically and experimentally determined indentation depth in the center of the indentation (the point with the maximum value of the indentation depth) are 15 and 1.5 µm for the BM of DP600 and DP800, respectively. The reason for the slight discrepancy between the simulation and experimental results has already been described in details in the explanation of Figures 4.10 and 4.12 and will not be recapitulated here. Moreover, the simulation model must be used later to calculate the material parameters of weld zones from the RSW and LBW, which have higher strength and hardness compared to the corresponding BM, and the presented numerical model works perfectly well for such a material.

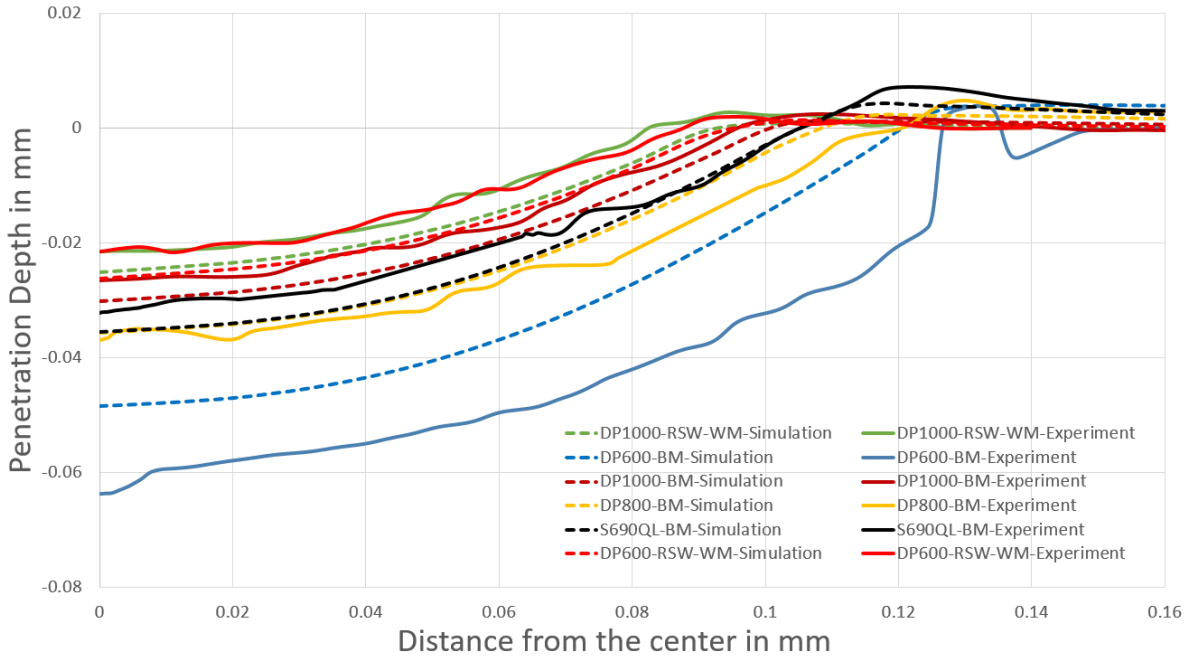

Figure 4.13 The comparison between the numerically calculated and the experimentally measured profiles of the indented sample from the indentation center (the point with the maximum value of the indentation depth) for the specimens with the known material parameters to validate the numerical simulation model of IIT

Another phenomenon observed in the indentation surface profile of the specimens in both experimental and simulation work is the occurrence of the pile-up effect. In order to get a better overview and discuss about it in details, the indentation profile of three DP-steels in the base material such as DP600, DP800 and DP1000, which have similar martensitic and ferritic microstructure, is compared. DP600 has the lowest strength compared to the other studied DP steels in this work, as shown in Table 3.7 and Table 3.8. On the other hand, it was reported that the martensite content of DP600, DP800 and DP1000 is 0.18, 0.25 and 0.48, respectively, and the rest of the microstructure is ferritic, with grain sizes of 8.4, 5.7 and 3.8 µm, accordingly [136]. Similarly, both simulation and experiment show that the pile-up size of DP600 is larger than DP800, and similarly DP800 is bigger than DP1000. On the other hand, it has been shown that there is a direct relationship between the pile-up magnitude and the grain size in a certain interval [137]. There is also a dependency between the grain size and the strength of a steel structure based on the Hall-Petch law [138]. It can therefore be concluded that DP600 experiences a larger pile-up due to its larger grain size and consequently lower strength compared to the other investigated steels.

From the numerical simulation point of view, the magnitude of the pile-up increases as the exponential saturation rate (b) and the difference between the yield strength and the saturation stress (R_∞) decrease. Therefore, the magnitude of the calculated pile-up in DP600 BM is higher than that in DP1000 BM. This leads to a more disparity for the numerically calculated indentation depth for the BM of DP600 compared to the DP1000 BM or WMs of other steels. Furthermore, the accuracy of the IIT simulation model proposed in this work can be revalidated as it shows exactly the similar flow in computing the magnitude of the pile-up.

The validated numerical simulation model of IIT was employed to calculate the mechanical properties of other weld zones, which could not be determined in Chapter 3, by using the inverse analysis. As explained in section “4.1.3. Numerical Simulation of Indentation Test” the unknown material model parameters of the investigated steels have been changed repeatedly in the simulation model of IIT to generate the force-indentation depth curves and profiles of the indented surface. Subsequently, experimental and simulation curves for each variation of the material model parameters are compared to find out the best parameters configuration that provides the smallest mean squared error between simulation and experiment. Normally, such an iterative procedure is numerically expensive and requires an optimization algorithm to improve the estimated parameters in each iteration. However, the objective of the present work is to calculate the material parameters of the WM of AHSSs, which have a martensitic microstructure and thus a high value of yield strength and low ductility. The prior knowledge about the unknown parameters that need to be calculated with the inverse simulation leads to a much lower numerical effort and does not require any further optimization algorithm.

Table 4.2 shows the material model parameters of WM of DP600, DP1000 and S690QL from LBW and HAZ of DP1000 from RSW. As expected, the yield strength of DP600 and DP1000 in WM has been increased after LBW, however, its magnitude is smaller than that of WM from RSW, as shown in Table 3.10. Similarly, Figure 3.23 shows that the Vickers hardness of DP600 and DP1000 WM from LBW is lower than that of WM from RSW, which consequently results in less strength. On the other hand, the parameters describing the isotropic strain hardening and ductility of the material remain approximately the same for the WM resulting from RSW or LBW for both DP600 and DP1000. Moreover, the material parameters of the HAZ from the RSW of

DP1000 show that their yield strength decreases significantly compared to the yield strength of DP1000 BM. This can be justified by the fact that the Vickers hardness in the HAZ of the RSW of DP1000 is lower than that of the BM and WM, as shown in Figure 3.23. In addition, the WM of S690QL from LBW has the highest value of yield strength compared to the other WMs and is also a least ductile steel among the other analyzed materials, as its Vickers hardness value is higher than that of any other investigated material, as shown in Figure 3.23.

Table 4.2 Determination of material parameters of different welding zones of AHSSs by inverse analysis with numerical simulation model of IIT

Material		$R_{p0.2}$ in MPa	R_0 in MPa	R_∞ in MPa	b
S690QL	LBW - WM	1000	200	400	100
DP600	LBW - WM	700	30	320	40
DP1000	RSW - HAZ	460	1500	343	50
	LBW - WM	800	175	437	96

Figure 4.14 compares the force-indentation depth curves between the experimental data and the simulation model results with the material data from Table 4.2. There is a strong correlation between the simulation and experimental data, especially in the loading phase of the indentation test for WM and HAZ of DP steels. As shown in the explanation of Figure 4.14, the discrepancy between the unloading paths from simulation and experimental work can have an impact on the calculation of elastic work and can be reduced by using a material model capable of predicting only the indentation path of AHSSs from both BM and WM as accurately as possible. However, Figure 4.14 shows that the obtained parameters in Table 4.2 are robust enough to be used for describing the stress-strain path of the investigated weld zones.

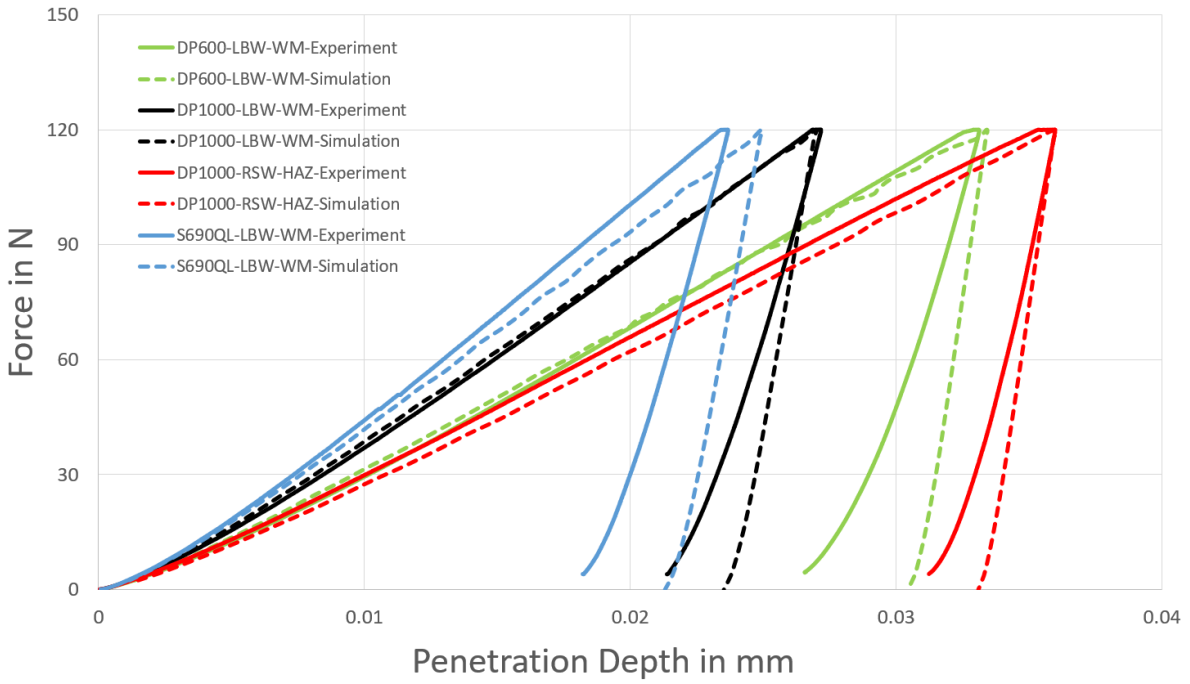

Figure 4.14 The comparison between the numerically calculated and experimentally measured Force-Indentation (Penetration) depth curve for the samples with the unknown material parameters, whose mechanical properties were determined by using the inverse numerical simulation model of IIT

In the same matter as Figure 4.14, Figure 4.15 compares the measured profiles of the indented surface with the Alicona system after performing the indentation test with the result of the simulation work for the materials whose parameters were calculated with the inverse analysis and presented in Table 4.2. As expected, the size of the pile-up for the WMs investigated in Figure 4.15 is much smaller than for the BMs of the DP steels, as shown in Figure 4.13, where the strength and hardness of the WMs resulting from the LBW are larger than the corresponding BMs of the welded steels in this work. Moreover, the strong correlation between the simulation results and the experimental analysis of the indented profile reconfirms the accuracy and correctness of the obtained material parameters in Table 4.2 and shows that they can be employed as test materials to evaluate and verify the accuracy of the trained ANNs in the current work, which is presented in the next chapter.

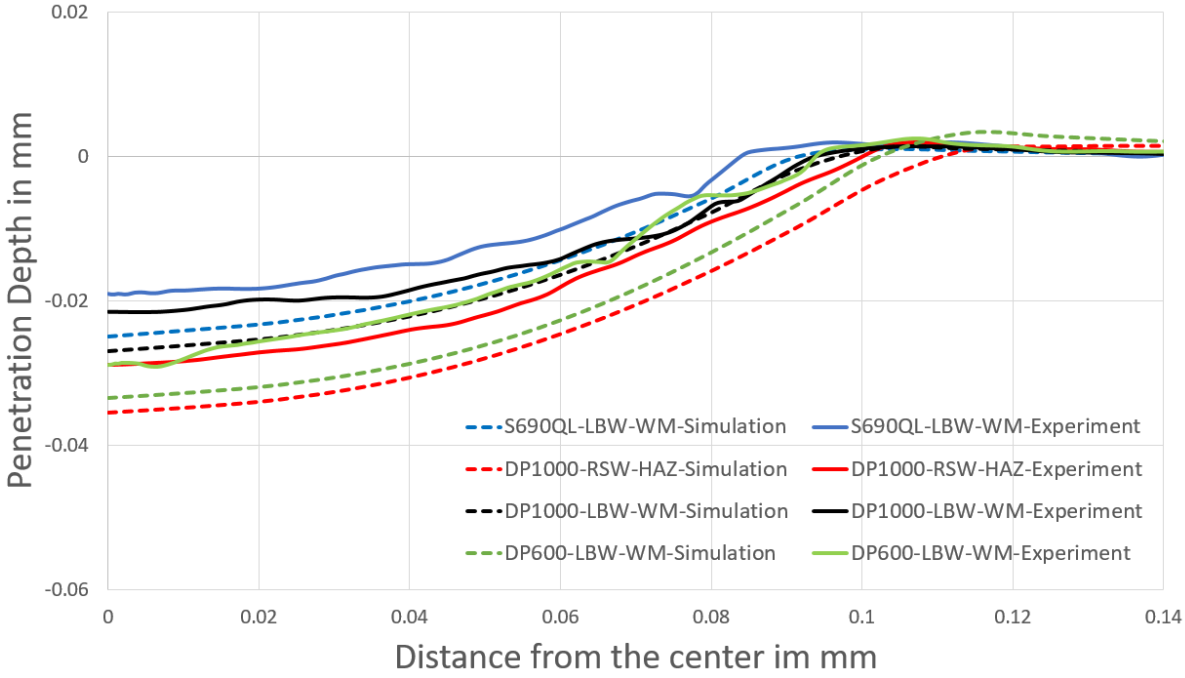

Figure 4.15 The comparison between the numerically calculated and experimentally measured profiles of the indented specimen from the indentation center (the point with the maximum value of the indentation depth) for the samples with the unknown material parameters, whose mechanical properties were determined by using the inverse numerical simulation model of IIT

To summarize, the IIT process was numerically simulated with a two-dimensional model and validated with the experimental results of BM and WM. This was then used to determine the material data of weld zones such as WM from LBW of DP steels and S690QL and HAZ of DP1000 from RSW using the inverse analysis. The need to have an accurate, simple and fast model which is able to perform the simulation of several hundred IITs in a short time to generate a large amount of data to train the ANNs leads to the setup of a two-dimensional symmetric numerical simulation model.

4.2.4. Methodology Validation

In the last step, in order to evaluate and revalidate the accuracy of the methodology used in the current chapter, the available data from the literature [7], as already shown in Figure 3.33, are used again and a further comparison based on the result of this chapter was performed as shown in Figure 4.16. As mentioned in the method validation of Chapter 3, the result of tensile test on HAZ of DP980 specimens with 1 and 3 mm thickness from thermomechanical simulation based on the work of Dancette [7] was first compared with the result of tensile test on the prepared

specimens of DP600 and DP1000 with 0.4 and 0.9 mm thickness, respectively, made from WM of RSW. Then, the stress-strain curves of WM of DP600 and DP1000 from LBW and HAZ of DP1000 from RSW are considered in Figure 4.16 to discuss about accuracy of the material characterization with inverse analysis based on the simulation model of IIT.

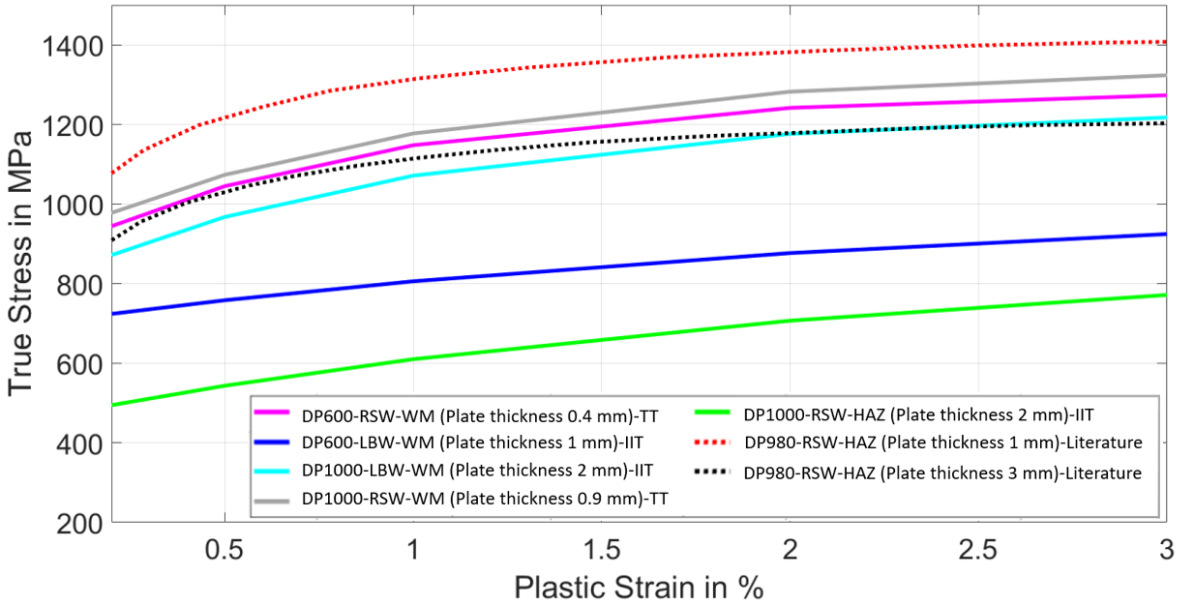

Figure 4.16 Comparison between the true stress-strain diagram of WM from LBW of DP600 and DP1000 plates and HAZ from RSW of DP1000 calculated from IIT with the result of stress-strain diagrams according to martensitic microstructure of HAZ DP980 of RSW from the literature [7] and the measured stress-strain curves from the tensile test (TT) on the notched specimens made of DP600 and DP1000 WM from RSW as shown in Figure 3.33

As explained in chapter three, the HAZ of DP980 plates are reproduced by heating them to 1200℃ and then cooling at different rates, where $t_{8/5}$ is less than 2s. According to TTT diagrams of DP-steels [99], such a high cooling rate leads to a martensitic microstructure which is similar to microstructure of WM. However, the investigated HAZ of RSW from DP1000 with inverse analysis of the IIT simulation model belongs to a zone far from the WM with the lowest measured hardness and, consequently, lower strength and lower level of the stress-strain diagram compared to the other weld zones. Furthermore, with the exception of the DP600 WM from LBW, the presented stress-strain diagrams of the WMs in Figure 4.16 show a slight deviation from each other and a similar behavior as expected based on the magnitude of the measured hardness as shown in Figure 3.23 which describing the reproduced microstructure after welding. Moreover, the stress-strain diagram of DP600 WM from LBW is lower than the stress-strain curves of other WMs but greater than the HAZ of DP1000 from

RSW. Figure 3.23 shows exactly the same behavior, as the hardness of DP600 WM from LBW is lower than the hardness of WMs, but greater than the hardness in the HAZ of DP1000 from RSW, especially in the region closer to the BM.

The comparison between the stress-strain diagrams from the literature [7] and the current research work further revalidate the results achieved based on the inverse analysis of the IIT simulation model. The slight differences between the stress-strain curves of the different investigated zones are expected since they were generated based on different measurement and calculation methods, welding procedures and belong to different welding zones. The results of the current and previous chapters are used in the next section to analyze the correctness and accuracy of the trained ANNs capable of computing the material model parameters.

5. Material Characterization with Artificial Neural Network

In the current chapter, the methodology of training the ANNs capable of calculating the mechanical properties of AHSSs in different weld zones is presented. As mentioned in the introduction, the ANNs in this research were trained with four independent datasets as shown in Figure 1.1. The steps to train the ANNs with the first two datasets, e.g., the force-penetration depth curves as well as the profile of the indented surface with their corresponding stress-strain diagrams, are explained in this chapter and their results and accuracy are discussed in details. The last two ANNs trained with the images of the indented surfaces are included in the appendix as further work.

First, various steps to train the ANNs such as generation of the large datasets, feature selection from the input datasets such as force-indentation depth diagrams and profile of the indented surfaces are described. Then, the architecture and parameters of the ANNs are discussed and explained in details. In the next section, the stress-strain diagrams resulting from the ANNs are evaluated and compared with the results obtained in the previous chapters to analyze the robustness and reliability of the trained ANNs and validate their outputs.

5.1. Methodology

The different steps to generate the large volume of datasets and then the workflow to train the ANNs with the datasets of the force indentation depth diagrams and the indented surface profiles are shown in Figure 5.1 and Figure 5.2, respectively. As shown on the left side of Figure 5.1, the parameters of the material model, as given in Equation 2.1, must be iteratively changed in the defined intervals as input data to

the simulation model of IIT, which was validated in chapter four, to generate the force indentation-depth curves and eventually provide a large volume of datasets for training the ANN. When enough datasets are generated, the training of the ANN can be started, as shown in the right side of Figure 5.1. In this step, the selected points from the force indentation depth diagrams generated by the FEM will become the input datasets of the ANN and the output will be the corresponding material model parameters, which will be iteratively changed at the defined intervals. When the training phase is complete, the accuracy of the trained ANN must be evaluated by comparing its outputs with the results of the test materials as determined in chapters three and four. If the accuracy of the outputs is not acceptable, the parameters or architecture of ANN must be changed or more datasets should be generated to increase the accuracy of trained ANN.

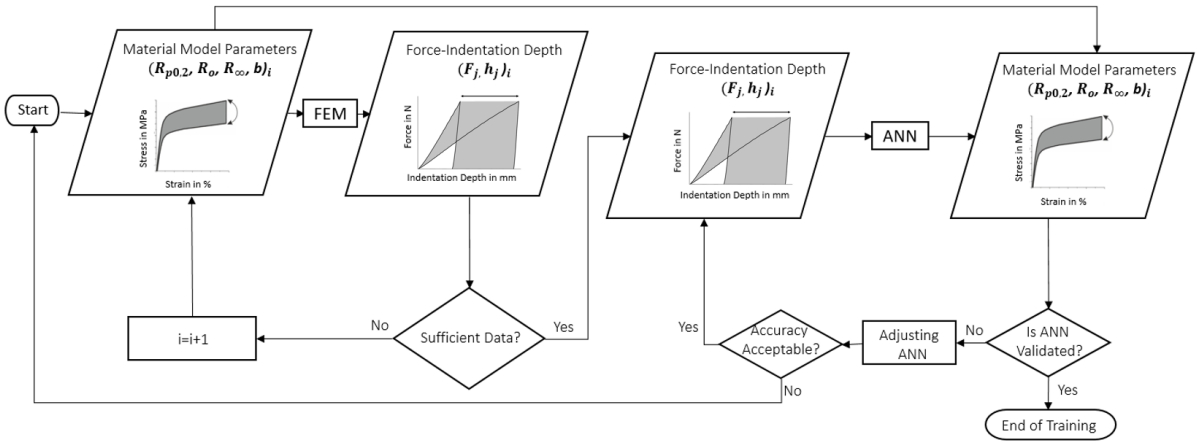

Figure 5.1 An overview of the methodology proposed in the present work to train the artificial neural network (ANN) to determine the material data by using Force-Indentation depth diagrams obtained from the instrumented indentation test. The training datasets were generated in a large volume by using the finite element method (FEM)

The methodology of training ANN with the second type of datasets, e.g. the profile of the indented surface as input data, is similar to the procedure of training ANN with the first type of datasets, e.g. the diagram of the force indentation depth as input data. However, as seen in Figure 5.2, the output of the simulation model of IIT will become the profile of the indented surface instead of the force indentation depth diagram. On the other hand, the input of the ANN is the output of the simulation model, e.g. the profile of the indented surface. The rest of the methodology remains similar as described in the explanation of Figure 5.1. In both Figure 5.1 and Figure 5.2, the subscript "i" refers to the number of datasets used to train the ANN. For example, if 100 force-indentation depth diagrams and their corresponding stress-strain curves

are provided to train the ANN, the final value of "i" is 100. In addition, the subscript "j" refers to each element of a dataset, e.g., if the input of a dataset contains 15 features, then the subscript "j" starts at 1 and ends at 15.

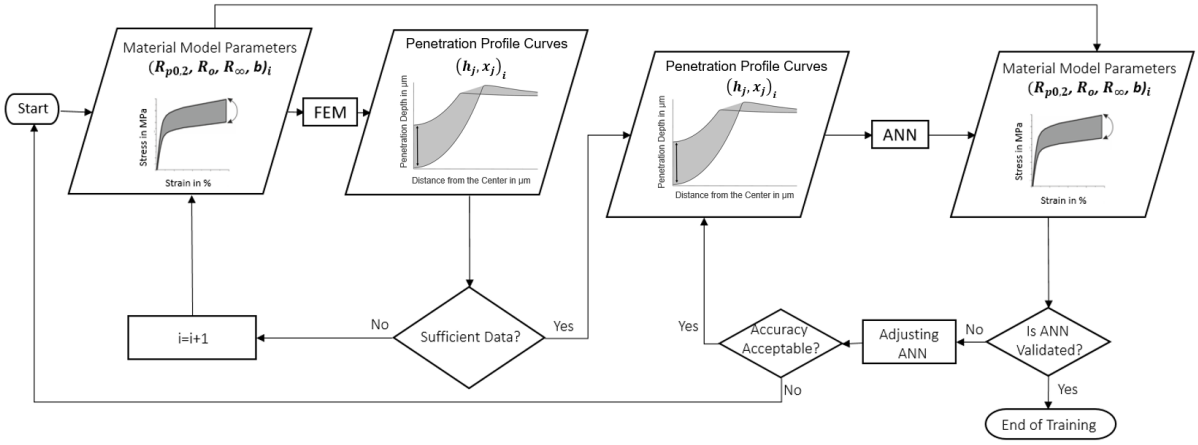

Figure 5.2 An overview of the methodology proposed in the present work to train the artificial neural network (ANN) to determine the material data by using the penetration profile curves obtained from the surface of the indented specimens. The training datasets were generated in a large volume by using the finite element method (FEM)

To begin with the methodology description of the ANN training, first the steps to generate the training datasets and the procedure to select the features from each dataset are explained. Then, the structure, architecture and parameters of the ANN are outlined.

5.1.1. Generation of Training Datasets

The parameters of Voce nonlinear isotropic hardening material model, as shown in Equation (2.1), were randomly changed about 250 and 500 times at the intervals presented in Table (5.1) as input to the simulation model of IIT, as depicted in Figure 4.3, to generate 250 and 500 imaginary materials for training the ANNs.

Table 5.1 Variation intervals of the material model parameters for the generation of datasets

Parameter	Interval
$R_{p0,2}$ in MPa	[340; 1050]
R_0 in MPa	[50; 1150]
R_∞ in MPa	[170; 460]
b	[15; 115]

The stress-strain curves of the imaginary materials, as shown in gray in Figure 5.3, are later used as input to the simulation model of the IIT and consequently as output of the ANN. As shown in the left side of Figure 5.1 and Figure 5.2, the imaginary materials are used to generate the force-indentation depth curves and the profile of the indented surfaces to obtain a complete dataset including input and output. Only the ANN that correlates the force-indentation depth curves with the stress-strain diagrams is trained with the 250 and 500 datasets to evaluate the effect of increasing the size of the datasets on the accuracy and flexibility of the trained ANN. The other ANN related to the profile of the indented surfaces are trained with 250 datasets.

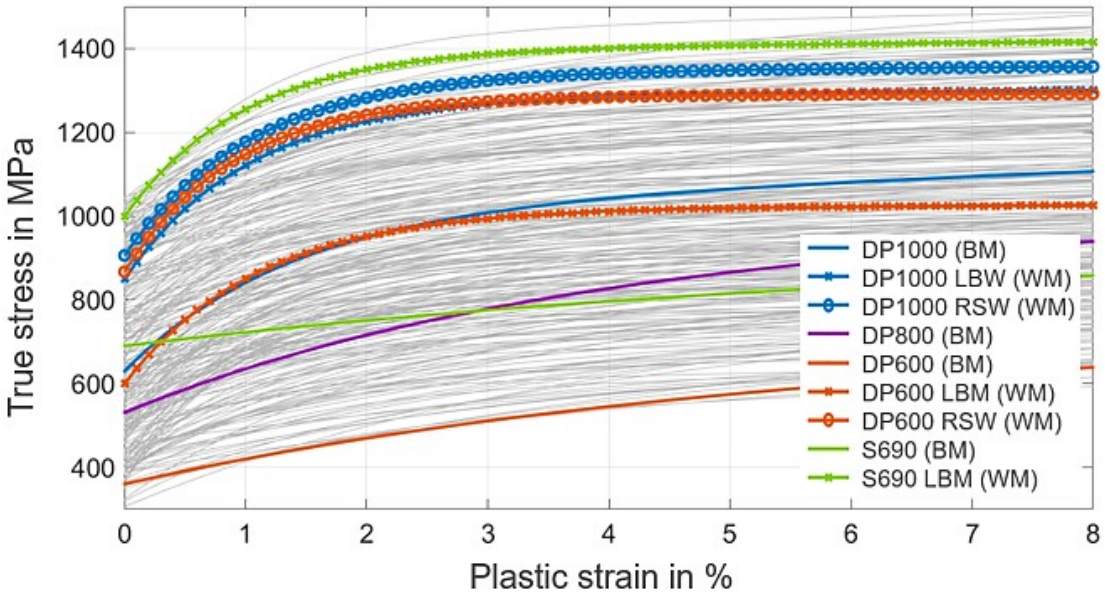

Figure 5.3 Stress-strain curves from the variation of material model parameters based on Table 5.1, the stress-strain curves shown in the legend belong to materials whose mechanical properties are determined using different approaches in chapter three and chapter four as shown in Tables 3.8, 3.10 and 4.2

The material parameters determined in chapters three and four with the notch tensile specimens and the inverse analysis with the simulation model of IIT as given in Table 3.8, Table 3.10 and Table 4.2 are shown in Figure 5.3. They must be used later as test materials to verify the accuracy and applicability of the trained ANNs. Therefore, they are excluded from the training datasets to remain unknown for the ANN. After training the ANN, the output of the ANN is compared with the test materials to quantify the error levels.

5.1.2. Training Datasets based on the Force-Indentation Depth Curves

A considerable rise in the number of neurons or layers increases the complexity of the training process and makes it more difficult to optimally adjust weights and thresholds to minimize the difference between the desired output and the one provided by the ANN. The performance of the neural network in terms of generalization becomes poor and it may lead to overfitting, which is why the features of a dataset must be reduced and the input and output variables for training must be chosen carefully. Therefore, the variables of the training datasets have to be reduced dimensionally.

For instance, a material model with four parameters, based on Equation (2.1), is introduced in the present work to describe the mechanical properties of the material instead of using the entire points in the stress-strain curves. Furthermore, it is required to reduce the number of features in the input. To do this, 15 points that characterize the force-indentation depth curve are selected for the input of the training. The points are distributed over the loading and unloading phases of the curve. The 10th data point is inserted at the end of the loading phase, where the force is maximum. The fifteenth data point is stored at the moment when the load is fully unloaded. Since each point has both x (indentation depth) and y (force) values, this gives a total of 30 features in a dataset. The inputs and outputs of a training dataset are shown in Table 5.2 and Figure 5.4.

Table 5.2 The inputs and outputs of the ANN, trained with dataset of the force-indentation depth curves

Inputs	Outputs
$x_{1\ldots9} = F_{1\ldots9}$ $x_{10} = F_{max} = 120\ N$ $x_{11\ldots15} = F_{11\ldots15}$ $x_{16\ldots24} = h_{1\ldots9}$ $x_{25} = h_{max}$ $x_{26\ldots30} = h_{11\ldots15}$	$t_1 = \mathrm{R_{p0,2}}$ $t_2 = \mathrm{R_0}$ $t_3 = \mathrm{R_\infty}$ $t_4 = b$

The ANN with the dataset of force-indentation depth curves was trained twice, first with a dataset containing 250 and then 500 pairs of inputs and outputs as presented in Figure 5.4. The goal is to evaluate the accuracy and performance of ANNs trained with two different size of datasets. To sum up, the ANN from Figure 5.4 has three layers of input, hidden, and output with 30, 10, and 4 neurons in each layer, respectively.

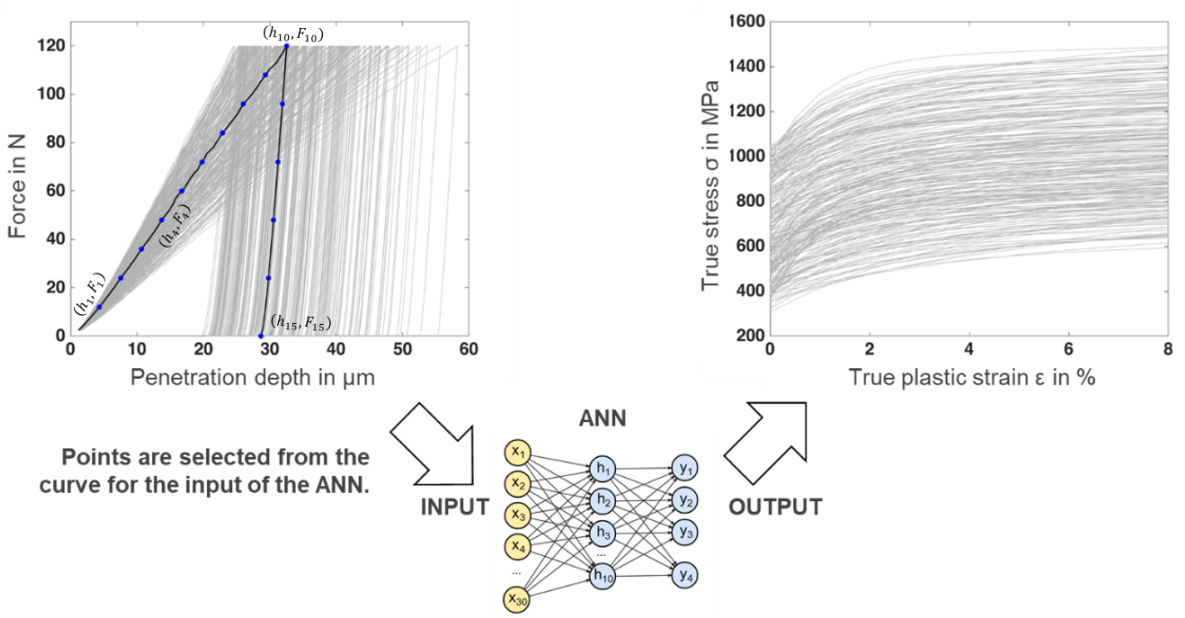

Figure 5.4 Force-Indentation depth curves generated by the FEM model and the corresponding stress-strain diagrams as the training datasets of the ANN with extracting the points as features of the dataset input including the indentation force and the corresponding indentation depth from Force-Indentation depth curve

An important point to improve the performance of ANN training is data normalization, i.e., scaling the data from the original range in such a way that all values lie in the range of 0 and 1, which requires the information about the minimum and maximum observation. Data normalization is necessary since the input and output variables have different units (e.g., MPa, µm, N) which results in the different scales of the variables. Scale mismatches between input variables can increase the complexity of problem modeling. For example, large input values with different ranges lead to a unstable model that has poor learning performance and sensitivity to input values, resulting in higher generalization error. Rescaling of input and output variables is an essential step in the training phase of ANN. Data normalization is performed to improve the accuracy of the subsequent numerical calculation and to obtain more precise outputs.

The inputs, as shown in Table 5.2, include the indentation depth with unit µm (micrometer) and the indentation force with unit N (newton). The value of each indentation depth (h_j) is larger than 0 and smaller than 100 µm in the dataset of "*i*". Moreover, the magnitude of the indentation force (F_j) changes between 0 and 120 N in each dataset. Therefore, each input element (*j*) of dataset (*i*) is divided to 120 in case of force and to 100 for indentation depth, as seen in Equation (5.1), to normalize the input datasets.

$$x_i = \begin{cases} \frac{F_j}{120} \rightarrow j = 1 \dots 15;\ i = 1 \dots 15 \\ \frac{h_j}{100} \rightarrow j = 1 \dots 15;\ i = 16 \dots 30 \end{cases} \tag{5.1}$$

The parameters of the material model used as output of ANN, as given in Table 5.2, were normalized as shown in Equations (5.2) to (5.5). As seen in Table 5.1, the material parameters have different units and were varied in different intervals, which makes it necessary to put them in a similar scale and in the range of 0 to 1.

$$t_1 = \frac{\mathrm{R_{p0,2}} - \min(\mathrm{R_{p0,2}})}{\max(\mathrm{R_{p0,2}}) - \min(\mathrm{R_{p0,2}})} \tag{5.2}$$

$$t_2 = \frac{\mathrm{R_0} - \min(\mathrm{R_0})}{\max(\mathrm{R_0}) - \min(\mathrm{R_0})} \tag{5.3}$$

$$t_3 = \frac{\mathrm{R_\infty} - \min(\mathrm{R_\infty})}{\max(\mathrm{R_\infty}) - \min(\mathrm{R_\infty})} \tag{5.4}$$

$$t_4 = \frac{b - \min(\mathrm{b})}{\max(\mathrm{b}) - \min(\mathrm{b})} \tag{5.5}$$

5.1.3. Training Datasets based on the Profile of the Indented Surfaces

In addition to the force-indentation depth diagram, the profile of the surface deformed by the indentation test can be obtained from the numerical simulation and used to train an ANN to characterize the material parameters. As mentioned in chapter four, when the force is removed after performing the IIT, the surface of the steel specimen does not completely recover, instead an indentation depth due to plastic deformation is formed in the contact area. The idea in the present work is to build a correlation

between the material parameters and the deformed surface of the specimen after performing the IIT.

The procedure of training with the datasets from the profile of indented surfaces is in principle similar to training with force-indentation depth diagram as explained in the previous section. The difference between the training methodologies lies in the generation of the training input datasets with numerical simulation model. The simulation model is basically the same, however other variables are exported. For instance, in the force-indentation depth diagram, the maximum force and the indentation depth as well as the force and the corresponding indentation at each loading and unloading increments are stored.

However, in order to train the ANN with profile of the indented surface, in the last increment and after removing the force, all values in x (distance from the center of indentation) and y (indentation depth) direction from the nodes in the contact line between the steel sample and the indenter are extracted. Finally, 15 points as shown in Figure 5.5 are selected from the deepest to the highest point of the indented surface to be used as the feature of the datasets. As seen in Table 5.3, each point consists of two pieces of information, including the indentation depth and the distance from the center of indentation, consequently, the total number of elements of the input is 30 and the output holds 4 parameters of the nonlinear isotropic material model as described in Equation (2.1).

Table 5.3 The inputs and outputs of the ANN, trained with dataset from the profile of the indented surface

Inputs	Outputs
$x_{1\ldots15} = h_{1\ldots15}$	$t_1 = \mathrm{R_{p0,2}}$
$x_{16\ldots30} = S_{16\ldots30}$	$t_2 = \mathrm{R_0}$
	$t_3 = \mathrm{R_\infty}$
	$t_4 = b$

The numerical simulation were repeated 250 times to generate 250 datasets for the training of the ANN based on profile of the indented surface. As seen in Figure 5.5, three layers of input, hidden, and output of the ANN has 30, 10, and 4 neurons, respectively. Following the same procedure as in Section 5.1.2, the outputs of each dataset are normalized to increase the performance of the ANN. Each element in the

input of the ANN is similarly normalized by a linear scale transformation and their value is mapped between -1 and 1, where -1 and 1 represent the minimum and maximum possible quantities.

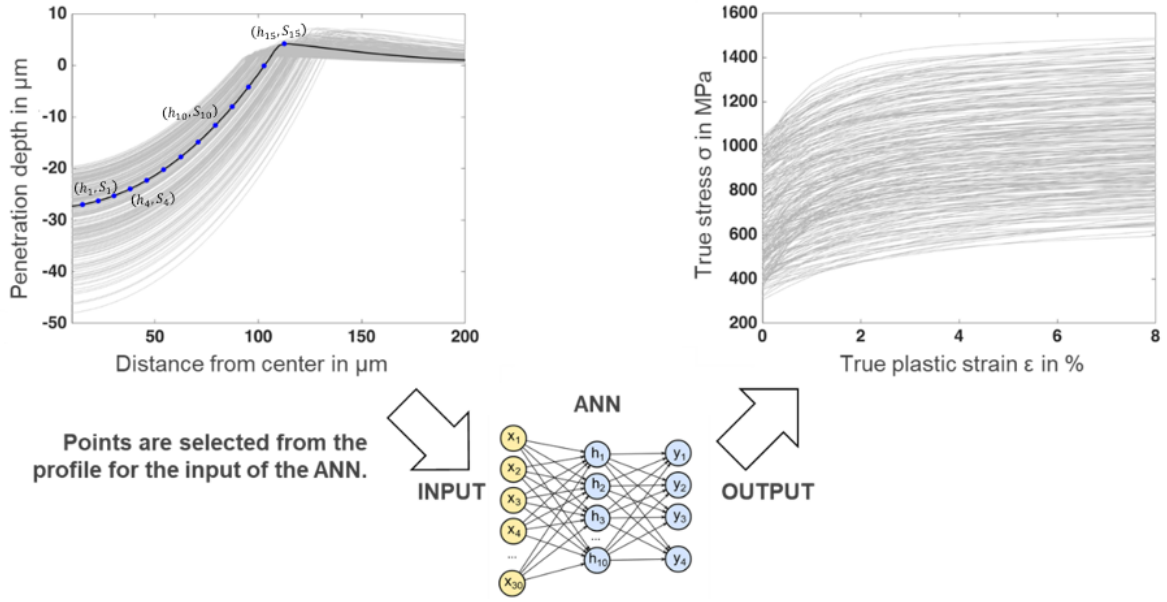

Figure 5.5 Indented surface profiles generated by the FEM model and the corresponding stress-strain curves as the ANN training datasets with extracting the points as features of the dataset input including the indentation depth and its corresponding distance from the center of the indentation

5.1.4. Training and Architecture of Artificial Neural Network

Once the datasets are provided, ANN training can begin with the goal of finding a general relationship between the inputs and outputs. The ANN can approximate unknown data well within the training range corresponding to the values contained in training datasets. Through training, the ANN memorizes the training datasets as examples and learns to adapt to new situations. However, intensive learning or little control over the training process can lead to overfitting, meaning that the ANN is so highly adapted to the training datasets that it has difficulty in generalizing to unknown datasets and consequently making good predictions.

One of the methods to increase the generalization capability is to divide the datasets into three subsets such as training, validation and test datasets. An ANN is trained with the training datasets to minimize the error between the calculated and desired outputs during training by setting the appropriate weights and thresholds. The

validation dataset is not used to train the ANN, instead the accuracy of the ANN is quantified by using the final parameters from the training phase by using the unknown datasets, e.g. the validation dataset, to monitor the training process. Similar to the validation dataset, the error is calculated according to test datasets based on the parameters from the training phase. However, its purpose is to evaluate the quality of the ANN compared to the generalization. Out of 250 and 500 datasets, 80% are randomly allocated for training, 10% for validation, and 10% for testing, with the maximum number of epochs equal to 1000. An epoch means that all datasets pass through the ANN once forward and once backward to recalculate the weights and thresholds. In this methodology, the training procedure stops at a certain epoch when the error in the validation dataset starts to climb several times in a row.

The error between the desired output (t_i) from the training dataset and the actual output (y_i) predicted by a trained ANN can be calculated using the mean square error (MSE). As the MSE gets progressively smaller, the performance of the ANN in terms of generalization gets continuously better. In the training phase, the MSE of validation and test datasets must be calculated separately and in most cases is larger than the MSE of test dataset in the training phase. The trained ANN does not know the validation and test datasets and approximates these data only based on the knowledge from the training dataset. As mentioned in chapter three, MSE can be calculated by using Equation (5.6) as follows:

$$MSE = \frac{1}{n}\sum_{i=1}^{n}(t_i - y_i)^2 \tag{5.6}$$

After performing the training, the training datasets are fed into the ANN once again to form the linear regression, which quantitatively describes the relationship between the desired and actual outputs and is normally employed in the algorithms such as ANN. The Pearson correlation coefficient (R) is a property of linear regression that shows the linear dependency between two variables, and when it becomes equal to one means that the model fits perfectly. The correlation coefficient provides a quantifiable assessment of whether the goal of the training was achieved and how well actual outputs match desired outputs and can be calculated from Equation (5.7) where μ and σ are the mean and the standard deviation of the population, respectively.

$$R = \frac{1}{n-1}\sum_{i=1}^{n}\left(\frac{y_i - \mu_{\text{actual output}}}{\sigma_{\text{actual output}}}\right)\left(\frac{t_i - \mu_{\text{desired output}}}{\sigma_{\text{desired output}}}\right) \quad (5.7)$$

The MSE and the correlation coefficient (R) can be used to quantitatively compare and evaluate the quality of the ANN training. The challenge in comparing the different trained ANNs is that they give different outputs even if the configuration of the ANN is the same. This is due to the randomness within the distribution of the training, validation and test datasets and the arbitrary initialization of the starting weights and thresholds at each training sequence which leads to different solutions for the same problem. Having inadequate randomness in the datasets distribution and training parameters initialization can result in a trained ANN with large error, which is not flexible enough and has low generalization.

Cross-validation can be used to make a statement about the quality of the trained ANN based on the new datasets that are unknown to the trained ANN. The datasets can be divided into two separate categories; for instance, one for training the ANN and one for evaluating the quality of the trained ANN. Monte Carlo cross-validation is used to randomly split the datasets into training and validation records multiple times. Every instance, the model is fitted to the training datasets and the performance of the ANN is evaluated against the validation datasets. The number of repetitions is important to reduce uncertainty about the model performance. In the present work, 50 ANNs with different distribution datasets were trained to evaluate the MSE and correlation coefficient from each dataset configuration based on the Monte Carlo cross-validation concept. After training the ANNs 50 times, an ANN with the smallest MSE and the largest correlation coefficient is selected as the representative ANN with the best performance, whose outputs are then tested with test datasets.

Subsequently, an optimal architecture of the ANN must be found based on the number of hidden layers and the number of neurons in each hidden layer. It is recommended in the literatures [139] [140] [141] that the number of neurons in the hidden layers must be between the number of neurons in the input and output layers, or it must be two-thirds of the sum of the neurons in the input and output layers, or the number of neurons in the hidden layers should not exceed twice the number of neurons in the input layer. However, it is not possible to follow the above recommendations as the hidden layers also depend on the randomness of the dataset distribution and initialization of parameters, training algorithms, number of

training datasets, and so on. Furthermore, if the ANN contains two hidden layers, the number of neurons in each of these layers must remain the same to increase the performance of the ANN [142].

The number of neurons in the hidden layer is gradually increased from 5 to 29 neurons based on the above suggestions to determine the best number of hidden neurons by evaluating the MSE and correlation coefficient for each configuration based on the cross-validation concept. The configuration of the ANN was changed with 5, 8, 10, 15, 20, and 25 neurons in one hidden layer and with the same number of neurons of 5, 10, and 15 in two hidden layers. The relationship between the number of neurons in the hidden layers and the MSE or correlation coefficient are shown in Figure 5.6 and Figure 5.7, respectively.

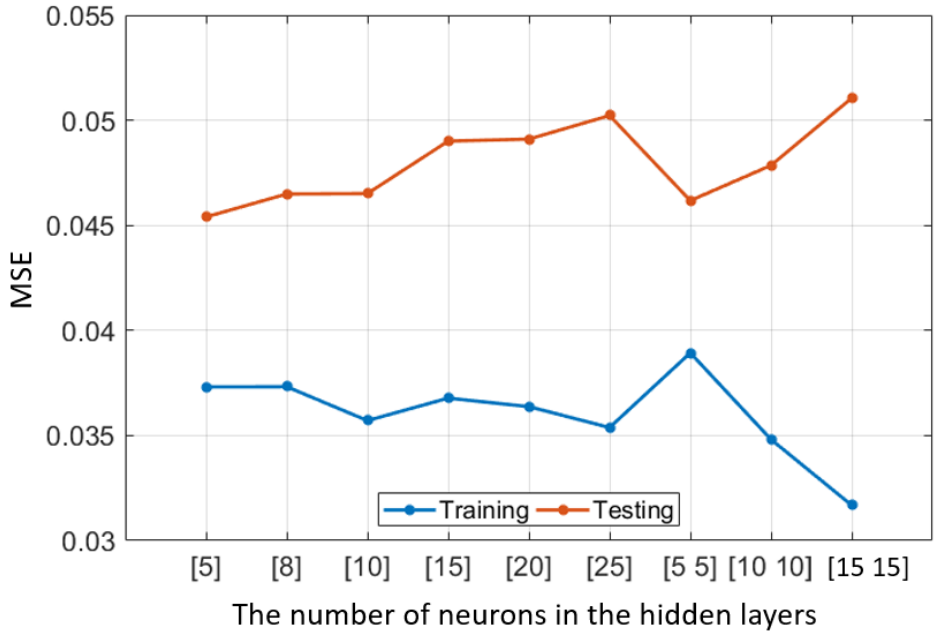

Figure 5.6 The relationship between the number of neurons in the hidden layers and the mean square error (MSE) obtained from the training and testing datasets, the first six ANNs have one hidden layer and the last three ANNs have two hidden layers with 5, 10 and 15 neurons in each layers

As seen in Figure 5.6, the blue line shows the MSE resulting from the training datasets, which decreases as the number of hidden neurons increases. Since the MSE of the test datasets is increased by decreasing the MSE of the training datasets, it can be concluded that adding more hidden neurons leads to overfitting. As one of its indicators is a low MSE from the training datasets and at the same time a large MSE from the test datasets as it is clear for the ANNs with two hidden layers. The MSE from the training datasets with 5 hidden neurons is relatively large, which means

that the ANN did not learn well from the training datasets since its coefficient correlation especially for the material parameter of b is worse than the other configurations of the ANN. An ANN with 10 neurons in the hidden layer shows the best combination of results compared to the other configurations of ANN and is therefore used in the present work.

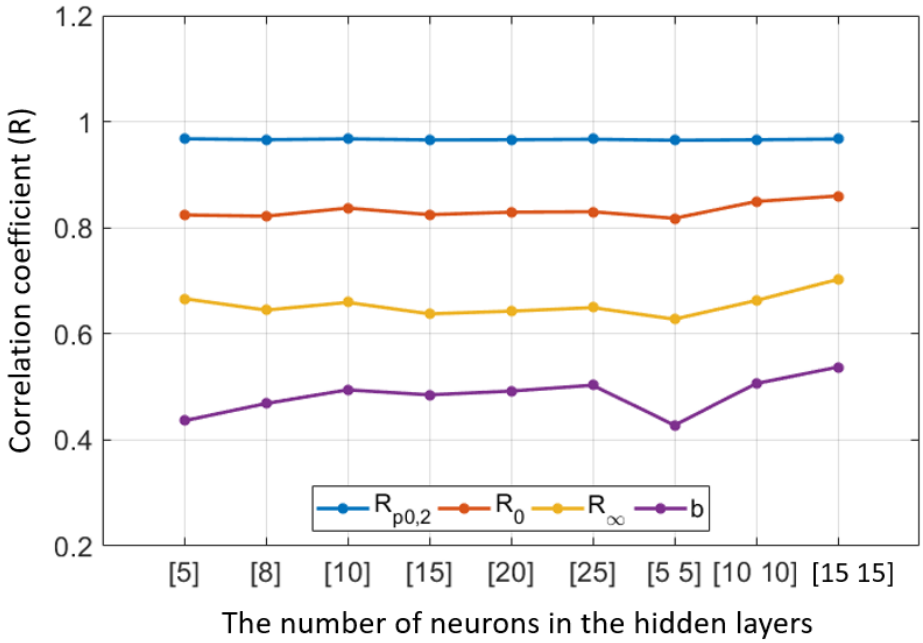

Figure 5.7 The relationship between the number of neurons in the hidden layers and the correlation coefficient obtained by comparing the calculated and desired outputs (four material model parameters of Equation (2.1)), the first six ANNs have one hidden layer, and the last three ANNs have two hidden layers with 5, 10 and 15 neurons in each layers

Furthermore, the Levenberg-Marquardt backpropagation algorithm (LMA) [143], developed by Kenneth Levenberg and Donald Marquardt, provides a numerical solution to the problem of minimizing a nonlinear function using the least squares method. LMA is one of the fastest algorithms for backpropagation and has stable convergence, however, requires more memory than other algorithms. The LMA combines the gradient descent and the Newton algorithm together to maintain the stability of the first algorithm and become faster by taking advantage of the latter approach. It is more robust than the Newton algorithm as it can converge well in many conditions even when the error surface is much higher in complexity than the quadratic situation. In the domain with complex contour, the gradient method is employed as long as the local curvature allows a quadratic approximation, then the Newton method can be applied to accelerate the convergence. The mathematical description of LMA is demonstrated [144] [145] in Equation (5.8).

$$x_{i+1} = x_i - [H + \mu I]^{-1} g = x_i - [J^T J + \mu I]^{-1} J^T e \quad (5.8)$$

In the above equation, the terms H and g represent the Hessian matrix and the gradient containing the Jacobian matrix (J) and the network error vector (e), respectively. The variable μ indicates by having a large value that the algorithm becomes gradient descent, and when its value is decreased, the importance of the Newton approach increases to speed up the function performance, and when it becomes zero, the Equation (5.8) becomes the Newton method. Due to the aforementioned advantages, this algorithm is implemented in the present work to find the minimums of the cost function in order to optimally adjust ANN.

5.2. Results and Discussion

After training the ANNs with the datasets of the force-indentation depth diagrams and the profile of the indented surfaces, it is necessary to evaluate and discuss the accuracy and repeatability of the predicted outputs as well as the reliability and precision of the trained ANNs. As explained in Section 5.1.4, about 50 ANNs were trained individually with different configuration of training, validation and test datasets according to each sort of datasets and the results and parameters of the best trained ANN are presented here. First the result of the trained ANNs with the dataset of force-indentation depth diagrams with the size of 250 and 500 records is detailed, and then the training protocols of the ANN trained with the dataset of the profile of the indented surfaces are described. Finally, the sensitivity analysis evaluates the effect of each material parameter and its weighting on the overall stress-strain diagram.

5.2.1. Trained ANN with the Force-Indentation Depth Curves Datasets

First, the ANN was trained with the dataset of force-indentation depth diagrams with the size of 250 records and the results discussed here are shown in Figures 5.8 to 5.10 and Table 5.4. Figure 5.8 shows the MSE value of the training, validation, and testing dataset for each epoch, which provides an opportunity to observe the error progression during the training process. The error is quite large at the beginning due to the randomly initialized weights and thresholds, and decreased significantly after

one epoch and the MSE is reduced as the ANN is iteratively adjusted at each epoch. From the 5th epoch, the error decreases slightly slower and at the 42nd epoch the training stops, since the error of the validation dataset increases about 6 times consecutively from 36th epoch, which is an indicator of possible overfitting. The best validation performance happens at epoch 36 with MSE of around 0.044. The training datasets are returned to the trained ANN to quantify the frequency distribution of errors from the training datasets by calculating the differences between the desired outputs and the outputs calculated by the ANN. The trained ANN can approximate the material parameters mostly with error close to zero which is an indicator of ANN performance.

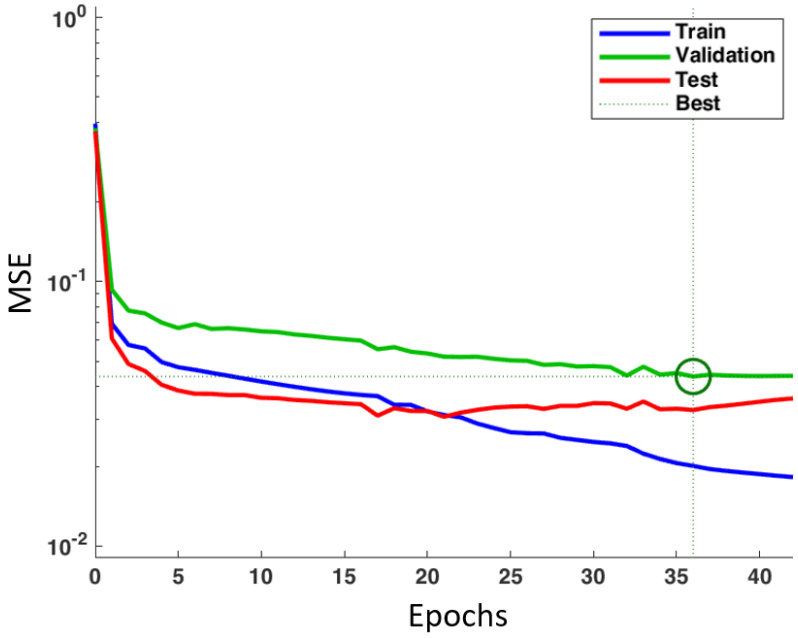

Figure 5.8 Development of the MSE value in each epoch from the training, validation, and testing datasets for the ANN trained with the Force-Indentation depth curves (250 datasets)

To verify that the training objective is met, the Pearson correlation coefficient (R) of each data subset must be calculated and compared with each other by feeding the ANN with all datasets and then forming a linear regression between the calculated and desired outputs. The correlation coefficient of the training dataset, as expected, is the highest with a value of 0.81, since the ANN fitting is performed based on this subset of data. On the other hand, the validation and testing datasets show lower but still good accuracy with the correlation coefficient of 0.88 and 0.77, respectively.

In addition, the correlation coefficient of each ANN output is calculated after all normalized data are converted to their original values to better observe the accuracy

of the predicted material model parameters from the training datasets. As seen in Figure 5.9, the correlation coefficient of yield strength has the highest value compared to other strain hardening parameters and is approximately 0.98 which shows that the ANN can determine it better than other material model parameters. Moreover, it is difficult to estimate the material model parameter b with a high accuracy as its correlation coefficient is almost 0.73. However, the parameters such as correlation coefficient or MSE are only the first indications of the ANN's performance. The more detailed evaluation about the ability of the ANN to predict the material model parameters must be performed after testing the ANN with unknown datasets.

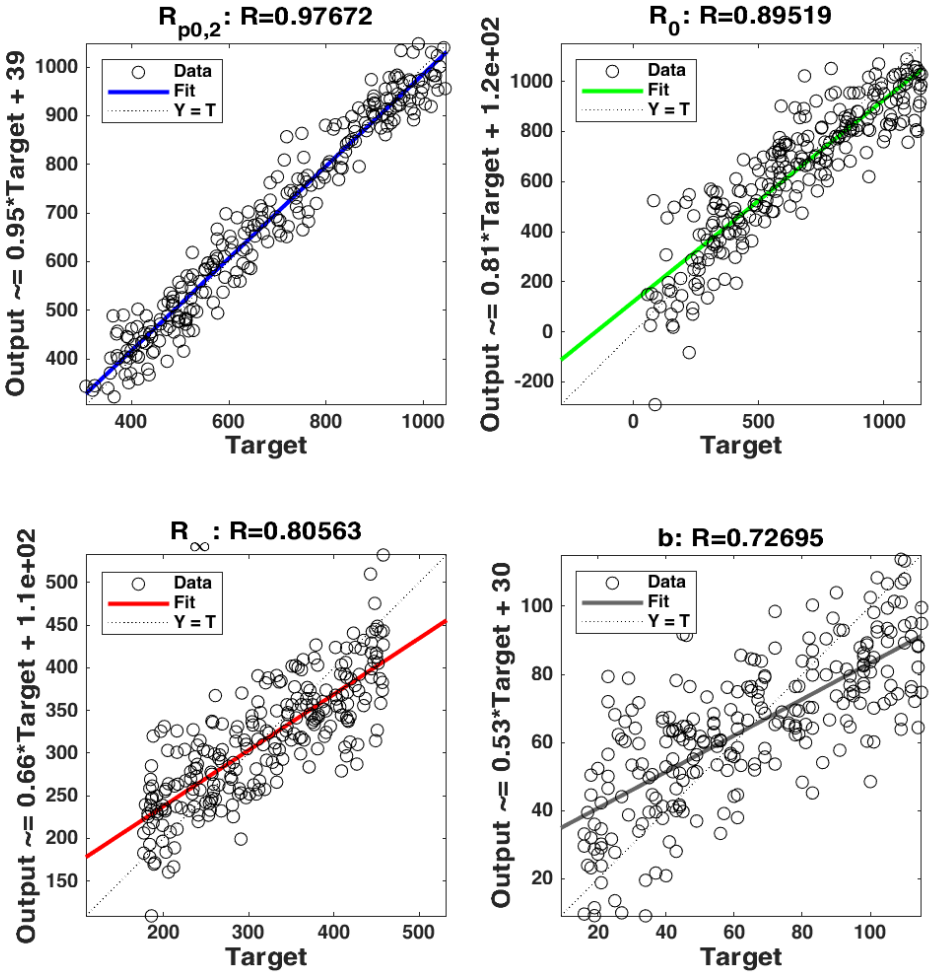

Figure 5.9 Correlation coefficient (R) obtained by comparing the desired outputs and outputs of the trained ANN with the Force-Indentation depth curves

After the trained ANN with the dataset of force-indentation depth curves is obtained, the accuracy and functionality of the trained ANN must be verified by comparing its outputs with the material model parameters of the unknown materials to quantify, once again, the error range of the ANN prediction. As seen in Table 5.4, the

mechanical properties of various test materials, whose actual (real) parameters were determined in chapters three and four and shown in Tables 3.8, 3.10, and 4.2, are compared to the parameters predicted by the ANN, and their deviation is quantified based on Equation 5.9. Once again, the real material model parameter sets of each material which is known as the reference is given as the input to the validated numerical simulation model of IIT as shown in chapter four to calculate the corresponding force-indentation depth curves. The trained ANN are fed with the generated force-indentation depth curves and the output of the ANN is considered as the prediction.

$$Deviation\ (Dev.) = \frac{|Reference - Predtion(Pred.)|}{Reference} \times 100\% \tag{5.9}$$

As seen in Table 5.4, the mean value of deviation between the reference and the predicted magnitude of yield strength is the lowest compared to other material model parameters, which is in agreement with the correlation coefficient of 0.98 between the desired and calculated value of $R_{p0,2}$ as shown in Figure 5.9. On the other hand, the strain hardening parameters such as exponential saturation rate (b) or the line tangent of stress-strain diagram in the plastic region (R_0) can be predicted with the lower accuracy which is around 64% and 78%, respectively.

Table 5.4 Quantification of the deviation (Dev.) between the outputs of the trained ANN (Pred.) with the Force-Indentation depth curves (250 datasets) and the reference values whose mechanical properties are determined using different approaches in chapter three and chapter four as shown in Tables 3.8, 3.10, and 4.2

Material	$R_{p0,2}$		R_0		R_∞		b	
	Pred.	Dev.	Pred.	Dev.	Pred.	Dev.	Pred.	Dev.
DP1000 (BM)	692	10%	941	14%	384	1%	44	39%
DP1000 LBW (WM)	961	13%	-19	111%	388	11%	42	57%
DP1000 RSW (WM)	964	6%	563	222%	289	34%	94	2%
DP800 (BM)	568	7%	928	111%	250	41%	59	118%
DP600 (BM)	359	0%	527	26%	319	19%	22	0%
DP600 LBW (WM)	605	1%	52	31%	386	8%	95	5%
DP600 RSW (WM)	954	10%	-11	117%	356	15%	70	37%
S690 (BM)	593	14%	305	22%	239	30%	69	307%
S690 LBW (WM)	997	0%	293	46%	406	1%	91	9%
Mean Value of Deviation		7%		78%		18%		64%

Although the magnitude of the difference between the prediction and reference material model parameters depends on the model parameters and material type, the

question is how large are the differences between the entire stress-strain curves of prediction and reference. Figure 5.10 compares the stress-strain curves from the experiment with the output from ANN to demonstrate the differences between the two curves resulting from the deviation between the material parameters, as calculated in Table 5.4. For instance, Table 5.4 shows that the maximum deviation between the predicted and reference yield strength are 14% and 13% which belongs to BM of S690 and WM of DP1000 from LBW, respectively. On the other hand, the magnitude of the deviation between other parameters of the mentioned materials is relatively high, e.g. the difference between the predicted and calculated b and R_o is about 307% and 111% for BM of S690 and WM of DP1000 from LBW, correspondingly.

However, Figure 5.10 shows that the agreement between the predicted and reference stress-strain diagram of S690 BM and WM of DP1000 from LBW are lower than the other stress-strain curves, though still acceptable and strong. It came from the fact that each material parameter has a specific weight on the final shape of stress-strain diagram, and a small error in one of them such as $R_{p0,2}$ may completely change the entire stress-strain diagram, while another parameter such as b may not have a strong impact on the ultimate value of the stress. The influence of each material model parameter on the final stress-strain curve will be assessed and quantified in the next section, called Sensitivity Analysis.

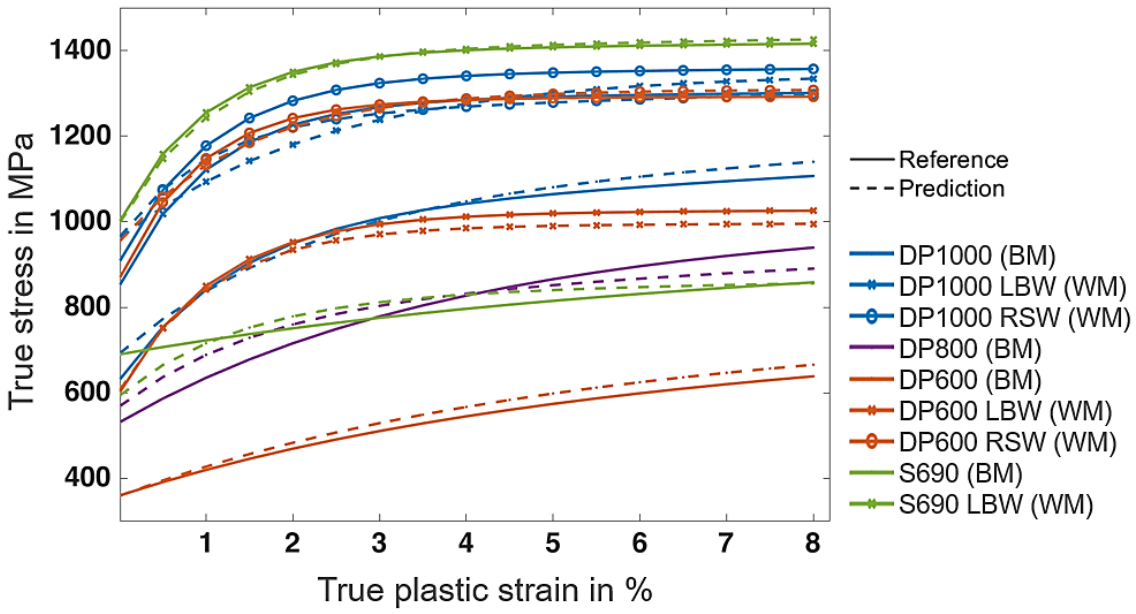

Figure 5.10 Comparison between the output of the ANN trained with the Force-Indentation depth curves (250 datasets) and the reference values whose mechanical properties are determined using different approaches in chapter three and chapter four as shown in Tables 3.8, 3.10 and 4.2

In addition to the former ANN, another ANN is trained with the force-indentation depth curve dataset using duplicate (500) records to investigate the effect of increasing volume of data on the accuracy of the trained ANN. Table 5.5 shows the predicted material parameters by the ANN trained with 500 records and the deviation between the real and predicted parameters according to Equation (5.9). As seen in Table 5.5, the magnitude of the mean deviation between the predicted and reference yield strength improved by 3% and became 4%. Moreover, other strain hardening parameters, especially b, can be predicted much better when the amount of training records is increased.

Table 5.5 Quantification of the deviation (Dev.) between the outputs of the trained ANN (Pred.) with the Force-Indentation depth curves (500 datasets) and the reference values whose mechanical properties are determined using different approaches in chapter three and chapter four as shown in Tables 3.8, 3.10, and 4.2

Material	$R_{p0,2}$		R_0		R_∞		b	
	Pred.	Dev.	Pred.	Dev.	Pred.	Dev.	Pred.	Dev.
DP1000 (BM)	659	5%	952	13%	400	2%	55	24%
DP1000 LBW (WM)	890	5%	139	21%	392	10%	82	15%
DP1000 RSW (WM)	973	7%	337	92%	350	20%	83	14%
DP800 (BM)	583	10%	982	123%	242	43%	50	86%
DP600 (BM)	350	3%	617	13%	298	11%	26	18%
DP600 LBW (WM)	613	2%	190	153%	337	20%	83	8%
DP600 RSW (WM)	839	3%	103	58%	426	1%	124	12%
S690 (BM)	678	2%	418	6%	171	7%	34	101%
S690 LBW (WM)	1013	1%	141	30%	404	1%	87	13%
Mean Value of Deviation		4%		57%		13%		32%

Although the mean value of the deviation between the reference and predicted parameters are improved by increasing the records volume, the estimation of the material parameters of some steels, such as WM of DP600 from LBW, are degraded by comparing Table 5.4 and Table 5.5, which can further be seen in Figure 5.11. On the other hand, the prediction of mechanical properties of some other materials such as BM of S690 have been improved drastically. The comparison of Figure 5.10 and Figure 5.11 shows that a larger number of datasets generally results in a more accurate ANN, however, for some materials the accuracy of the prediction may be lower.

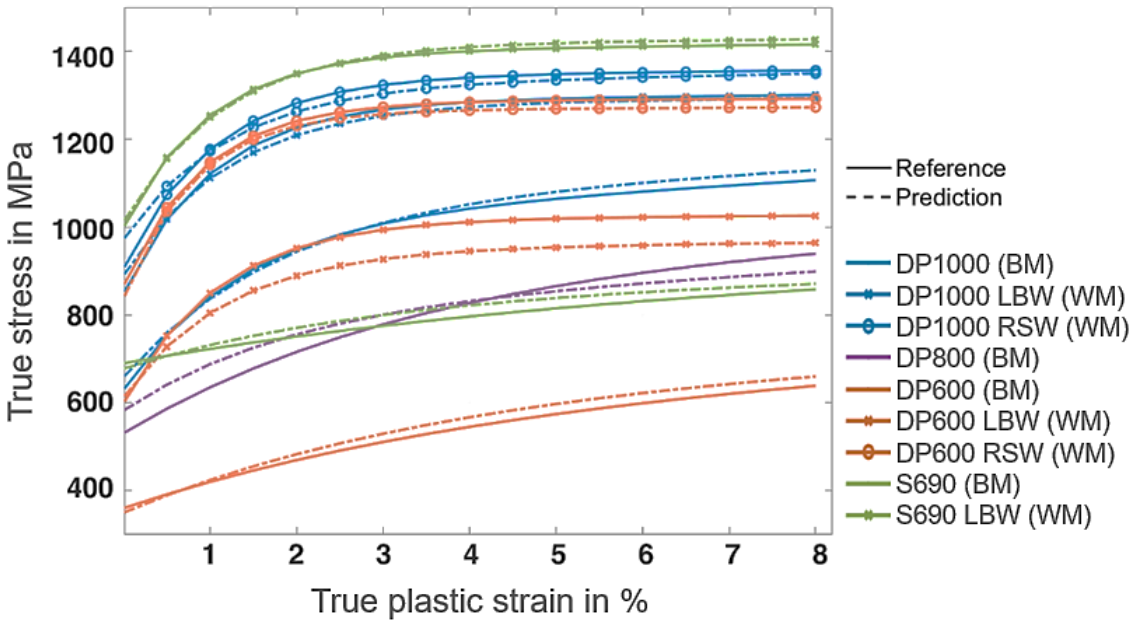

Figure 5.11 Comparison between the output of the ANN trained with the Force-Indentation depth curves (500 datasets) and the reference values whose mechanical properties are determined using different approaches in chapter three and chapter four as shown in Tables 3.8, 3.10 and 4.2

Furthermore, the comparison between the correlation coefficients obtained from the regression plots produced by comparing the reference and predicted outputs of the ANNs trained with 250 and 500 records show that the correlation coefficient of the material parameter b increased significantly when more records were available, which is in agreement with the results obtained by comparing the mean deviation of this material parameter between Table 5.4 and Table 5.5. In addition, the correlation coefficient of other material model parameters such as yield strength or line tangent of the stress-strain diagram in the plastic region was improved, though not at the same level as the exponential saturation rate (b).

5.2.2. Trained ANN with the Profile of the Indented Surfaces Datasets

In the next step, another ANN was trained with the dataset of the indented surface profile with 250 datasets to determine the mechanical properties of the indented specimens. Similar to the previous section, 50 ANNs were trained with different configurations of training, validation and testing datasets and the results and parameters of the best ANN are presented here. As seen in Figure 5.12, the training process ends at epoch 95 and the ANN of the 89th epoch with the validation

performance of 0.0095 is delivered back. Figure 5.12 shows that the MSE of the training and validation datasets decreased continuously until epoch 89. However, after this epoch, the MSE of the training datasets declined while the MSE of the validation slightly increased, which is an indicator of overfitting after epoch 89 which can similarly be observed in the MSE value of the test datasets. Generally, a larger number of epochs and recalculation of weights by more iterations may result in a lower value of MSE, however, it does not guarantee an optimally trained ANN.

Furthermore, the comparison between the MSE value development of the ANNs trained with the force-indentation depth curves and profiles of indented specimens datasets, shown in Figure 5.8 and Figure 5.12, respectively, reveal that the MSE value of the ANNs trained with the latter datasets is lower than that of the former one. Therefore, the ANN with training datasets of the profile of the indented surface is expected to provide more accurate and precise results compared to the ANNs trained in Section 5.2.1.

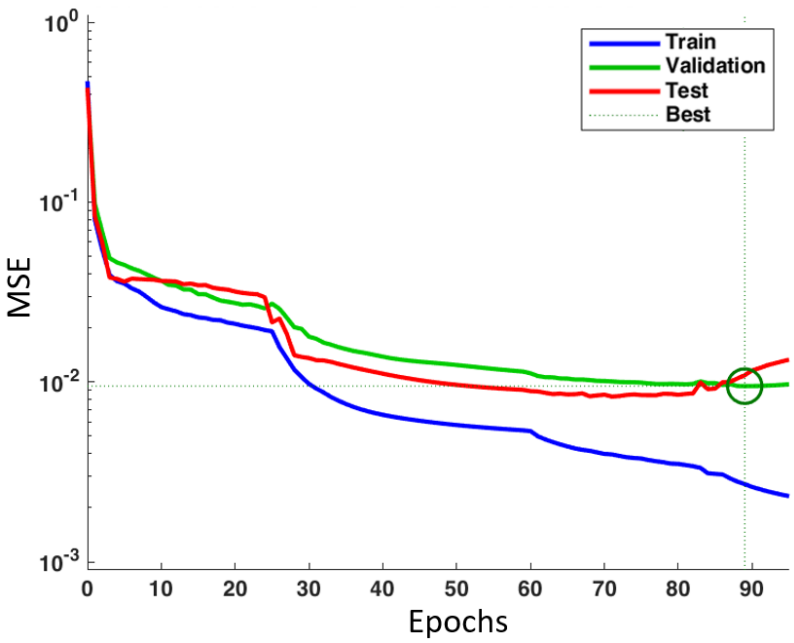

Figure 5.12 Development of the MSE value in each epoch from the training, validation, and testing datasets for the ANN trained with the profile of the indentation surface (250 datasets)

In the next step to evaluate the accuracy of the trained ANN, Figure 5.13 shows the correlation coefficients of the different material model parameters calculated by comparing the desired and predicted outputs. All material parameters have extremely high correlation coefficients with maximum and minimum values of 0.996 and 0.946, which belong to the yield strength and exponential saturation rate, respectively,

demonstrating the performance and accuracy of the trained ANN. Although the current ANN was trained with only 250 datasets, the correlation coefficient of its outputs is higher than that of the previous ANN trained with 500 datasets, showing that instead of increasing the dataset volume, generating more qualitative datasets can lead to a better performance.

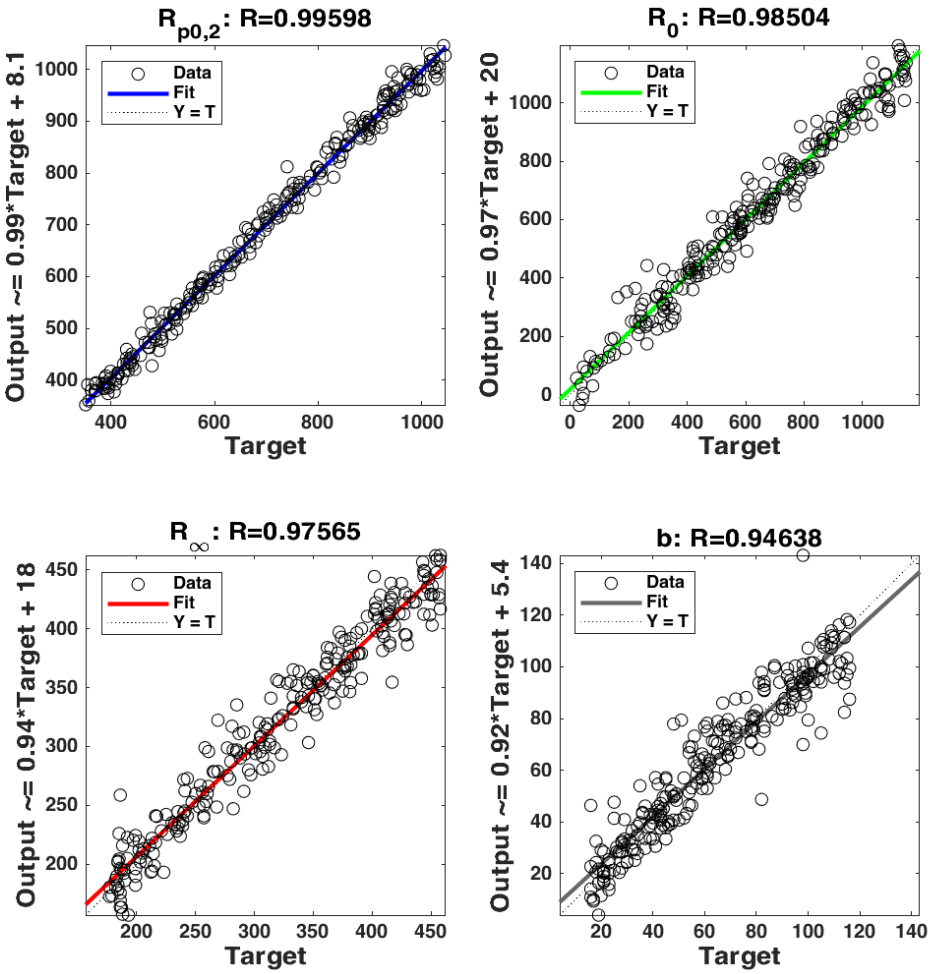

Figure 5.13 Correlation coefficient (R) obtained by comparing the desired outputs and outputs of the trained ANN with profile of the indented surface (250 datasets)

In addition, the results of the trained ANN with the datasets of the indented surface profile must be checked with the parameters of the unknown materials in a similar way as explained in Section 5.2.1. As seen in Table 5.3, the current ANN can predict the yield strength with a mean deviation of about 4% and other strain hardening parameters with a mean deviation of less than or equal to 21%. The comparison of the data from Table 5.5 with Table 5.6 shows that not only the average deviation of the records in Table 5.6 is lower than in Table 5.5, but also the maximum value of the deviation for each material parameter was reduced by training the ANN with a

different type of dataset. For instance, the maximum value of deviation for yield strength in Table 5.6 is 7%, whereas the maximum value of the similar parameter in Table 5.5 is 10%. Therefore, the agreement between the entire stress-strain curves of the prediction and the reference is expected to be reduced by using the indented surface profiles instead of the force-indentation depth curves as training datasets which is also in consistency with value of the correlation coefficient.

Table 5.6 Quantification of the deviation (Dev.) between the outputs of the trained ANN (Pred.) with the profile of the indented surfaces (250 datasets) and the reference values whose mechanical properties are determined using different approaches in chapter three and chapter four as shown in Tables 3.8, 3.10, and 4.2

Material	$R_{p0,2}$		R_0		R_∞		b	
	Pred.	Dev.	Pred.	Dev.	Pred.	Dev.	Pred.	Dev.
DP1000 (BM)	618	2%	1063	3%	412	6%	87	21%
DP1000 LBW (WM)	891	5%	158	10%	395	10%	101	5%
DP1000 RSW (WM)	923	2%	208	19%	414	5%	114	18%
DP800 (BM)	539	2%	436	1%	412	2%	11	58%
DP600 (BM)	350	3%	645	9%	313	17%	23	3%
DP600 LBW (WM)	634	6%	147	96%	386	8%	89	1%
DP600 RSW (WM)	930	7%	53	19%	364	13%	91	18%
S690 (BM)	728	6%	438	11%	147	20%	15	13%
S690 LBW (WM)	980	2%	160	20%	471	18%	119	19%
Mean Value of Deviation		4%		21%		11%		17%

In the last step to evaluate the performance of the current ANN, the stress-strain curves of the unknown materials obtained from the ANN are qualitatively compared with the reference ones as shown in Figure 5.14. Figure 5.14 shows that there is a strong correlation between the predicted and reference stress-strain curves for almost all unknown materials, however, the ANN can estimate the stress-strain curves of some materials, such as BM of DP1000, better than other steels, such as BM of DP800, as expected based on the data mentioned in Table 5.6. As mentioned in Section 5.2.1, each material parameter has its own weight on the overall stress-strain curves and estimating a parameter that does not have a strong influence on the entire curve with a low accuracy does not lead to a significant deviation between the reference and the prediction. The significance of each material parameter in the material model is discussed in the next section, which helps to better understand the influence of each material parameters deviation on the overall stress-strain curve.

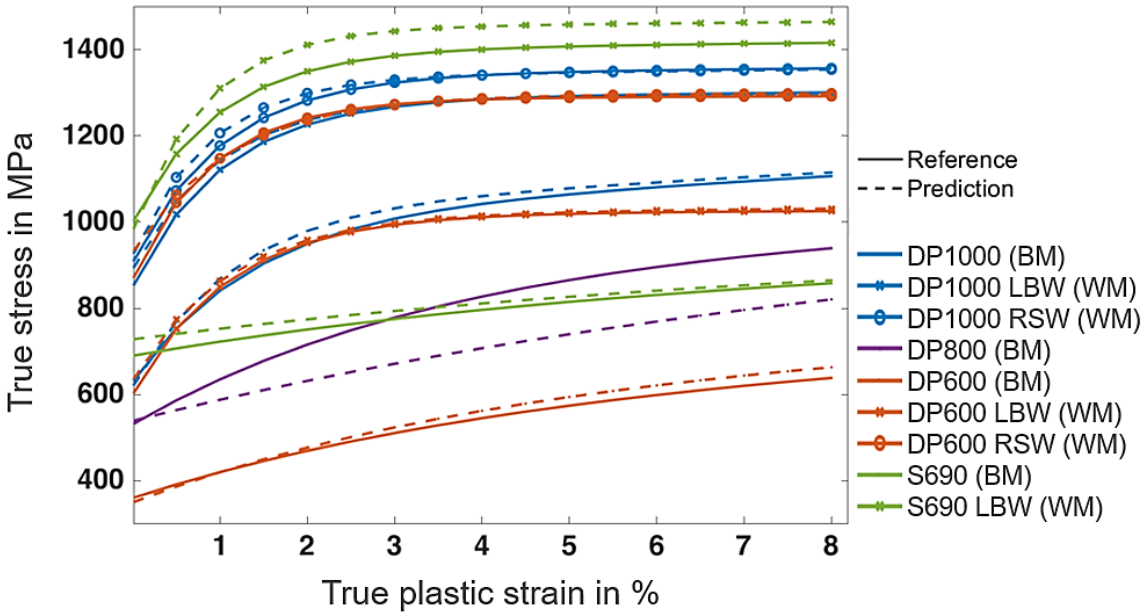

Figure 5.14 Comparison between the output of the ANN trained with the profile of the indented surfaces (250 datasets) and the reference values whose mechanical properties are determined using different approaches in chapter three and chapter four as shown in Tables 3.8, 3.10 and 4.2

5.2.3. Sensitivity Analysis

Despite the relatively high mean value of deviation between some of the calculated and reference material model parameters such as “b”, as seen in Table 5.4, Table 5.5, and Table 5.6, there is a slight disagreement between the entire calculated and reference stress-strain curves, as shown in Figure 5.10, Figure 5.11, and Figure 5.14. The reason for that is the different weight of the individual material parameters on the entire stress-strain curve, which can be visualized and understood by performing the sensitivity analysis.

For performing the sensitivity analysis, each material model parameter was varied individually based on the interval given in the Table 5.1, while the other three parameters were kept constant. For instance, the material parameter "b" has been modified from 15 to 115 and then the corresponding stress-strain curves for each variation of up to 10% of the plastic strain have been calculated, as seen in Figure 5.15. Then, the stress magnitude at 8% of plastic strain was recorded to plot the variation in stress according on the modification of the material model parameters at 8% of plastic strain as seen in Figure 5.16. This arbitrary specific percentage of plastic

strain was chosen since fracture occurs after 8% for the welded and not welded steels.

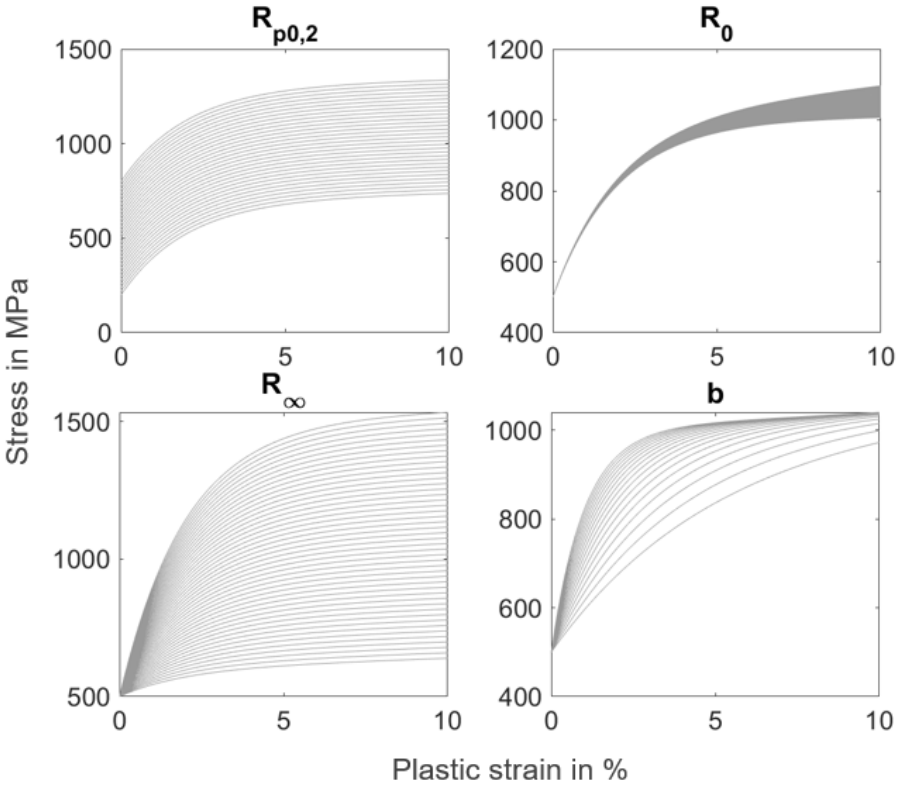

Figure 5.15 Stress-strain curves calculated on the basis of each material model parameter variation according on the interval of Table 5.1

As seen in Figure 5.16 (left and up), the changes of yield strength ($R_{p0,2}$) based on the interval of Table 5.1 as demonstrated in x-axis lead to a significant variation of the stress value at 8% of plastic strain from almost 700 to 1400 MPa as seen in y-axis. Nevertheless, the variation of other material parameters such as R_0, which stands for the tangent of the line in the stress-strain diagram in the plastic region in an interval between 50 to 1150 MPa, varies the total amount of stress only in a range close to 100 MPa, e.g. from 1000 to about 1100 MPa. On the other hand, the Figure 5.16 (left and down) shows that the variation of material model parameter R_∞ which presents the difference between the yield strength and the saturation stress has more effect on the changes of the stress in comparison to parameter R_0. For instance, when R_∞ changes for 290 unites, the total amount of stress at 8% of plastic strain varies almost less than 350 MPa. Similarly, changing the exponential saturation rate (b) between the interval of 15 to 115 does not dramatically change the amount of stress at 8% of plastic strain e.g. only in less than 100 MPa. However, its changes show a significant effect on area of the transition mode from elastic to plastic behavior which

is at initiation of plasticity and depending on the configuration of the other material model parameters, especially the yield strength, as shown in Figure 5.15 (right and below).

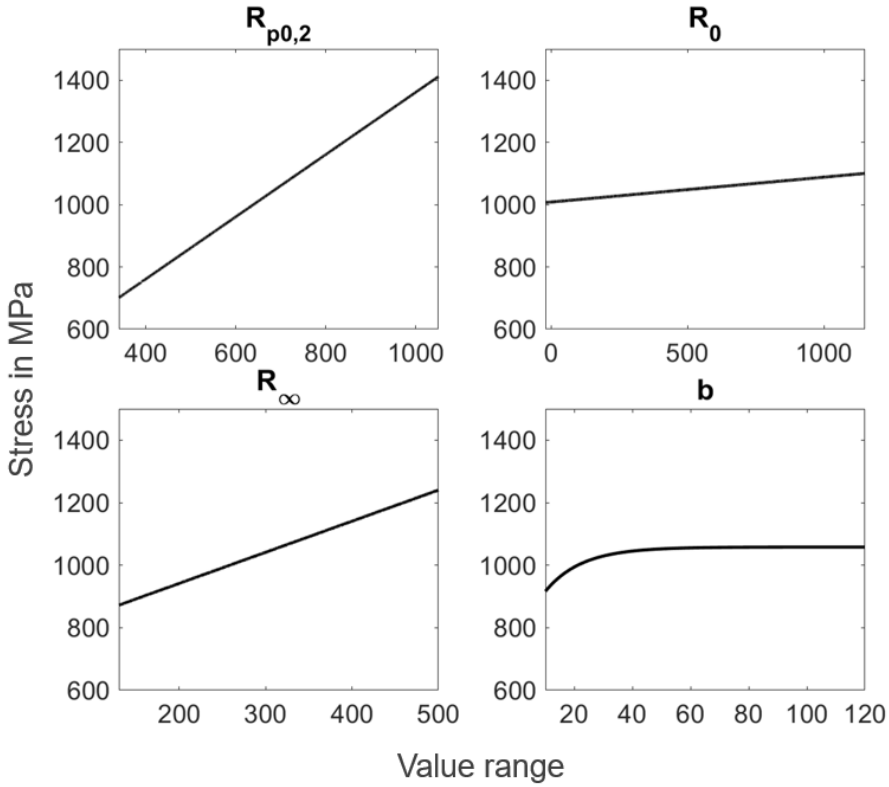

Figure 5.16 Sensitivity analysis of the material model parameters as output of the ANNs to evaluate their influences on the ultimate stress value by their variation in x-axis in the defined intervals as described in Table 5.1 by plotting the amount of stress at 8% of plastic strain

It can be concluded that the material parameters $R_{p0,2}$ and R_∞ have a significant effect on the final amount of stress, while the variation of the other parameters such as R_0 and b does not change the stress-strain curve considerably. On the other hand, as seen in Table 5.4, Table 5.5 and Table 5.6, the mean value of the deviation for the parameters $R_{p0,2}$ and R_∞ is small intrinsically and even the lowest compared to other material parameters. Therefore, it is expected to observe a small deviation between the stress-strain curves of reference and prediction in Figure 5.10, Figure 5.11 and Figure 5.14, although the deviation between the reference and predicted material parameters such as "b" is relatively high.

In summary, the current chapter explains the methodology of the ANN training with the datasets of the force-indentation depth curves and the profile of the indented samples, including the feature extraction and the architecture of the ANN. Then, the accuracy of the trained ANN is evaluated with different sizes of records and at the

end, the stress-strain diagrams as the output of the ANN is compared with the reference curves which show a strong agreement between them.

6. Summary

The goal of the current research is to introduce and develop ANNs capable of determining the mechanical properties of AHSSs in both base and weld metal from the information collected with the indentation test. Such records can be collected in various ways, e.g., the force-indentation depth diagrams or profiles of the indented surface. Other related datasets are the images taken from the indented surface of the specimens using a high-resolution 3D measurement system or light microscope, which are discussed in more details in the Appendix as further work. The training of the ANNs includes different phases, such as generation of datasets, training of the ANNs, and at the end, evaluation of the performance and accuracy of the ANNs with test materials.

In the current work, the mechanical properties of four AHSSs such as DP1000, DP800, DP600 and S690QL in different weld zones produced with different technologies such as RSW or LBW were determined to later verify the accuracy of the trained ANNs with them. The stress-strain diagrams of the AHSSs in base metal were obtained by performing the uniaxial quasi-static tensile test on the conventional tensile specimens. However, the challenge was to identify the material parameters of the weld metal or HAZ of the AHSSs, since it is not possible to prepare any standard tensile specimens from inhomogeneous structures. In the absence of a thermomechanical simulator in our research institute, the microstructure of WM made of RSW in DP600 and DP1000 is reproduced on a larger scale in one plate by changing the welding parameters. The subsequent metallographic investigations such as microstructural analysis, hardness measurement as well as heating and cooling cycle measurement show that the reproduced microstructures are similar for both industrial and optimal welding parameters.

In the next step, the notched tensile specimens from the welded plates were provided with the weld metal in the notch region to force the fracture to occur in the weld metal to determine the mechanical properties of WM made of RSW in DP600 and DP1000. In a parallel investigation, the effect of notch geometry was quantified as a term of the geometry factor and was applied to determine the conventional stress-strain curves of WM. In addition, the accuracy of the material model in calculating the parameters of the used AHSSs was analyzed in details for both BM and WM. It was found that RSW results in a reduction in ductility and an increase in yield and tensile strength for DP600 and DP1000. It was noticeable that the material parameters for welded DP600 and DP1000 were very similar, indicating that the same martensitic structure was present in the weld metal.

Afterwards, the instrumented indentation technique was used to perform the indentation on the specimens to obtain the force-indentation depth curves and also to examine the surface of the indented specimens with a 3D high-resolution measurement system as well as light microscope. In addition, a numerical simulation model of IIT was established and its accuracy was evaluated against the experimental data of the force-indentation depth curves and the profile of the indented surfaces. The goal of the simulation model is to generate a large volume of qualitative datasets to train the ANNs. In addition, the numerical simulation model was used to perform the inverse analysis to determine the mechanical properties of the weld zones of AHSSs such as WM of DP600 and S690QL from LBW and HAZ of DP1000 from RSW that could not be identified with the notched tensile specimens. The results demonstrated that the strength in the WM of LBW enhanced due to the martensitic microstructure. However, the yield strength of the resistance spot welded DP1000 in HAZ was reduced compared to the BM.

The final step to achieve the goal of this study is to train the ANNs with sufficient number of training records. Two ANNs were first trained with the same type of datasets (Force-Indentation depth curve) with different number of records, e.g., 250 and 500, to investigate the effect of increasing the number of records on the accuracy and performance of the trained ANNs. In addition, another ANN was trained with the input data of the profile of the indented surface and the output was similar to the other ANNs, i.e., the parameters of the material model. To assess the accuracy of the trained ANNs, a detailed analysis including the evaluation of MSE, the correlation coefficient, and the deviation between the calculated and the desired outputs (test

materials) was performed. It was observed that increasing the number of records improves the accuracy of the trained ANNs, though the effect is significant for some parameters such as the exponential saturation rate and minor for other parameters such as yield strength. On the other hand, the trained ANN with the profile of the indented surface with the small datasets (number of training data: 250) provides an ANN with better performance than the trained ANN with the large datasets of the force-indentation depth diagrams (number of training data: 500).

Moreover, the comparison between the entire stress-strain diagrams of predictions and references shows that there is a strong agreement between them and all three trained ANNs with different sizes and types of datasets can calculate the entire stress-strain diagrams accurately enough for any further applications.

7. Appendix: Further Work

In order to develop the methodology of material characterization with instrumented indentation technique (Figure 1.1, first methodology), an attempt was made to make the procedure independent of the instrumented indentation machine. Therefore, as explained in Section 5.2.2, the concept of training the ANN was developed by using the datasets of the indented surface profiles (Figure 1.1, second methodology). Although the surface of the specimens was indented with the instrumented indentation machine, the indentation can be performed with any equipment if the experimental conditions are calibrated the same for all specimens. Furthermore, there is no need to measure the force and the corresponding indentation depth in each step, which is the main output of the instrumented indentation machine. This means that the material characterization method is so far independent of an indentation machine, which can be not available in many companies or research institutes.

In a further step, the possibility of material characterization with the optical methods under certain conditions was evaluated based on the fact that if it is possible to determine the mechanical properties from the profile of the indented surface which is obtained from the images taken from the surface of the indented samples with a high-resolution 3D measurement system, as seen in Figure 4.7 (d), it may also be possible to work with an isometric 3D projection of the indented surface (Figure 1.1, third methodology), as seen in Figure 4.7 (a). The fact is that both, e.g. the profile of the indented surface (Figure 4.7 (a)) and the 3D projection of the indented surface (Figure 4.7 (d)) contain the very same information, namely the indentation depth on the surface of the specimens. The challenge is that the large datasets of the indented surface profile were generated using the numerical simulation as explained in Section 5.1.3, however, the numerical simulation cannot be applied to generate the datasets

of the indented surface images. Therefore, the training of the ANN in the current section is limited to a small volume of datasets.

The surface of indented specimens was visually analyzed by using the Alicona infinite focus as a contactless 3D surface measurement system as explained in section 4.2.2. The information related to the deformation depth of indented surface in each point was recorded in 2D and 3D and represented with a color. First, the images were processed to bring them into the same color scale as a measurement reference and the same size, brightness, and pixel. In total, nine images from the surface of the specimens mentioned in Tables 3.8, 3.10, and 4.2 were captured and processed. Each final image has a square shape with the same brightness and contained 170×170 pixels. The pixels had color values based on an RGB (red, green and blue) format which shows the indentation depth. The input data is needed to be dimensionally reduced to have less complexity before employing them as the input to train the ANN to eliminate the possibility of overfitting. By performing k-means clustering as an unsupervised machine learning algorithm, the RGB values in each pixel of the image were observed and partitioned into five optimal clusters extracted by analyzing the Silhouette index of each data point in each cluster of the k-means results. The algorithm returned the centroid of the clusters based on the RGB values and additionally assigned every pixel to its proper group. Furthermore, the Mann–Whitney–Wilcoxon test was conducted on each representative cluster to show that that each cluster is unique and independent of the others by resulting the p-value of less than 0.05. The transformation is depicted in Figure 7.1 in the unsupervised training part. Once again and as seen in isometric image of Figure 7.1, the colors from the 3D measurement system show the depth of penetration at each specific point.

The clustered colors were then sorted according to the Hue-saturation value, which was used to represent the depth from the 3D-measurement. By sorting the colors, it was guaranteed that the first centroid showed the region with the deepest indentation, located mostly in the middle of the image. The last centroid defined the highest region of the surface unaffected by the indentation or pile-up. Finally, the RGB values of each centroid were used as input for the training dataset. With this, the image that initially had 170×170×3 variables were reduced to a total of 5×3 parameters. Then, these parameters, shown in the red circle in Figure 7.1, were packed into a vector (15×1), and this vector was used as input data. The material parameters of each

image were used as the corresponding output. In the end, 15 input, 7 hidden, and 4 output neurons were needed to train the ANN with images from the 3D-measurement as shown in Figure 7.1.

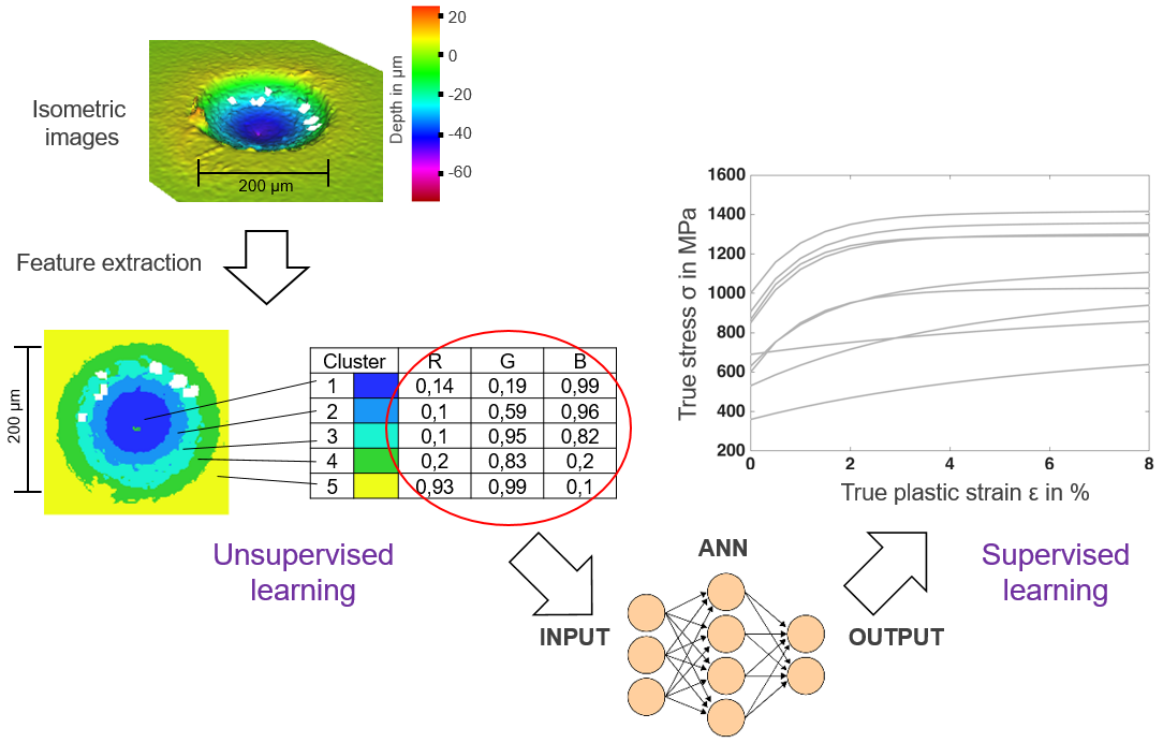

Figure 7.1 Feature extraction with the unsupervised learning algorithm from the images of the indented surface of a specimen captured with a high-resolution 3D measurement system (Alicona Infinite Focus), as explained in Section 4.2.2, and training the ANN as a supervised learning algorithm with them as input and the corresponding stress-strain curves as output

Since the number of images in the current dataset is limited, three different ANNs were trained and two materials were excluded in each training to check the accuracy of the trained ANNs by using them as test materials. As seen in Figure 7.2, the trained ANNs in the current section were able to determine the stress-strain curves well, but with lower accuracy compared to the first two datasets, e.g., force-indentation depth curves and the profile of the indented surfaces, the results of which are shown in Figures 5.10, 5.11, and 5.14.

Furthermore, Figure 7.2 shows that all the resulting stress-strain curves from the three trained ANNs can follow the reference diagrams, but with different deviation. The various differences between them may be due to the fact that the outputs of the training datasets are limited and concentrated on a certain part. By eliminating two output diagrams (stress-strain curves in Figure 7.1) as test material, the concentration

of data in a certain interval can be decreased and thus some curves can be predicted with lower accuracy. The deviation between the reference and the predicted yield strength varied from 3% to 26%. Due to the importance of the yield strength in the selected material model and the entire stress-strain curve, a small variation of this parameter can significantly change the resulting stress-strain curve, as discussed in Section 5.2.3. The high value of deviation was mainly caused by the limited number of training datasets and it is expected to be reduced by increasing the volume of training datasets.

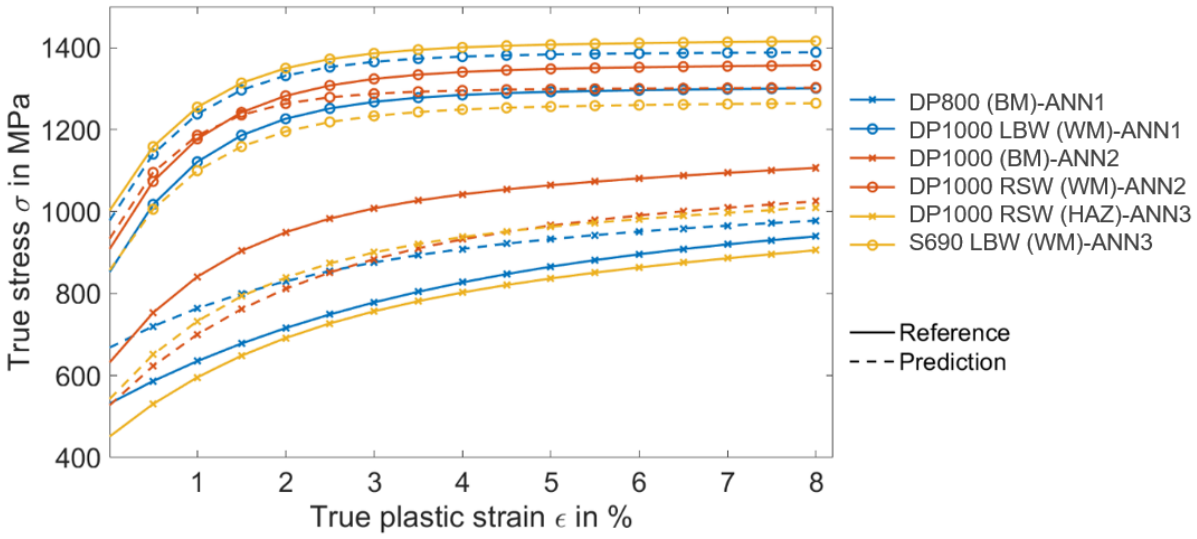

Figure 7.2 Comparison between the output of the ANN trained with features extracted from images captured from the indented surface of a specimen using a high-resolution 3D measurement system (Alicona Infinite Focus), as explained in Section 4.2.2, and the reference values whose mechanical properties were determined using different approaches in Chapter Three and Chapter Four, as shown in Tables 3.8, 3.10, and 4.2

Additionally, the concept of material characterization is further developed with the current methodology to make it more practical for the end user by using the images of the indented specimen surface taken with a simple light microscope as the input of the training datasets (Figure 1.1, fourth methodology). As explained in Section 4.2.2, the indented surface was examined under a simple light microscope with 40× magnification. All images were captured under the same conditions, such as lighting and camera position. In total, 11 grayscale images were successfully captured with the light microscope from the materials mentioned in Tables 3.8, 3.10, and 4.2 and the corresponding heat affected zones.

The images had a square shape with dimensions of 200×200 pixels. Image segmentation with k-means clustering was also performed on them. The optimal number of clusters, extracted by analyzing the Silhouette index of each data point in each cluster of k-means results, was 5. Since the images were in grayscale, the centroids of the clusters had three identical RGB values. This parameter represents the brightness, with 0 defined as black and 1 as white. The indented area is recognizable with its darker color as well as its surrounding. The size of the indented area is different between images and depends on the depth of the penetration. Therefore, instead of color values of each centroid, the number of pixels assigned to each cluster was considered as the input of training dataset. The centroids of five clusters were then sorted from light to dark as seen in Figure 7.3. In this step, the ANN was constructed with 5 input, 5 hidden, and 4 output neurons for the training with images from the light microscope. The Tansig and Purelin transfer functions were used as the activation function in the hidden and output layer. The learning rate of the network was 0.01. Due to the limited training dataset, backpropagation and he Levenberg–Marquardt optimization as well as Bayesian regularization were used to construct the ANN. This algorithm needs more computation time but is suitable for training with limited records. Moreover, the performance of the ANN was analyzed with the cross-validation method.

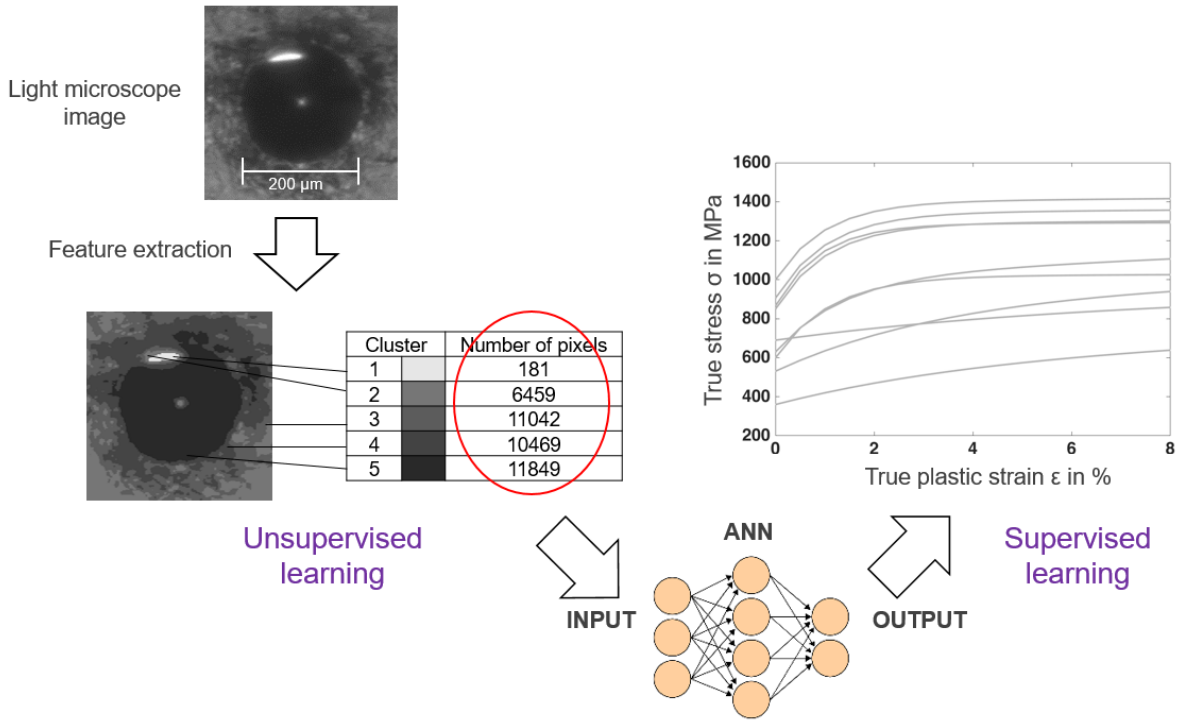

Figure 7.3 Feature extraction with the unsupervised learning algorithm from the images of the indented surface of a specimen captured with a light microscope, as explained in Section 4.2.2, and training the ANN as a supervised learning algorithm with them as input and the corresponding stress-strain curves as output

Figure 7.4 shows the comparison between the predicted stress-strain curves from the ANNs trained with the grayscale images taken with a simple light microscope and the reference values from Tables 3.8, 3.10, and 4.2. It seems that the ANN had difficulties in determining the strain hardening parameters such as R_o and b. However, it could estimate $R_{p0,2}$ and R_∞ with a deviation between the reference and prediction of less than 16% and 25%, respectively. Similar to the previous trained ANNs, three ANNs were trained and two test materials were excluded in each training to test the performance and accuracy of the trained ANNs with them later. Moreover, the similar explanation as for Figure 7.2 can be given here to justify the different deviations between the reference and predicted stress-strain curves.

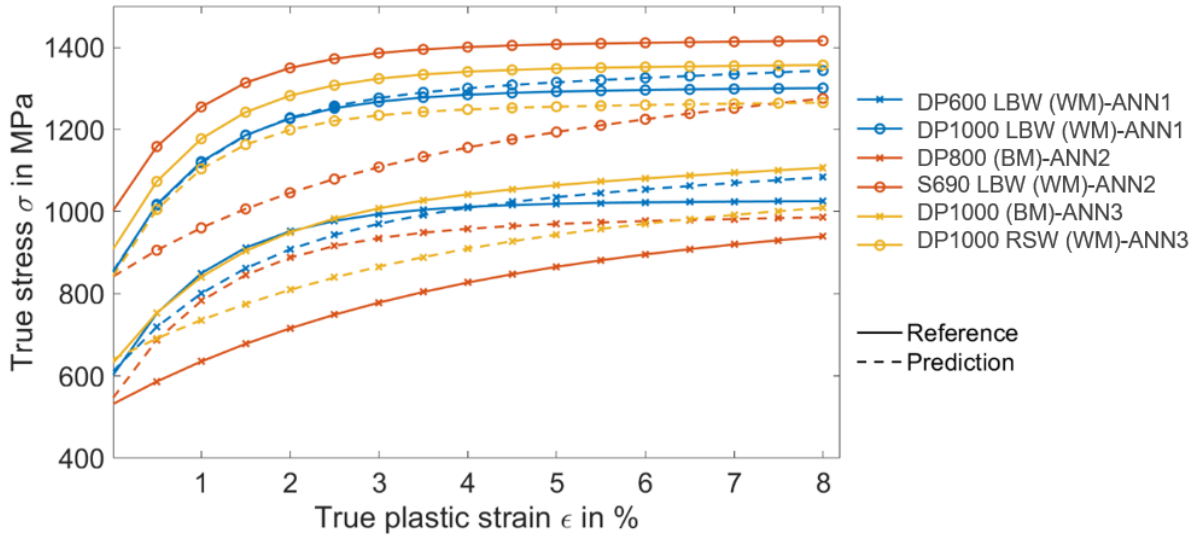

Figure 7.4 Comparison between the output of the ANN trained with the features extracted from images captured with a light microscope from the indented surface, as explained in section 4.2.2, and the reference values whose mechanical properties were determined using different approaches in Chapter Three and Chapter Four, as shown in Tables 3.8, 3.10, and 4.2

In the Appendix of the current dissertation, named "Further work", the methodology of material characterization by using the information of the indented surface of a sample was developed to introduce the concept of material parameter determination of a steel by using the images taken from the indented surface. The images were captured using a high-resolution 3D measurement system that accurately records all deformations on the surface of a specimen, and also using a light microscope. The goal of introducing these methods, shown as the third and fourth methods in Figure 1.1, is to facilitate on-site materials testing and inspection. However, more datasets are needed to perform material characterization by using images from the surface of the indented samples as a robust approach. Since it was not possible to provide such a large volume of datasets in the current work due to lack of resources and infrastructure, these methods are presented in the Appendix as Further Work to show that there is potential for future research in this area.

References

[1] E. Javaheri *et al.*, “Quantifying Mechanical Properties of Automotive Steels with Deep Learning Based Computer Vision Algorithms,” *Met. 10*, p. 163, 2020, doi: https://doi.org/10.3139/120.111349.

[2] E. Javaheri, A. Pittner, B. Graf, and M. Rethmeier, “Mechanical properties characterization of resistance spot welded DP1000 steel under uniaxial tensile tests,” *Mater. Test. 616*, pp. 527–532, 2019, doi: https://doi.org/10.3390/met10020163.

[3] E. Javaheri, J. Lubritz, B. Graf, and M. Rethmeier, “Mechanical Properties Characterization of Welded Automotive Steels,” *Met. 10 1*, 2020, doi: https://doi.org/10.3390/met10010001.

[4] E. Javaheri, A. Pittner, B. Graf, and M. Rethmeier, “Application of artificial neural network for the determination of local material properties of welded steel structures,” Düsseldorf, Germany, 2019.

[5] E. Javaheri, A. Pittner, B. Graf, and M. Rethmeier, “Instrumented indentation technique and its application for the determination of local material properties of welded steel structures,” presented at the 39. Assistentenseminar, DVS report, Aachen, Germany, 2019.

[6] E. Javaheri, B. Graf, and M. Rethmeier, “Qualifizierung der instrumentierten Eindringprüfung zur Kennwertermittlung für hochfeste Stähle mit Schweißungen,” Forschungsvereinigung Stahlanwendung e. V., Düsseldorf, Germany, AIF-Bericht; Forschungsprojekt P 1248 / IGF-Nr. 19550 N der FOSTA Bestell-Nr. P 1248, 2021.

[7] S. Dancette, V. Massardier-Jourdan, D. Fabregue, J. Merlin, T. Dupuy, and M. Bouzerkri, “HAZ Microstructures and Local Mechanical Properties of High Strength Steels Resistance Spot Welds,” *ISIJ International*, pp. 99–107, 2011.

[8] C. Asbjørn Sörensen, “A Material Framework for Product Design,” Faculty of Engineering and Department of Design Sciences, Lund University, 2018.

[9] *Summary for Policy Makers, In Climate Change 2014: Mitigation of Climate Change. Contribution of Working Group III to the Fifth Assessment Report of the Intergovernmental Panel on Climate Change*. Cambridge: Cambridge University Press, 2015.

[10] A. Ramazani, K. Mukherjee, A. Abdurakhmanov, M. Abbasi, and U. Prahl, “Characterization of Microstructure and Mechanical Properties of Resistance Spot Welded DP600 Steel,” *Metals 5, no. 3*, pp. 1704–1716, 2015.

[11] H. H. Stadelmaier and W. W. Austin, *Mechanical Properties of Engineering Materials: Macroscopic Behavior. Materials Science Research*. Springer, Boston, MA, 1963.

[12] J. R. Davis, *Tensile Testing, 2nd Edition*. ASM International, 2004.

[13] P. F. Pavel Konopik, “Application of micro-tensile test for material characterization of mild steel DC01,” *Ubiquity Proc.*, vol. 1, p. 33, Sep. 2018, doi: 10.5334/uproc.33.

[14] W. Liu and et al, “Gleeble simulation of the HAZ in Inconel 617 welding,” *Journal of Materials Processing Technology (225)*, pp. 221–228, 2015.

[15] T. TABOR, *Hardness of Metals*. Oxford: Clarendon Press, 1948.

[16] J.-H. Ahn and D. Kwon, “Derivation of plastic stress-strain relationship from ball indentations: Examination of strain definition and pileup effect,” *J. Mater. Res. 16*, p. 3170, 2001.

[17] I. 29381:2008(E), “TECHNICAL REPORT; Metallic materials-Measurement of mechanical properties by an instrumented indentation test-Indentation tensile properties,” Switzerland, 2008.

[18] C. Ullner, “Determination of local stress–strain properties of resistance spot-welded joints of advanced high-strength steels using the instrumented indentation test,” *J Mater Sci 47*, pp. 1504–1513, 2012.

[19] Y.-C. Kim, W.-S. Song, J.-H. Kim, K.-H. Kim, and D. Kwon, “Quantitative Characterization of Mechanical Properties using Instrumented Indentation,” *Procedia Engineering (10)*, pp. 3162–3172, 2011.

[20] N. Huber, A. Konstantinidis, and C. Tsakmakis, “Determination of Poisson’s Ratio by Spherical Indentation Using Neural Networks—Part I: Theory,” *ASME J Appl Mech*, vol. 68(2), pp. 218–223, 2001.

[21] D. Schaeffler, “Introduction to advanced high-strength steels-Part I,” *Stamp. J.*, vol. 16, pp. 22–28, 2004.

[22] J. Schumpeter, “Creative destruction,” *Capital. Social. Democr.*, vol. 825, pp. 82–85, 1942.

[23] O. Manual, “The measurement of scientific and technological activities. Proposed guidelines for collecting and interpreting technological innovation data,” *Eur. Comm. Eurostat*, 2005.

[24] H. Lööf and A. Heshmati, “On the relationship between innovation and performance: A sensitivity analysis,” *Econ. Innov. New Technol.*, vol. 15, no. 4–5, pp. 317–344, 2006.

[25] B. DEL CURTO, “The importance of materials and technologies in design_,” 2009, pp. 1–8.

[26] H. Bhadeshia and R. Honeycombe, *Steels: microstructure and properties*. Butterworth-Heinemann, 2017.

[27] A. Kalhor, M. Soleimani, H. Mirzadeh, and V. Uthaisangsuk, “A review of recent progress in mechanical and corrosion properties of dual phase steels,” *Arch. Civ. Mech. Eng.*, vol. 20, no. 3, pp. 1–14, 2020.

[28] M. Handbook, “Vol. 1, Properties and Selection,” *Irons Steels High-Perform. Alloys ASM Int. Mater. Park OH*, vol. 44073, 1990.

[29] D. Das and P. P. Chattopadhyay, “Influence of martensite morphology on the work-hardening behavior of high strength ferrite–martensite dual-phase steel,” *J. Mater. Sci.*, vol. 44, no. 11, pp. 2957–2965, 2009.

[30] M. Y. Sun *et al.*, “The critical impact of intercritical deformation on variant pairing of bainite/martensite in dual-phase steels,” *Mater. Sci. Eng. A*, vol. 771, p. 138668, 2020.

[31] R. G. Davies, “Influence of martensite composition and content on the properties of dual phase steels,” *Metall. Trans. A*, vol. 9, no. 5, pp. 671–679, 1978.

[32] L. Gardner and X. Yun, “Description of stress-strain curves for cold-formed steels,” *Constr. Build. Mater.*, vol. 189, pp. 527–538, 2018.

[33] G. R. Speich, “Dual-phase steels,” *ASM Int. Met. Handb. Tenth Ed.*, vol. 1, pp. 424–429, 1990.

[34] D. Arsic, V. Lazic, R. R. Nikolic, S. Aleksandrovic, B. Hadzima, and M. Djordjevic, “Optimal welding technology of high strength steel S690QL,” *Mater. Eng.-Materiálové Inž. MEMI*, vol. 22, no. 1, pp. 33–47, 2015.

[35] N. Baddoo and D. Brown, “High strength steel,” *New Steel Constr.*, vol. 23, no. 8, pp. 24–26, 2015.

[36] R. W. Messler, *Joining of materials and structures: from pragmatic process to enabling technology*. Butterworth-Heinemann, 2004.

[37] H. J. Fahrenwaldt and V. Schuler, *Praxiswissen schweisstechnik: werkstoffe, prozesse, fertigung*. Springer-Verlag, 2011.

[38] K. Weman, *Welding processes handbook*. Elsevier, 2011.

[39] M. Rethmeier, S. Brauser, and G. Weber, “Potential of optical strain field measurement for the characterisation of the properties of resistance-spot-welded joints,” 2011.

[40] N. T. Williams, “Resistance spot welding,” *ASM Handb.*, vol. 6, pp. 226–229, 1993.

[41] H. J. Fahrenwaldt, *Praxiswissen Schweitechnik: Werkstoffe*. Springer Fachmedien Wiesbaden, 2014.

[42] R. P. Martukanitz, “A critical review of laser beam welding,” 2005, vol. 5706, pp. 11–24.

[43] S. Katayama, *Handbook of laser welding technologies*. Elsevier, 2013.

[44] G. E. Dieter, “Mechanical behavior under tensile and compressive loads,” *Asm Handb.*, vol. 8, pp. 99–108, 2000.

[45] A. K. Saxena, S. Brinckmann, B. Völker, G. Dehm, and C. Kirchlechner, “Experimental conditions affecting the measured fracture toughness at the microscale: Notch geometry and crack extension measurement,” *Mater. Des.*, vol. 191, p. 108582, 2020.

[46] J. R. Rice, “On the Structure of Stress-Strain Relations for Time-Dependent Plastic Deformation in Metals,” *ASME J Appl Mech*, vol. 37, no. 3, pp. 728–737, 1970.

[47] K. Yamaguchi, H. Adachi, and N. Takakura, “Effects of plastic strain and strain path on youngs modulus of sheet metals,” *Metals and Materials 4*, pp. 420–425, 1995.

[48] G. Greaves, A. Greer, R. Lakes, and et al, “Poisson’s ratio and modern materials,” *Nature Mater 10*, pp. 823–837, 2011.

[49] E. N. Borodin, A. E. Mayer, Y. V. Petrov, and et al, “Maximum yield strength under quasi-static and high-rate plastic deformation of metals,” *Phys. Solid State 56*, pp. 2470–2479, 2014.

[50] DIN 50125:2009-07, “Prüfung metallischer Werkstoffe-Zugproben: Testing of metallic materials-Tensile test pieces,” Deutsches Institut für Normung e. V., Berlin, Germany, Dec. 2016.

[51] DIN EN ISO 6892-1, “Metallic materials –Tensile testing –Part 1: Method of test at room temperature (ISO 6892-1:2016);German version EN ISO 6892-1:2016,” DIN Deutsches Institut für Normung, Berlin, Germany, Feb. 2017.

[52] F. Yoshida, M. Urabe, and V. V. Toropov, “Identification of material parameters in constitutive model for sheet metals from cyclic bending tests,” *International Journal of Mechanical Sciences*, pp. 237–249, 1998.

[53] A. A. Mohammed, S. M. Haris, and W. Al Azzawi, “Estimation of the ultimate tensile strength and yield strength for the pure metals and alloys by using the acoustic wave propertiesEstimation of the ultimate tensile strength and yield strength for the pure metals and alloys by using the acoustic wave pro,” *Sci Rep 10*, 2020.

[54] J. Valíček *et al.*, “Quantifying the Mechanical Properties of Materials and the Process of Elastic-Plastic Deformation under External Stress on Material,” *Materials*, pp. 7401–7422, 2015.

[55] E. M.C.Jones *et al.*, “Parameter covariance and non-uniqueness in material model calibration using the Virtual Fields Method,” *Computational Materials Science*, vol. 152, pp. 268–290, 2018.

[56] J. Rösler, H. Harders, and M. Bäker, *Mechanisches Verhalten der Werkstoffe*. Springer-Verlag, 2012.

[57] E. Voce, “A practical strain-hardening function,” *Metallurgica*, pp. 219–226, 1955.

[58] A. L. Gurson, “Continuum Theory of Ductile Rupture by Void Nucleation and Growth: Part I-Yield Criterion and Flow Rules for Porous Ductile Media,” *J. Eng. Mater. Technol.*, vol. 1, pp. 2–15, 1977.

[59] A. Needleman and V. Tvergaard, “An Analysis of Ductile Rupture in Notched Bars,” *J. Mech. Phys. Solids*, vol. 32, no. 6, pp. 461–490, 1984.

[60] A. Birkert, S. Haage, and M. Straub, *Umformtechnische Herstellung komplexer Karosserieteile: Auslegung von Ziehanlagen*. Springer-Verlag, 2013.

[61] E. Javaheri, K. Hemmesi, P. Tempel, R. Fenzl, and M. Farajian, “Fatigue assessment of the welded joints containing process relevant imperfections,” *Weld. World 63*, pp. 249–261, 2019, doi: https://doi.org/10.1007/s40194-018-00676-y.

[62] S. Tu, X. Ren, B. Nyhus, O. M. Akselsen, J. He, and Z. Zhang, “A special notched tensile specimen to determine the flow stress-strain curve of hardening materials without applying the Bridgman correction,” *Eng. Fract. Mech.*, vol. 179, pp. 225–239, Jun. 2017, doi: 10.1016/j.engfracmech.2017.04.039.

[63] Z. L. Zhang, M. Hauge, C. Thaulow, and J. Ødegård, “A notched cross weld tensile testing method for determining true stress–strain curves for weldments,” *Eng. Fract. Mech.*, vol. 69, no. 3, pp. 353–366, 2002.

[64] H. Klingelhöffer, “European TENSTAND project; ISO 6892-1; Strain controlled tensile testing; Stress rate,” Committee meeting of ISO TC 164 SC1 WG4, Teddington, UK, 2015.

[65] R. Klinman and et al, “Ultrasonic prediction of grain size, strength, and toughness in plain carbon steel, In Ultrasonic Materials Characterization,” presented at the Proceedings of the First International Symposium on Ultrasonic Materials Characterization Held at the National Bureau of Standards, 1980.

[66] C. H. Hsu and et al, “Relationship between ultrasonic characteristics and mechanical properties of tempered martensitic stainless steel,” *J. Mater. Eng. Perform.*, pp. 593–599, 2004.

[67] W. Oliver and G. Pharr, “n improved technique for determining hardness and elastic modulus using load and displacement sensing indentation experiments,” *Journal of Materials Research 7(06)*, pp. 1564–1583, 1992.

[68] G. Revankar, “Introduction to Hardness Testing,” *Mater. Park OH ASM Int. 2000*, pp. 197–202, 2000.

[69] E. I. 14577-1:2002, “Metallic materials-Instrumented indentation test for hardness and materials parameters-Part 1: Test method (ISO 14577-1:2002),” DIN Deutsches Institut für Normung e.V., Berlin, Germany, 2003.

[70] E. I. 14577-2:2002, “Metallic materials-Instrumented indentation test for hardness and materials parameters-Part 2: Verification and calibration of testing machines (ISO 14577-2:2002),” DIN Deutsches Institut für Normung e.V., Berlin, Germany, 2003.

[71] D. Klöter and et al, “Identification of viscoplastic material parameters from sphrical indentation data; Part 2. Experimental validation of the method,” *J. Mater. Res. (21)*, 2005.

[72] E. I. 14577-3:2002, “Metallic materials-Instrumented indentation test for hardness and materials parameters-Part 3: Calibration of reference blocks (ISO 14577-3:2002),” DIN Deutsches Institut für Normung e.V., Berlin, Germany, 2003.

[73] E. I. 14577-4:2007, “Metallic materials-Instrumented indentation test for hardness and materials parameters-Part 4: Test method for metallic and non-metallic coatings (ISO 14577-4:2007),” DIN Deutsches Institut für Normung e.V., Berlin, Germany, 2007.

[74] Zwick-Materials Testing and PI 739 2.0809, “Product Information: Universal hardness testing machine ZHU/zwicki-Line.”

[75] C.-S. Han and S. Nikolov, “Indentation size effects in polymers and related rotation gradients,” *J. Mater. Res.*, vol. 22, pp. 1662–1672, Jun. 2007, doi: 10.1557/JMR.2007.0197.

[76] T. Trzepiecinski and H. G. Lemu, “A Three-Dimensional Elastic-Plastic Contact Analysis of Vickers Indenter on a Deep Drawing Quality Steel Sheet,” *Mater. Basel Switz.*, vol. 12, no. 13, p. 2153, Jul. 2019, doi: 10.3390/ma12132153.

[77] V. Karthik *et al.*, “Finite element analysis of spherical indentation to study pile-up/sink-in phenomena in steels and experimental validation,” *Int. J. Mech. Sci.*, vol. 54, no. 1, pp. 74–83, 2012.

[78] S. H. Kim, B. W. Lee, Y. Choi, and D. Kwon, “Quantitative determination of contact depth during spherical indentation of metallic materials,” *Mater. Sci. Eng.*, p. 59, 2006.

[79] S.-K. Kang, J.-Y. Kim, P.-P. Chan, H.-U. Kim, and D. Kwon, “Conventional Vickers and true instrumented indentation hardness determined by instrumented indentation tests,” *J. Mater. Res.*, vol. 25, no. 2, pp. 337–343, Feb. 2010, doi: 10.1557/JMR.2010.0045.

[80] W. Hang, L. Zhou, J. Shimizu, and J. Yuan, “A robust procedure of data analysis for micro/nano indentation,” *Precision Engineering*, pp. 408–414, 2013.

[81] E.-C. Jeon, J.-S. Park, and D. Kwon, “Statistical analysis of experimental parameters in continuous indentation tests using Taguchi method,” *ASME J. Eng. Mater. Technol. 125*, p. 406, 2003.

[82] T. Nakamura, T. Wang, and S. Sampath, “Determination of properties of graded materials by inverse analysis and instrumented indentation,” *Acta Mater.*, vol. 48, no. 17, pp. 4293–4306, Nov. 2000, doi: 10.1016/S1359-6454(00)00217-2.

[83] T. Nakamura and Y. Gu, “Identification of elastic–plastic anisotropic parameters using instrumented indentation and inverse analysis,” *Mech. Mater.*, vol. 39, no. 4, pp. 340–356, Apr. 2007, doi: 10.1016/j.mechmat.2006.06.004.

[84] R. E. Kalman, “A New Approach to Linear Filtering and Prediction Problems,” *J. Basic Eng.*, vol. 82, no. 1, pp. 35–45, Mar. 1960, doi: 10.1115/1.3662552.

[85] Angus P. Andrews and Mohinder S. Grewal, *Kalman Filtering: Theory and Practice Using MATLAB*, 4. Wiley-IEEE, 2021.

[86] A. Corigliano, "Elasto-Plastic Interface Law for Non-Homogeneous Materials: Formulation, Sensitivity Analysis, Parameter Identification," in *IUTAM Symposium on Analytical and Computational Fracture Mechanics of Non-Homogeneous Materials*, Dordrecht, 2002, pp. 233–242.

[87] T. Kamhda and S. Koyama, "Stress Distribution Determination Scheme for Elastic Plastic Material Based on Equivalent Inclusion Method," *Inverse Problems in Engineering Mechanics III, Elsevier Science Ltd,* pp. 193–200, 2002.

[88] J.-M. Collin, G. Mauvoisin, and P. Pilvin, "Materials characterization by instrumented indentation using two different approaches," *Mater. Des.*, vol. 31, no. 1, pp. 636–640, Jan. 2010, doi: 10.1016/j.matdes.2009.05.043.

[89] ISO, "Metallic materials—Measurement of mechanical properties by an instrumented indentation test—Indentation tensile properties," *NPR-ISOTR 29381*, pp. 1–29, 2008.

[90] K. D. Bouzakis, N. Michailidis, and G. Erkens, "Thin hard coating stress-strain curve determination through a FEM supported evaluation of nano-indentation test results," *Surf. Coat. Tech. (142-144)*, p. 102, 2001.

[91] M. Dao, N. Chollacoop, K. J. Van Vlient, T. A. Venkatesh, and S. Suresh, "Computational modeling of the forward and reverse problems in instrumented sharp indentation," *Acta Mater (49)*, pp. 3899–3905, 2001.

[92] J. L. Bucaille, S. Stauss, E. Felder, and J. Michler, "Determination of plastic properties of metals by instrumented indentation using different sharp indenters," *Acta Mater (51)*, pp. 1663–1668, 2003.

[93] K. D. Bouzakis and N. Michailidis, "Indenter surface area and hardness determination by means of a FEM-supported simulation of nano-indentation," *Thin Solid Films (494)*, pp. 155–162, 2006.

[94] N. Huber and C. Tsakmakis, "Determination of constitutive properties from spherical indentation data using neural networks. Part I: The case of pure kinematic hardening in plasticity laws," *J. Mech. Phys. Solids*, vol. 47, pp. 1569–1588, 1999.

[95] N. Huber, "Anwendung Neuronaler Netze bei nichtlinearen Problemen der Mechanik, Habilitationsschrift, FZKA 6504," Universität Karlsruhe (TH), 2000.

[96] W. S. McCulloch and W. H. Pitts, "A Logical Calculus of the Ideas Immanent in Nervous Activity, Reprinted in McCulloch 1964, pp16-39," *Bulletin of Mathematical Biophysics 7*, pp. 115–133, 1943.

[97] M. Garnelo and M. Shanahan, "Reconciling deep learning with symbolic artificial intelligence: representing objects and relations," *Current Opinion in Behavioral Sciences (29)*, pp. 17–23, 2019.

[98] P. Jackson, *Introduction to expert systems*. Addison-Wesley Pub (Sd); 2nd Edition (1. Mai 1990), 1990.

[99] G. Yagawa and H. Okuda, "Neural networks in computational mechanics," *Arch. Comput. Methods Eng.*, vol. 3, no. 4, pp. 435–512, 1996.

[100] A. A. Huqqani, E. Schikuta, S. Ye, and P. Chen, "Multicore and GPU Parallelization of Neural Networks for Face Recognition," *Procedia Computer Science (18)*, pp. 349–358, 2013.

[101] I. S. A Krizhevsky, “Imagenet classification with deep convolutional neural networks,” *Communications of the ACM*, pp. 84–90, 2017.

[102] J. H. D. Rao, “On characterisation of local stress–strain properties in friction stir welded aluminium AA 5083 sheets using micro-tensile specimen testing and instrumented indentation technique,” *Mater. Sci. Eng. 52718-19*, pp. 5018–5025, 2010.

[103] B. L. Sang Ye, “Deep neural network method for predicting the mechanical properties of composites,” *Appl. Phys. Lett. (115)*, 2019.

[104] X. L. and K. Z. Z. Xu, “Mechanical Properties Prediction for Hot Rolled Alloy Steel Using Convolutional Neural Network,” *IEEE Access, vol. 7*, pp. 47068–47078, 2019.

[105] P. Chun, T. Yamane, S. Izumi, and T. Kameda, “Evaluation of Tensile Performance of Steel Members by Analysis of Corroded Steel Surface Using Deep Learning,” *Metals 9 (12)*, p. 1259, 2019.

[106] W. Wang, P. Shi, L. Deng, H. Chu, and X. Kong, “Residual Strength Evaluation of Corroded Textile-Reinforced Concrete by the Deep Learning-Based Method,” *Materials 13 (14)*, p. 3226, 2020.

[107] I. Basheer and M. Hajmeer, “Artificial neural networks: Fundamentals, computing, design, and application,” *J. Microbiol. Methods (43)*, pp. 3–31, 2000.

[108] N. Huber and C. Tsakmakis, “Determination of Poisson’s Ratio by Spherical Indentation Using Neural Networks—Part II: Identification Method,” *ASME J Appl Mech 682*, pp. 224–229, 2001.

[109] E. Tyulyukovskiy and N. Huber, “Identification of viscoplastic material parameters from spherical indentation data: Part I. Neural networks,” *J. Mater. Res. 213*, pp. 664–676, 2006.

[110] D. Klötzer, C. Ullner, E. Tyulyukovskiy, and N. Huber, “Identification of viscoplastic material parameters from spherical indentation data: Part II. Experimental validation of the method,” *J. Mater. Res. 213*, pp. 677–684, 2006.

[111] N. Huber and C. Tsakmakis, “Determination of constitutive properties from spherical indentation data using neural networks. Part ii:plasticity with nonlinear isotropic and kinematichardening,” *Journal of the Mechanics and Physics of Solids*, pp. 1589–1607, 1999.

[112] Z. L. Xiang Li, “Predicting the effective mechanical property of heterogeneous materials by image based modeling and deep learning,” *Computer Methods in Applied Mechanics and Engineering (347)*, pp. 735–753, 2019.

[113] L. Harrsion, M. Ravan, D. Tandel, K. Zhang, T. Patel, and R. K. Amin, “Material Identification Using a Microwave Sensor Array and Machine Learning,” *Electronics 9(2); Applications of Electromagnetic Waves*, 2020.

[114] E. DIN, “5821: 2010-04,„,” *Widerstandsschweißen-Punktschweiß-Elektrodenkappen ISO 5821 2009*.

[115] S. 1220-2:2011-08, “Prüf- und Dokumentationsrichtlinie für die Fügeeignung von Feinblechen aus Stahl – Teil 2: Widerstandspunktschweißen, Beuth Verlag, Berlin (2011).”

[116] J. D. Rigney, “Introduction to the Mechanical Behavior of Metals,” 2000.

[117] N. Zhong, X. Liao, M. Wang, Y. Wu, and Y. Rong, “Improvement of microstructures and mechanical properties of resistance spot welded DP600 steel by double pulse technology,” *Mater. Trans.*, vol. 52, no. 12, pp. 2143–2150, 2011.

[118] T. STAHL, “ThyssenKrupp Stahl Werkstoffblatt 1800: DP-W 550 und DP-W 600,” 2002.

[119] DIN EN ISO 6507, “DIN EN ISO 6507-1:2018-07; Metallische Werkstoe-Härteprüfung nach Vickers: Teil 1: Prüfverfahren (ISO6507-1:2018),” 2018.

[120] O. Sherepenko and S. Jüttner, “Transient softening at the fusion boundary in resistance spot welded ultra-high strengths steel 22MnB5 and its impact on fracture processes,” *Weld World 63*, pp. 151–159, 2019.

[121] THYSSENKRUPP STAHL, “ThyssenKrupp Stahl Werkstoffblatt 1800: DP-W 550 und DP-W 600,” Jun. 2002.

[122] W. Kapłonek, K. Nadolny, and G. M. Królczyk, “The use of focus-variation microscopy for the assessment of active surfaces of a new generation of coated abrasive tools,” *Meas. Sci. Rev.*, vol. 16, no. 2, pp. 42–53, 2016.

[123] H. Lee, J. Lee, and M. Pharr, “numerical approach to spherical indentation techniques for material property evaluation,” *Journal of the Mechanics and Physics of Solids*, pp. 2037–2069, 2005.

[124] E. A. Ariza, A. S. Nishikawa, H. Goldenstein, and A. P. Tschiptschin, “Characterization and methodology for calculating the mechanical properties of a TRIP-steel submitted to hot stamping and quenching and partitioning (Q&P),” *Materials Science & Engineering A*, pp. 54–69, 2016.

[125] J. Chen and S. J. Bull, “Relation between the ratio of elastic work to the total work of indentation and the ratio of hardness to Young’s modulus for a perfect conical tip,” *J. Mater. Res.*, vol. 24, pp. 590–598, 2009.

[126] S. SYNGELLAKIS, H. HABBAB, and B. G. MELLOR, “Finite element simulation of spherical indentation experiments,” *Int J Comp Meth Exp Meas*, vol. 6, no. 4, pp. 749–763, 2018.

[127] C. Jiang, D. Michael, and J. Zekonyte, “Finding Minimal Optimal Indent Separation for Polystyrene via Instrumental Nanoindentation and FEA Method,” *Appl. Sci.*, vol. 10, no. 12, p. 4262, 2020.

[128] W. Oliver and G. Pharr, “An improved technique for determining hardness and elastic modulus using load and displacement sensing indentation experiments,” *J. Mater. Res.*, vol. 7, no. 6, pp. 1564–1583, 1992.

[129] M. Doerner and W. Nix, “A method for interpreting the data from depth-sensing indentation instruments,” *J. Mater. Res.*, vol. 1, no. 4, 1986.

[130] J. H. Kim, A. Gouldstone, and C. S. Korach, “Analysis of Spherical Indentation of an Elastic Bilayer Using a Modified Perturbation Approach,” in *MEMS and Nanotechnology, Volume 4*, New York, NY, 2011, pp. 53–57.

[131] YT. Cheng and CM. Cheng, “Relationships between initial unloading slope, contact depth, and mechanical properties for conical indentation in linear viscoelastic solids,” *J. Mater. Res.*, vol. 20, pp. 1046–1053, 2005, doi: https://doi.org/10.1557/JMR.2005.0141.

[132] B. J. Briscoe, L. Fiori, and E. Pelillo, “Nano-indentation of polymeric surfaces,” *J. Phys. Appl. Phys.*, vol. 31, p. 2395, 1998.

[133] W. Hang, L. Zhou, J. Shimizu, J. Yuan, and T. Yamamoto, “Study on the mechanical properties of lithium tantalate and the influence on its machinability,” *Int. J. Autom. Technol.*, vol. 7, pp. 644–653, 2013.

[134] D. Zíta, P. Hanus, E. Schmidová, and J. Zajíc, “Determining of the machine compliance using instrumented indentation test and finite element method,” *IOP Conf. Ser. Mater. Sci. Eng.*, vol. 461, p. 012095, Dec. 2018, doi: 10.1088/1757-899x/461/1/012095.

[135] K. Grochalski, M. Wieczorowski, J. H’roura, and G. Le Goïc, “The Optical Aspect of Errors in Measurements of Surface Asperities Using the Optical Profilometry Method,” *Front. Mech. Eng.*, vol. 6, p. 12, Mar. 2020, doi: 10.3389/fmech.2020.00012.

[136] Y. Bergström, Y. Granbom, and D. Sterkenburg, “A Dislocation-Based Theory for the Deformation Hardening Behavior of DP Steels: Impact of Martensite Content and Ferrite Grain Size,” *J. Metall.*, vol. 2010, p. 647198, Dec. 2010, doi: 10.1155/2010/647198.

[137] J. Hu, Y. Zhang, W. Sun, and T. Zhang, “Nanoindentation-Induced Pile-Up in the Residual Impression of Crystalline Cu with Different Grain Size,” *Crystals*, vol. 8, no. 1, 2018, doi: 10.3390/cryst8010009.

[138] R. W. Armstrong, “60 Years of Hall-Petch: Past to Present Nano-Scale Connections,” *Mater. Trans.*, vol. 55, no. 1, pp. 2–12, 2014, doi: 10.2320/matertrans.MA201302.

[139] K. Hornik, “Approximation capabilities of multilayer feedforward networks,” *Neural Netw.*, vol. 4, no. 2, pp. 251–257, Jan. 1991, doi: 10.1016/0893-6080(91)90009-T.

[140] G. Cybenko, “Approximations by superpositions of sigmoidal functions,” *Math. Control Signals Syst.*, vol. 2, no. 4, pp. 303–304, 1989.

[141] G. Hinton, S. Osindero, and Y. W. Teh, “A Fast Learning Algorithm for Deep Belief Nets,” *Neural Comput.*, vol. 18, no. 7, pp. 1527–1554, 2006.

[142] S. Karsoliya, “Approximating Number of Hidden layer neurons in Multiple Hidden Layer BPNN Architecture,” *Int. J. Eng. Trends Technol. IJETT*, vol. V3, no. 6, pp. 714–717, Dec. 2012.

[143] K. Levenberg, “A method for the solution of certain non-linear problems in least squares,” *Quart. Appl. Math*, American Mathematical Society, pp. 164–168, 1944.

[144] M. T. Hagan and M. Menha, “Training feed-forward networks with the Marquardt algorithm,” *IEEE Trans. Neural Netw.*, vol. 5, no. 6, 1999, pp. 989–993, 1994.

[145] M. T. Hagan, H. B. Demuth, and M. H. Beale, *Neural Network Design*, PWS Publishing. Boston,MA, USA, 1996.